1-2012

Optical and Mechanical Characterization of InAs/GaAs Quantum Dot Solar Cells

Christopher G. Bailey

OPTICAL AND MECHANICAL CHARACTERIZATION OF InAs/GaAs QUANTUM DOT SOLAR CELLS

by

CHRISTOPHER G. BAILEY

A DISSERTATION

Submitted in partial fulfillment of the requirements
For the degree of Doctor of Philosophy
in
Microsystems Engineering
at the
Rochester Institute of Technology

January, 2012

Author: _____
Microsystems Engineering Program

Certified by: _____
Ryne P. Raffaelle, Ph.D.
Co-advisor, Vice President of Research

Certified by: _____
Seth M. Hubbard, Ph.D.
Co-advisor, Assistant Professor, Department of Physics

Approved by: _____
Bruce W. Smith, Ph.D.
Director of Microsystems Engineering Program

Certified by: _____
Harvey J. Palmer, Ph.D.
Dean, Kate Gleason College of Engineering

NOTICE OF COPYRIGHT

REPRODUCTION PERMISSION STATEMENT

Permission Granted

TITLE:

"Optical And Mechanical Characterization of InAs/GaAs Quantum Dot Solar Cells"

I, *Christopher G. Bailey*, hereby grant permission to the Wallace Library of the Rochester Institute of Technology to reproduce my dissertation in whole or in part. Any reproduction will not be for commercial use or profit.

Signature of Author: _____ Date:_____

OPTICAL AND MECHANICAL CHARACTERIZATION
OF InAs/GaAs QUANTUM DOT SOLAR CELLS

By

Christopher George Bailey

Submitted by Christopher George Bailey in partial fulfillment of the requirements for the degree of Doctor of Philosophy in Microsystems Engineering and accepted on behalf of the Rochester Institute of Technology by the dissertation committee.

We, the undersigned members of the Faculty of the Rochester Institute of Technology, certify that we have advised and/or supervised the candidate on the work described in this dissertation. We further certify that we have reviewed the dissertation manuscript and approve it in partial fulfillment of the requirements of the degree of Doctor of Philosophy in Microsystems Engineering.

Dr. Seth M. Hubbard _____
(Dissertation Advisor)

Dr. Ryne P. Raffaelle _____
(Committee Chair & Dissertation Advisor)

Dr. Sean L. Rommel _____

Dr. Alan D. Raisanen _____

Dr. Donald F. Figer _____

Dr. Bruce W. Smith _____
(Director, Microsystems Engineering)

Dr. Harvey J. Palmer _____

MICROSYSTEMS ENGINEERING PROGRAM
ROCHESTER INSTITUTE OF TECHNOLOGY

To my grandmother Katherine Kramer for her passion, wisdom and strength which she showed me during the precious years we spent together. Her encouragement lives on in everything I do.

Abstract

Kate Gleason College of Engineering
Rochester Institute of Technology

Degree Doctor of Philosophy **Program** Microsystems Engineering

Name of Candidate Christopher G. Bailey

Title Optical and mechanical characterization of inas/gaas quantum dot solar cells

State of the art triple junction solar cells have achieved in excess of 43% efficiency. In order to extend this beyond a multijunction-only design, novel approaches to photon conversion must be sought and realized. Two novel mechanisms, bandgap engineering and absorption from an intermediate state within a semiconductor bandgap show promise in this regard. A single promising approach to both of these novel mechanisms is to exploit the unique properties of nanostructured materials to extend the absorption spectrum for the ultimate improvement of solar energy conversion efficiency. In this work, it is proposed to utilize InAs quantum dot (QD) nanostructures embedded in a GaAs *p-i-n* solar cell device to investigate the effects of these unique properties. Theoretical and experimental approaches will be used in tandem to explore these types of devices with special attention given to mechanical issues and optical processes inherent in this type of device. In this work, typical optical, mechanical and photovoltaic experiments for these devices will be demonstrated. The techniques and analysis used here can lead to the advancement of the use nanostructures in solar cells as well as many other types of optoelectronic devices. As a result, an improved method of strain balancing (SB) three-dimensional layers is developed and implemented in QD solar cells. Along with this improved technique, a reduced InAs coverage value was found to ultimately improve the device absolute power conversion efficiency by 0.5%.

Abstract Approval: Committee Chair _____

Program Director _____

Dean KGCOE _____

Acknowledgements

My Advisors:

I would like to thank Dr. Seth M. Hubbard for his monumental contribution to my doctoral education. His undying dedication to me and his other students, unequaled approachability and optimism, and his patience and eagerness to listen to students' ideas provided a working environment that encouraged innovation, hard work and a desire to investigate my own hypotheses. And also, being a good friend.

I would also like to thank Dr. Ryne P. Raffaelle for his inspiration, motivation and the opportunities provided by him both directly and indirectly. His enthusiastic direction and leadership gave me confidence during stressful times. In one instance, during the approach to a particular deadline, he arrived in the cleanroom in full 'bunny suit' on a Saturday and 'advised' me, "Put me to work, Chris!"

I would also like to thank:

- My committee: Dr. Sean Rommel, Dr. Alan Raisanen, Dr. Donald Figer.
- My parents for their unconditional support and understanding through the years.
- My sister, Jessica, for always being available for a late night phone call.
- Dr. Cory Cress, for inspirational discussions and thought experiments, some of which turned real.
- Dr. Brian Landi for encouraging me to write my first paper.
- Dr. David Forbes, for countless discussions on epitaxy and timeless humor.
- Stephen J. Polly, Esq. for his eagerness to help and learn and discuss (at Macgregor's).
- Zachary Bittner for his eager morning attitude and keeping me on my toes (good morning, sir).
- The Hubbard Project Group: Chelsea Mackos, Chris Kerestes, Michael Slocum, Adam PoV, Wyatt Strong, Yushuai Dai.
- Ryan Aguinaldo & Matthew Lomb for their simulations and discussions.
- The SMFL Team: John, Dave, Bruce and Rich.
- Dave Scheiman for aid in measurements, car problems & helpful life lessons.
- Dr. Andersen for intense and enlightening physics discussions.
- Dr. Stefan Preble for being a good and understanding professor.
- Dr. Vinnie Gupta for being an eager and helpful tutor to the world of XRD.
- Sharon Stevens for being superhuman in her understanding of the system.
- Stephanie Klenk for helping me through all the paperwork things I didn't understand.
- Elaine Van Patten for keeping the workplace lively and eventful.
- Roberta DiLeo for learning the Microsystems ropes with me.
- Dr. Annick Anctil for having more confidence in me than I had.
- Derek Schmitt and Melissa Monahan for their understanding of my work hours.
- The PV branch at the NASA Glenn Research Center for keeping my time in Cleveland eventful. Especially Mike, Barb, Jay, Eric and Anna.
- The Trifonopoulos family, Johnny, Helen and George for their family-away-from-home attitude towards me during my time in Cleveland.
- Last, but not least, my girlfriend, Elizabeth Trifon, for her constant support, and understanding nature.

Table of Contents

List of Figures

List of Tables

1. Introduction

1.1. Approaches to high efficiency

For the last decade, the energy production community in the developed world has made renewable energy sources a major focus for research. Annual funding for the National Renewable Energy Laboratory (NREL) has doubled in the past five years. Solar energy is of particular interest for the renewable resources, as it has roughly 3000 times the earth's energy requirements with any given time interval [1]. The solar private sector has strongly responded to this interest and availability, with a five hundred-fold increase in production output from 46 MW in 1990, to 23.5 GW in 2010 [2].

An important factor driving this interest is the photovoltaic (PV) device efficiency. If PV manufacturers can increase the efficiencies of a devices while maintaining the production cost, the reduction of the $/Watt metric can be obtained. NREL's 2010 Solar Technology Market Report [3] estimates current (2008) production costs at $4US/Watt. The Solar American Initiative has given research awards to those proposing technologies reducing this number further (target $1US/Watt by 2017, with a 50/50 focus on cell and module development) [4]. Developing novel technologies to meet these targets is currently driving many photovoltaic research efforts.

Of the pathways to higher efficiency, the multi-junction approach is one of the most successful. Since 1993, all of the efficiency world records have been achieved using this technology under concentrated sunlight. Multijunction cells are able to achieve such high efficiencies because of their ability to divide the absorption of the solar spectrum among multiple materials which are highly efficient for specific wavelength ranges,

minimizing thermalization and non-absorption losses. Standard lattice-matched triple junction solar cells consist of InGaP (1.85 eV/675 nm) and GaAs (1.42 eV/875 nm) monolithically grown on a Ge (0.67 eV/1850 nm) substrate. The lattice matched condition provides the ability for low-defect epitaxial layers. However, non-optimal bandgaps result from this constraint. For a three-junction device, the bottom junction is optimized to near 1 eV, but no substrate material exists which is lattice matched to GaAs at this value. The Inverted Metamorphic (IMM) solar cells enabled this condition to be circumvented. In this revolutionary device, the lattice-matched InGaP and InGaP/GaAs subcells were grown first, followed by a 9-step graded buffer stepping to a lattice constant representing a 2.2% lattice mismatch arriving at a 1 eV InGaAs bottom subcell [5]. This resulted in 1-sun 31.1% efficiency (1% absolute below world record) despite not being optimized for concentration measurements.

Other photovoltaic technologies have included unique single junction designs such as hot carrier devices [6, 7], multiple exciton generation [8, 9]. Other novel technologies take advantage of quantum wells and dots to aid in the mitigation of thermalization and non-absorption losses [10]. It is relatively well understood that quantum confinement can be used to absorb photons below the bandgap of a bulk semiconductor photovoltaic device. Quantum wells (QW), and more recently, quantum dots (QD) have been used to improve short circuit current densities [11, 12]. An increase in density of states is desirable for increased capacity for photon-separated carriers. Reduction in dimensionality to quantum mechanical length scales leads to further descretization of states as well as an increase in their density. A 2D dimensional material, or a quantum well (in which the ratio of one length scale to the other two approaches

zero) exhibits a step-function-like density of states. Further dimensional confinement, as in quantum wire (1D) or quantum dot (0D) structures, adds additional discretization and increases the density of available states. The dimensionality of confinement follows an inverse relationship, with the zero dimensional QD structures exhibiting 3D confinement. Figure 1.1 shows the various levels of dimensionality, geometry and carrier distribution, *N(E)*.

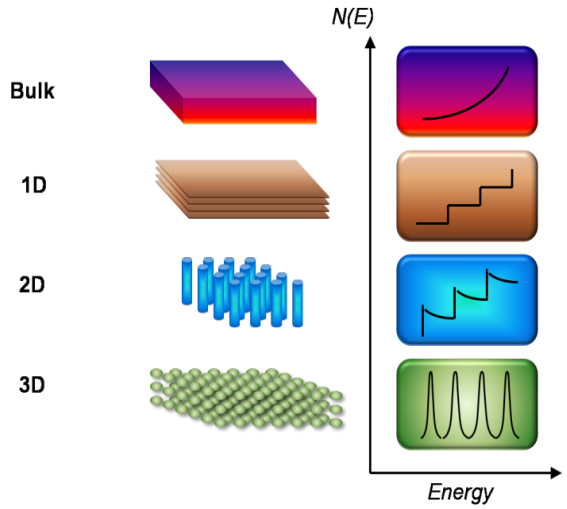

Figure 1.1. Pictorial table of various type of nanostructures. The additional dimensionality of confinement is represented in the second column by geometrical conditions and in the third column by the carrier distribution in the confined states.

Including quantum dot structures in the active region of a solar cell can give a number of significant advantages. The availability of states below the bandgap extends the absorption range of a single junction. Additionally, the improved density of states with high geometrical confinement provided by QDs can drastically enhance the absorption coefficient. Finally, the size dependence of the energy levels provides the ability to vary absorption edges of an absorber. This last trait can provide not only an advantage in single material photovoltaic devices, but can add an additional variable to the design of current-matching devices such as multijunction solar cells which typically

middle junction limited [13]. Although the multijunction solar cell is a major, outstanding motivation for this work, the focus will be primarily the investigation of the properties of InAs/GaAs QD system for the enhancement and improvement of solar cell parameters of single junction GaAs devices.

1.2. Efficiency in photovoltaic devices

1.2.1. Detailed Balance Development

Prior to discussing the ways in which nanostructures such as QDs can enhance efficiencies of single or multijunction devices, it is important to establish how PV efficiency is evaluated. In an adiabatic system in which the sun is both a sink and a source at T_s = 5760K and the cell is the same at T_c = 300K, the fundamental thermodynamic 'Carnot' efficiency can be calculated at ~95%. With the inclusion of entropy gain via a second sink (non-adiabatic system), this efficiency drops to 93.3% for these temperatures (Landsberg model [14]). Both of these methods consider perfect absorbers with no thermalization or absorption losses included. These two losses are very present in real devices and must be considered.

The efficiency calculation developed by Shockley and Queisser uses a 'detailed balance' model in which both losses are included [15]. This is calculated by including the addition of bandgap (E_g) of a single semiconductor material, and the associated absorption conditions that $h\nu > E_g$ are absorbed, but energy of value $h\nu - E_g$ is lost and all energy from photons of $h\nu < E_g$ are lost via non-absorption (transmission). It is shown that the chemical potential of the material can be substituted for E_g [16].

If a system is considered as before with the sun, cell and ambient matter radiate photons with a specific spectrum (e.g. blackbody), the exchange of energy can be evaluated by the respective temperatures of the components. Here, we take the ambient temperature to be equivalent to the cell temperature. First, effective current densities can be identified for all components of this system, where J_{rad} represents the current density required for the radiation of photons from the cell, X is the concentration factor, and F_s is the incident spectrum from the sun. The currents can be calculated as follows,

$$J_{sun} = qX\int_{E_g}^{\infty}\dot{N}(E)dE \tag{1.1}$$

$$J_{amb} = \frac{2(\pi - XF_s)}{h^3c^2}\int\frac{E^2dE}{e^{E/k_BT_c}-1} \tag{1.2}$$

$$J_{rad} = \frac{2q\pi}{h^3c^2}\int_{E_G}^{\infty}\frac{E^2}{e^{E-\Delta\mu/k_BT_c}-1}dE \tag{1.3}$$

Calculation of the current density produced from electron-hole pair generation in the device is simply the difference of the incoming and exiting representative current densities,

$$J = J_{sun} + J_{amb} - J_{rad} \tag{1.4}$$

and the voltage produced depends only on the chemical potential,

$$\Delta\mu = qV\,. \tag{1.5}$$

Using the scalar magnitude of the integrated power from the incident spectrum, the efficiency can be calculated:

$$\eta = \frac{VJ(V)}{P_S}. \tag{1.6}$$

It is important to mention that loss due to material properties and its quality such as diffusion length, mobility, and non-radiative recombination are neglected in this calculation.

The versatility of this approach can be seen with the repetition of this calculation for multiple spectra. For an Air Mass Zero (AM0) spectrum (the incident solar spectrum from just beyond the absorbing portion of the troposphere), the limiting efficiency is 31% at a bandgap of 1.3 eV. For an AM1.5 spectrum (the incident solar spectrum taking an average of daily shift of the air mass absorption coefficient, which changes as the secant of the angle between the sun and the horizon), limiting efficiency rises to 33% at a bandgap of 1.4 eV. This calculation is a fundamental application of a thermodynamic balance between a source and an absorber and is a commonly used limit when evaluating effectiveness of new material systems and novel PV devices such as nanostructured solar cells.

1.2.2. Inclusion in Triple Junction Devices

Photovoltaic devices have reached experimental efficiencies beyond this, typically using the multijunction approach. Beyond the lattice-matched condition specified in section 1.1, another limiting constraint is applied to multijunction cells. Since each junction generates current, and the subjunctions are connected in series, it follows that although the voltages add, the currents are equivalent. They are therefore restricted to the current density generated by the subjunction which contributes the least. This current-matching condition creates a limit to the efficiency of the entire device. In traditional lattice matched triple junctions, the middle junction generates the least amount of current of the three, causing it to be the limiting junction.

A detailed balance calculation for two upper junctions is applied along with 3 specific modifications from the single junction version. 1) The bottom junction is fixed at 0.67 eV assuming a Ge substrate, 2) the current matched condition is required and implemented by optimizing the efficiency using the lowest of the two subjunction current densities, and 3) the additional constraint of the filtering of the incident spectrum from the material above any given subjunction. This results in efficiency as a function both the top and bottom junctions, and can be seen as a efficiency contour plot shown in Figure 1.2 (left). The standard lattice matched triple junction is shown here with an efficiency of 33%.

In order to increase the efficiency of this theoretical device, the approach of maintaining the top cell bandgap at 1.85 eV results in a required shift of the middle cell (current limiting junction) from 1.4 eV to 1.2 eV. This effectively shifts the absorption edge of the middle junction cell and can be seen in reference to the solar spectrum in Figure 1.2 (right). Collecting photons that would otherwise transmit to the current-rich bottom junction balances junction currents, raising the upper limit of the current-matching condition. The sub-GaAs bandgap absorption of embedded QDs provides a unique path to achieve this improved current density, while maintaining the material quality of lattice matched, monolithically grown triple junction solar cell. This was proposed in literature by Raffaelle et al. [13], and is a current focus of work in our research group.

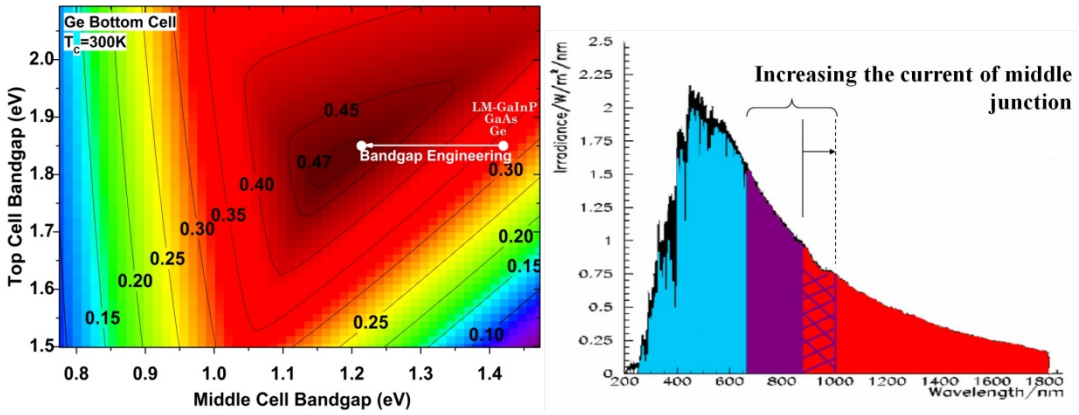

Figure 1.2. The detailed balance model applied to a triple junction solar cell with a fixed Ge bottom cell highlighting the current state of the art lattice-matched triple junction and the potential efficiency gains of lowering the middle bandgap of such a device (left). The effect of the lowering of this bandgap can be seen here represented by the adjustment of the absorption edge with respect to the incident AM0 spectrum (right).

1.3. Epitaxial QDs in PV

III-V materials lattice matched to GaAs exist only with bandgaps of higher energy. In order to reduce the middle junction (GaAs) bandgap using nanostructures, the lattice constant must depart from, and be larger than that of GaAs. This lattice mismatch is a requirement for the growth of QDs, as will be discussed in section 2.2. Layer by layer growth of lattice matched and slightly lattice mismatched material, is generally known as Frank van der Merwe growth mode, and considerable thicknesses of high quality material can be grown given a fixed substrate lattice constant. As the material lattice constant further departs from the substrate value, the surface energy increases, until a critical thickness is reached where defects may form [17]. This highly defective mode of growth is called Vollmer-Webber mode and is typically avoided for optoelectronic devices. At relatively low lattice mismatch (nominally 2-10%), a third mode of growth can be observed. First observed by Stranski and Krastinow [18], self assembled islands nucleate and grow indicating a compromise in the competition between cohesive and adhesive

forces. These islands can be maintained defect free with minimal relaxation and leave behind a characteristic 2D layer called the wetting layer (WL).

The defect-free epitaxial growth of these self-assembled, coherently strained islands was first shown to give strong luminescence properties in 1985 [19]. Subsequently, studies of using this Stranski-Krastinow (SK) growth mode for optoelectronic devices began emerging such as lasers [20, 21] and infrared (IR) detectors [22, 23]. At the same time, quantum well solar cells began to emerge based on a concept introduced in 1990 [24]. The enhancement of device performance due to the inclusion of QDs in solar cells was proposed for the first time [25] in pursuit of the Intermediate Band Solar Cell (IBSC) [26], and light IV measurements of epitaxial QD solar cells were first shown experimentally in 2005 [27]. The IBSC is of a secondary motivation for this work. QDs are the primary method of implementation of this proposed device type and will be discussed in detail in Chapter 5. The InAs/GaAs system was used here since it was, and still is, currently the most widely studied of the III-V QD material systems for optoelectronic purposes.

Despite the vast implementation of the InAs QD system in a GaAs matrix for optoelectronic device applications, there are other systems exploring QD arrays in optoelectronic devices. The binary elemental nature of InAs makes it relatively simple to grow, having single group III and V elements. A common departure from the InAs QD on GaAs is the addition of Ga, making an InGaAs ternary QD on GaAs substrates for infrared detectors [28]. Other binary QD molecules have been explored in the GaAs matrix such as GaSb [29]. Non-GaAs-based quantum dot systems have also been studied,

such as InSb on InAs [30] and InAs on InP [31, 32] for goal of improving optoelectronic devices.

The choice of InAs on GaAs is relatively straightforward. In addition to being the most widely studied III-V QD material system, the motivation for both single junction GaAs, and Ge-lattice matched multijunction solar cells make it simple to implement in existing solar cell device technology. The confinement requirement of a material of lower bandgap than GaAs (E_g = 1.4 eV) is met with InAs (E_g = 0.36 eV). The lattice mismatch of 7.2% (a_{GaAs} = 5.65 Å, and a_{InAs} = 6.05 Å), makes it an ideal candidate for the SK growth mode without the added variable of a ternary III-V alloy.

InAs has the additional property of having a relatively early onset for the effects of quantum confinement making it an attractive choice for bandgap tuning methodology. Using the de Broglie Wavelength (λ_{db}) for the determination of the onset of quantum confinement effects, the comparison of various semiconductor materials can be made. Figure 1.3 shows λ_{db} for various III-V materials and Si as a function of their effective mass. The relation is defined:

$$\lambda_{db} = \sqrt{2\pi\hbar^2 / m^* kT} \qquad 1.7$$

where $\hbar$ is the reduced Planck's constant, k is Boltzmann's constant, T is temperature in Kelvin and m^* is the electron effective mass. InSb ($m^* = 0.014m_0$) exhibits quantum effects at near 40 nm. This very high λ_{db} value allows for tuning of energy bands at feasible layer thicknesses. The value for InAs ($m^* = 0.023m_0$) is slightly smaller at 29 nm. Si and GaP have particularly high effective masses due to their electron band curvature and result in quite low wavelengths requiring extremely thin layers for confinement effects to be exploited.

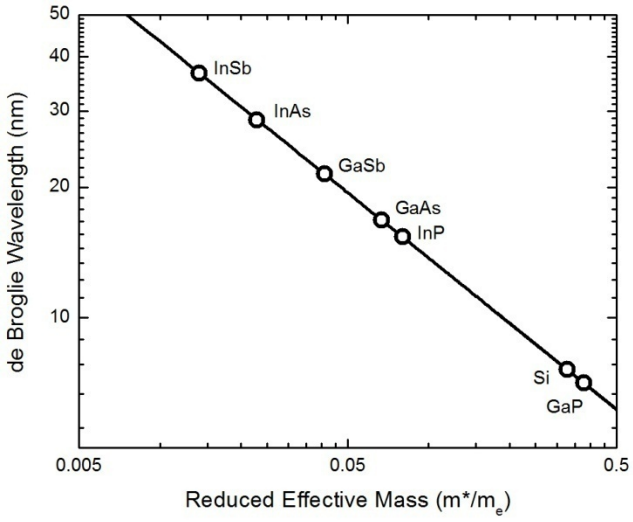

Figure 1.3. Graphical representation of the dependence of the de Broglie Wavelength on the effective mass ratio with reported values of various important semiconductor materials.

The InAs/GaAs QDs form on the order of 20-30 nm/3-6 nm in diameter/height. Both dimensions fall below the λ_{db} value, making their confinement effects easily tunable with QD size. This is seen throughout literature, with QD/barrier conduction band offsets in the range of meV [33, 34] resulting in conduction to valance band transition energies near 1.1-1.2 eV [35, 36].

1.4. Organization of thesis

The work included in this thesis involves the electrical, mechanical, and optical properties of strain-balanced InAs/GaAs QD superlattices and their inclusion in the *i*-region of *p-i-n* devices. After investigating the InAs coverage in test structures [37], devices were grown using the optimal coverage value of InAs, and losses in V_{oc} were found to be similar to existing devices in literature but with improved absolute voltage values for both QD and baseline structures [38]. QD embedded devices were subsequently grown and fabricated with higher numbers of repeat layers and improved

short circuit current, along with minimal degradation in open circuit voltage led to, for the first time, the improvement of absolute device efficiency in these devices by 0.5%.

The purpose of Chapter 1 is to give the reader an exposure to the general motivation behind the inclusion of nanostructures, in particular QDs, in photovoltaic devices. Briefly addressing the key features of this type of device, the reader is introduced to the major topics which will be scientifically explored throughout the remainder of the document.

Chapter 2 discusses photovoltaic devices and their physics both in general and under illuminated conditions. Also included is the outline of the growth and fabrication details performed at the NASA Glenn Research Center and Rochester Institute of Technology. The chapter concludes with testing and preliminary results of our devices. Chapter 3 is an overview of the strain balancing of the InAs/GaAs superlattices and the use of GaP and GaAsP as strain balancing layers in discussed. An optimal thickness evaluation is derived to arrive at the proper growth conditions and results are shown for both test and solar cell devices.

Chapter 4 outlines the theory and work performed involving evolution of QD growth within in the chamber, how it can be controlled, and how these methods can be used to obtain an optimal coverage of InAs for these types of solar cells. Test structures and devices are evaluated and ultimately, when many layers are grown, the improvement in J_{sc} is shown to be able to outweigh loss in V_{oc} resulting in improved efficiency. Chapter 5 encompasses the effects of temperature on these types of devices. The quenching of photoluminesence at high temperature, studies of bandgap and confined state variations vs. temperature, comparisons of these under both photon and

electron/hole pair injection and activation energy extract are discussed topics. Particular focus is put on the operation of the intermediate band solar cell concept as these techniques can be of use when evaluating the performance of these devices under this motivation.

Chapters 2 – 5 all include suggested next steps for the current state of the work. Chapter 6 concludes the major results of the thesis and provides a recap of the next step sections in order to provide a path forward for the research in light of current and state of the art literature and findings.

2. QD Embedded Photovoltaic Devices

2.1. High Efficiency Photovoltaics

Currently the world record solar cell is 43.5% by Solar Junction which included dilute nitride in the bottom junction [39]. Drawbacks to III-Vs include toxicity of material source, high growth cost, high substrate cost, and low to medium throughput device growth. Because of these, manufacturability can be limited further driving up cost. Often, niche markets like power conversion in space, in which manufacturing costs are dwarfed by costs of rocket propulsion fuel, opt for these types of high specific power devices. Companies like Solar Junction are evaluating and producing concentrator modules for terrestrial use of III-V materials. Besides Solar Junction, Emcore and Azur Space, are also currently pursuing this path taking advantage of the reduction in cell material provided by concentrator technology to offset the high cost of III-V materials.

2.1.1. Group III-V Devices.

Semiconductor group III (Ga, In, Al) and V (As, P, Sb) elements are used for some of the highest efficiency solar cells produced today. Their high absorption coefficients, high electron mobilities, and layer-by-layer epitaxial growth capabilities provide attractive properties for high performance electronic and optoelectronic devices. With the additional benefit of single-chamber, multiple-material growth capability, spectrum-spanning III-V multijunction technology becomes a feasible pathway to very high efficiencies.

Most III-V binary and ternary compounds feature a direct bandgap, i.e. aligned minimum and maximum band transitions at the gamma point in an E-k diagram. Figure

2.1 shows a generalization of semiconductor band structure near this point. Indirect bandgap semiconductors, like Si and Ge require a phonon interaction event. This trait results in a weak absorption coefficient. For direct bandgap semiconductors, separated electron hole pairs can populate bands without the aid of phonons (see Figure 2.1, Δk), making them ideal candidates for devices like lasers and photodetectors. With strong absorption coefficients, solar cells made from these materials can be kept thin as opposed to semiconductors like silicon and germanium.

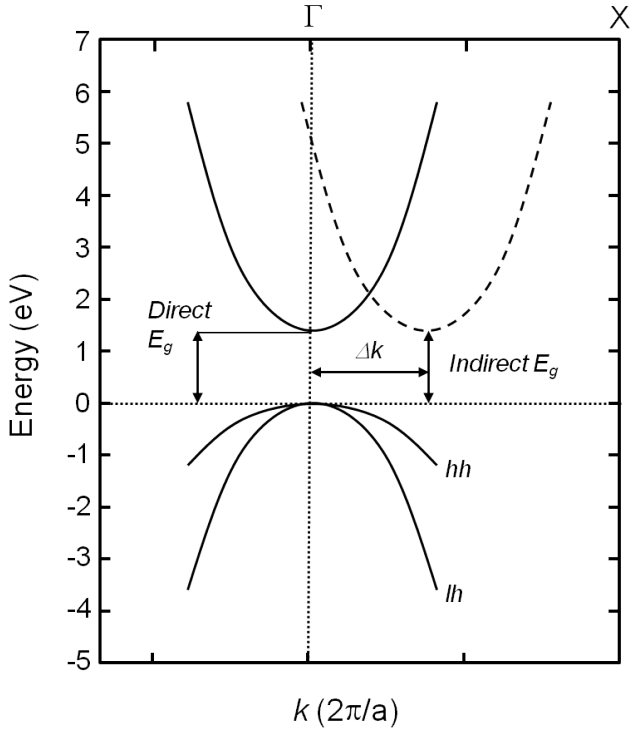

Figure 2.1. Generalized E-k diagram for semiconductor materials highlighting the Γ-point of the Brillouin Zone. For direct bandgap semiconductors, the lowest of the band minima at this point in *k*-space. Indirect bandgaps exhibit lowest transition band minima away from this point.

Additionally, the conduction band densities of states of III-V materials are typically lower for direct bandgap semiconductors due to orbital symmetry [40]. Table 2.1 shows these values for Si, InP and GaAs at room temperature and equivalent doping

values. The electron mobility of both InP and GaAs are excellent compared to Si, making them ideal for high frequency devices such as HEMTs and Lasers.

Table 2.1. Electron mobility and densities of states for important semiconductors.

Semiconductor	Type	Conduction Band Density of States ($1/cm^3$)	Electron Mobility ($cm^2/V\text{-}s$)
Silicon	Indirect	3.2e19	1400
InP	Direct	5.4e17	5400
GaAs	Direct	4.7e17	8500

The increase in mobility provided by the reduced scattering from lower densities of states in these III-V devices leads to improved diffusion lengths. The following equation combines the definition of the diffusion length, L, with the Einstein relation:

$$L_{n,p} \equiv \sqrt{D_{n,p}\tau_{n,p}} = \sqrt{\mu_{n,p}\frac{kT}{q}\tau_{n,p}} \qquad 2.1$$

where D is the diffusion coefficient, and τ is the lifetime of the p- or n-type material. Lifetimes especially in minority carrier devices like solar cells.

High electron mobilities and high absorption coefficients are generally characteristic of most III-V materials allowing these excellent electronic and optoelectronic properties to be taken advantage of for high efficiency solar cells such as multiple junction cells. Most multijunction solar cells are connected monolithically in series. Because of this, lattice constants of the materials forming the separate junctions must be lattice matched. This material constraint severely restricts the binary compounds that can be grown on any given substrate (GaAs, a = 5.6533Å or InP, a = 5.8687Å, or Germanium, a = 5.658Å). More significant to the solar cell designer, this material

constraint restricts the composition of any ternary material grown subsequently. A visual aid to any compound semiconductor grower is the bandgap vs. lattice constant chart, also known as the "crystal growers' chart." Figure 2.2 shows a version of this chart for the group III-V semiconductor materials. The lines represent a path (ternary material) between any two binary materials varying the composition. With this useful aid, it is easily seen that any vertical line drawn through the page represents a line of varying bandgap but of constant lattice parameter. With a few exceptions, solar cells are typically grown smallest bandgap first since transmission through larger bandgaps closer to the cell surface can be collected by a subsequent sub-junction. The point at which such a vertical line crosses a ternary line, the material can be grown upon the substrate below it with no internal stress or strain. Germanium's low bandgap and relatively closely matched lattice parameter, is widely used for multiple junction solar cells.

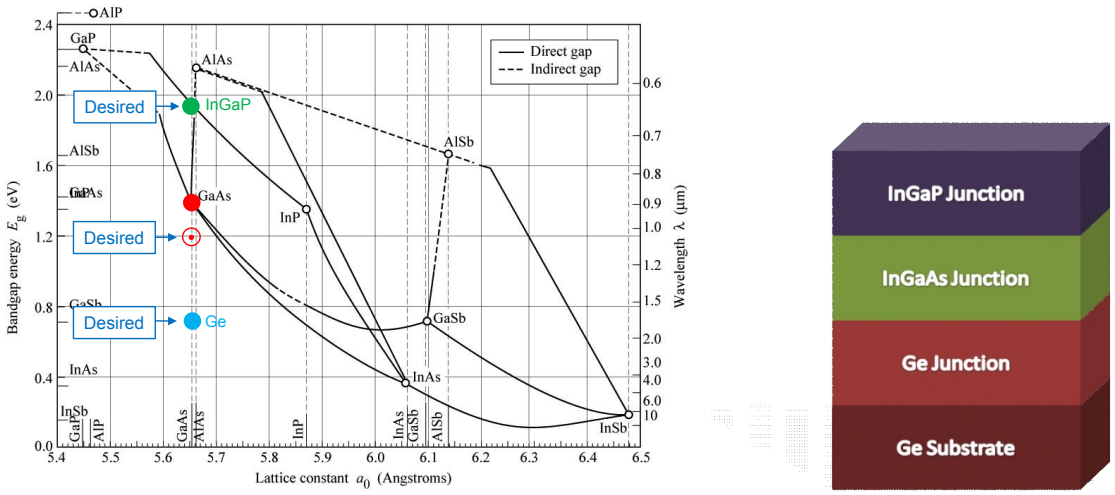

Figure 2.2**.** Left: Bandgap vs. Lattice constant chart used by III-V compound semiconductor crystal growers and designers [41] (copyright pending). Solid dots represent available latticed-matched binaries/ternaries. Right: Standard materials for a monolithically grown triple junction stack.

A detailed balance calculation reveals that given the option of three junctions, with Ge (E_g = 0.67eV) fixed as the bottom junction, the middle and top junction bandgaps are optimized to be 1.21 and 1.86eV, respectively [13]. Lattice matched InGaP (In content = 49%) gives about this value for the top bandgap, but no lattice matched material exists at the 1.21eV bandgap point. The calculation above suggests that under a one sun AM0 spectrum, a triple junction cell with these bandgaps will give a conversion efficiency of 47% [13]. Therefore tuning of this middle junction to better fit the spectrum is paramount for the space power community. The inclusion of nanostructures is proposed in this work as a method to achieve this.

2.1.2. PV Bandgap Tuning with Nanostructures.

The use of layers of quantum confined material inside a solar cell was been suggested, as mentioned earlier, by Barnham and Duggan [24] and realized by Barnham and others [11, 42, 43]. The ability to tune the bandgap can be implemented here to attain the lower bandgap need of the middle junction (1.21eV). With the GaAs (E_g = 1.42eV) embedded with InAs QDs (typical ground state absorption 1.0-1.1eV [35]), an "average" bandgap can be estimated to have values much closer to this preferred energy. 'Bandgap tuning' has the potential use as a tool to achieve bandgaps otherwise inaccessible.

The pursuit of the IBSC is a more specific, focused use of quantum confined material within a solar cell. This concept, proposed by Marti and Luque, hypothesizes that intermediate level states or 'minibands' provided by wavefunction coupling between embedded nanostructures provide photon absorption capability from both valence to intermediate and intermediate to conduction bands [26]. This functionality reduces

transmission loss much like a multijunction cell and gives a detailed balance efficiency value of 63% with an optimized energy transitions. Their result corresponds to a total host bandgap of 1.93eV, with the intermediate band at 1.23eV from the valence band. Their theory has very specific assumptions, most of which are quite unrealistic at this technology juncture, such as a concentration value of 46,000 suns, no non-radiative recombination, and infinite carrier mobilities [26]. Quantum well structures would otherwise be useful for this concept except that the isolation requirement of the intermediate band can only be ideally satisfied by a band with zero-dimensional density of states [44]. For this reason, this concept has drawn much attention to solar cells embedded with QDs as the most viable means of realizing such a device [45]. It is these two potential solar technologies that motivate the work done here.

2.2. Photovoltaic Operation and Testing

Photons striking a uniformly doped single material semiconductor generate electrons and holes, which relax back to their equilibrium state. Solar cells make use of this photovoltaic effect in which device asymmetry is used to collect the separated charge prior to relaxation. The asymmetry is provided by reversing the doping polarity within a bulk semiconductor material, producing a p/n or n/p junction. Virtually all solar cells operate using this type of asymmetry making the physics of the p/n junction fundamental to the understanding of photovoltaic device operation.

2.2.1. The p/n junction

A metallurgical junction is formed in a material when a semiconductor with excess acceptors (p-type) meets an interface with a material with excess donors (n-type).

A depletion region forms at this interface creating a natural intrinsic layer between the extrinsic (doped) layers. Evaluation of this *i*-region can be followed by a standard electrostatics treatment of device material, doping levels and thicknesses. Using Poisson's equation:

$$\nabla^2\phi = \frac{q}{E}\left(n_0 - p_0 + N_A^- - N_D^+\right) \qquad 2.2$$

we can convert the doping profile into an electrostatic potential (ϕ), where N is the concentration of the respective dopant. By integrating the profile of this potential, we can arrive at the built-in voltage (V_{bi}). In the case of an abrupt junction device,

$$V_{bi} = \frac{kT}{q}\ln\left(\frac{N_A N_D}{n_i^2}\right) \qquad 2.3$$

and these values are typically 1.2-1.5 for GaAs and 0.8 to 1.1 for Si (depending on doping level) [46]. V_{bi} can be an important metric in solar cells, as it is directly proportional to the open circuit voltage of a device and is shown in Figure 2.3, below. Ultimately, depletion width can be calculated from this value. As it may be desirable for improved absorption and collection purposes, an *i*-region maybe artificially inserted into an abrupt junction design to enhance device performance.

To this point we have discussed the statics of p/n junctions, yet the electrodynamics of these devices reveal the fundamental operation of photovoltaic action. In order to examine the influence of generated electron hole pairs, the existing currents in a p/n junction will be briefly discussed first. Currents in the junction, under no illumination, are dominated by both drift and diffusion components based on location within the junction. In the *i*-region, there is a strong electric field present due to the

missing excess carriers, inducing drift as the dominating current flow mechanism. In the quasi-neutral regions, diffusion is predominant. These regions are depicted for a device at equilibrium in Figure 2.3. The energy of the conduction, valence and Fermi level are shown as E_c, E_v and E_f, respectively.

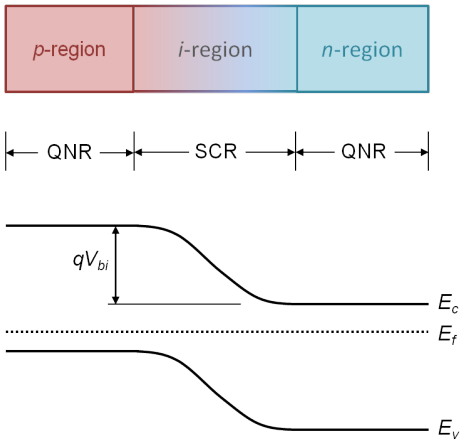

Figure 2.3**.** The three regions of a p-n junction and the electronic band structure at equilibrium.

At equilibrium, these competing currents can be evaluated algebraically with the total current relationship:

$$J_{eq} = J_n + J_p \tag{2.4}$$

$$J_n = J_{n|drift} + J_{n|diffusion} = q\mu_n nE + qD_n \nabla n \tag{2.5}$$

$$J_p = J_{p|drift} + J_{p|diffusion} = q\mu_p pE - qD_p \nabla p\,. \tag{2.6}$$

In equations 2.5 and 2.6, the components of the current are separated with the first term resulting from the drift associated with the electric field, E, and the mobility and carrier populations. The second term describes the current purely associated with the spatial non-uniformity of carrier populations and results in the current contribution from diffusion action.

Under applied bias, a term describing the current from the space charge region becomes significant and an exponential relationship with the applied voltage which is

derived from the Fermi-Dirac statistics of a semiconductor. The differences in band structure under applied bias can be seen in Figure 2.4. The energy offset in either band is now reduced by the applied voltage. The diffusion of excess majority carriers increases significantly outweighs the drift component which has been further reduced from the decrease in electric field. The correct application of ohmic contacts, this current can be extracted as a function of voltage applied, resulting in a *J-V* relationship.

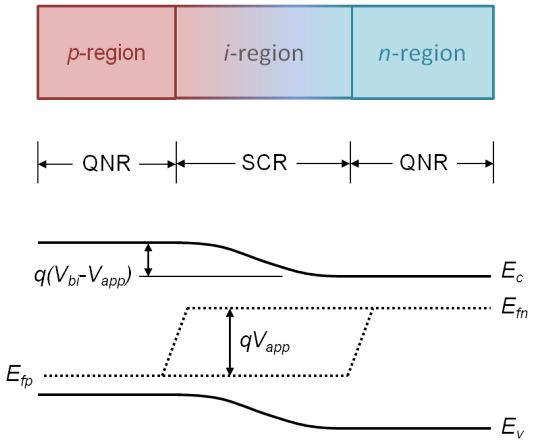

Figure 2.4**.** The three regions of a p-n junction and the electronic band structure under applied bias.

Additionally, in high-quality, direct bandgap semiconductors, radiative recombination currents (also exponentially dependent on voltage) can become significant. These conditions result in a current-voltage relationship as follows:

$$J_{dark} = J_{diff|0}\left(e^{qV/kT} - 1\right) + J_{scr|0}\left(e^{qV/2kT} - 1\right) + J_{rad|0}\left(e^{qV/kT} - 1\right) \quad 2.7$$

$$J_{diff|0} = qn_i^2\left(\frac{D_n}{N_a L_n} + \frac{D_p}{N_d L_p}\right) \quad 2.8$$

$$J_{scr|0} = \frac{qn_i\left(w_n + w_p\right)}{\sqrt{\tau_n \tau_p}}. \quad 2.9$$

where J_{dark} is the total current in the device as a function of voltage, J_{diff} and J_{scr} envelope the diffusion and drift components discussed above and J_{rad} is the radiative recombination portion (which can have significance in high quality materials with direct bandgaps). This is a form of the diode equation. Of note here in equation 2.7 is that the voltage dependencies differ by the denominator in the exponential, termed the ideality (n). For both diffusion and radiatively limited devices, this value tends toward $n = 1$, and in the case of poor material quality and/or low injection operation, the effects of recombination in trap states in the space charge region dominate the dark current and this ideality approaches $n = 2$. The interaction of a semiconductor with light adds another term to this equation which will be discussed in the next section.

2.2.2. The illuminated p/n junction

Under illumination, generation and recombination have affects the carrier populations in the material and alters these equations. Generation of carriers from incident photons provide additional terms in the equations used to derive equation(s) 2.7 through 2.9. These sum to a value of light-induced current called the short circuit current density, J_{sc}:

$$J_{sc} = \int_0^\infty j_{sc}(E)dE = \int_0^\infty \left[- j_n(E) - j_p(E) - j_{scr}(E) \right] dE \qquad 2.10$$

The individual light-generated current terms are energy dependent and can be calculated from the incident spectrum, b_s, reflectance, R, and the absorption coefficient, α. This relationship is shown here for the example of $j_n(E)$:

$$j_n(E) = q b_s(E)(1 - R(E))e^{-\alpha(E)x} \qquad 2.11$$

This relationship is used for all regions of the device, and x is representative of the current contribution of the particular region of the device. Here, the dependence of semiconductor material can be evaluated. The absorption coefficient is dependent on the density of states and can be approximated as:

$$\alpha(E) = \alpha_0 \left(E - E_g\right)^{1/2} \tag{2.12}$$

Clearly, at E equal to E_g, the absorption coefficient drops to zero, and at $E < E_g$, is undefined, representing transmission of light through a material at wavelengths higher than that of the absorption edge. The inclusion of nanostructures in devices potentially extends this absorption range and can therefore have a direct positive effect on the short circuit current density.

This short circuit current density is voltage independent and is added as a term in the diode equation that is constant with respect to voltage:

$$J(V) = J_{diff|0}\left(e^{qV/kT}\right) + J_{scr|0}\left(e^{qV/2kT}\right) + J_{rad|0}\left(e^{qV/kT}\right) - J_{sc} \tag{2.13}$$

This is the light-based diode equation and is competitive in nature with the other dark currents in the device and offsets the diode curve at all values of V, by the J_{sc} value. The point on the diode curve described by equation 2.13 where the dark current terms exactly cancel the light generated current is known as the open circuit voltage. At this point the diffusion and radiative terms are dominant, and the J_{scr} term can be neglected. Setting the By this definition, setting the $J(V)$ term to zero, plugging in V_{oc} for the voltage, and rearranging this simplified equation gives:

$$V_{oc} = \frac{nkT}{q} \ln\left(\frac{J_{sc}}{J_0} + 1\right) \tag{2.14}$$

in which case, the J_0 factor is dominant dark current value at short circuit current, called the saturation current, and is described by equation 2.8. This parameter has a strong influence on the open circuit voltage and is an important metric in determining material quality of a solar cell. It is strongly and moderately dependent on the intrinsic carrier concentration, n_i, and the diffusion coefficient, D of the material. Table 2.2 shows these values in diffusion limited device regime for important photovoltaic semiconductors at typical doping levels.

Table 2.2. Intrinsic carrier concentration and saturation current densities for important photovoltaic semiconductors.

Semiconductor	n_i	D_n	D_n	J_0
	($1/cm^3$)	($1/cm^2$-s)		(A/cm^2)
Silicon	1.0×10^{10}	36	12	1.2×10^{-12}
InP	1.3×10^{7}	130	5	6.2×10^{-18}
GaAs	2.1×10^{6}	200	10	2.3×10^{-19}

Typical open circuit voltage values generally track with these with $V_{oc|GaAs} > V_{oc|InP} > V_{oc|Si}$. This correlates with the dependence of n_i on E_g: $n_i^2 \propto e^{-E_g}$. Because of the dependence of the saturation current on material quality, evident through its dependence on the diffusion coefficient, keeping material quality high directly improves the open circuit voltage values of photovoltaic devices.

The open circuit voltage and short circuit current are important extractable parameters that can be obtained from a light-IV measurement, as discussed in the next section. They, along with the fill factor, ultimately determine a solar cell efficiency, as we will see in the next section.

2.2.3. Devices Under Test

Testing state of the art solar cells requires equipment that allows comparison of results to those in the research community. Efficiency is calculated from illuminated current density (J) vs. voltage (V) measurements (light J-V curve). Precise control of the space solar spectrum is obtained using NASA certified calibration solar cells along with an air mass zero (AM0) filter. The terrestrial solar spectrum is calibrated using NREL certified solar cells under an air mass 1.5 (AM1.5) filter. A TS Space Systems Class A solar simulator along with a Newport single source xenon lamp were used to generate the spectrum. Figure 2.5 shows the close-matched nature of this simulator at RIT along with the ASTM AM0 spectrum. Spikes in the visible wavelength region are due to the spectrum lines typical of a xenon bulb.

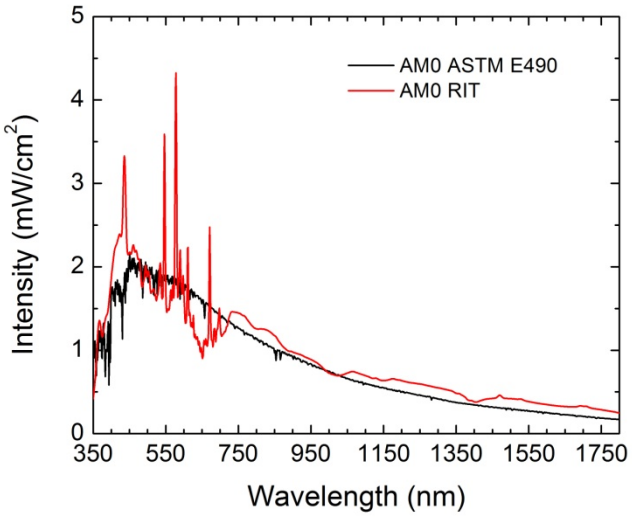

Figure 2.5**.** The ASTM standard AM0 spectrum overlaid with the AM0 filtered simulated spectrum generated by the TS Space Systems solar simulator at RIT.

With the provided simulation of the spectrum under AM0 conditions, a light J-V curve obtained from one of our GaAs baseline cells is shown in Figure 2.6. The diode

behavior of these *p-i-n* solar cells, provide the *J-V* behavior shown in the red dashed curve.

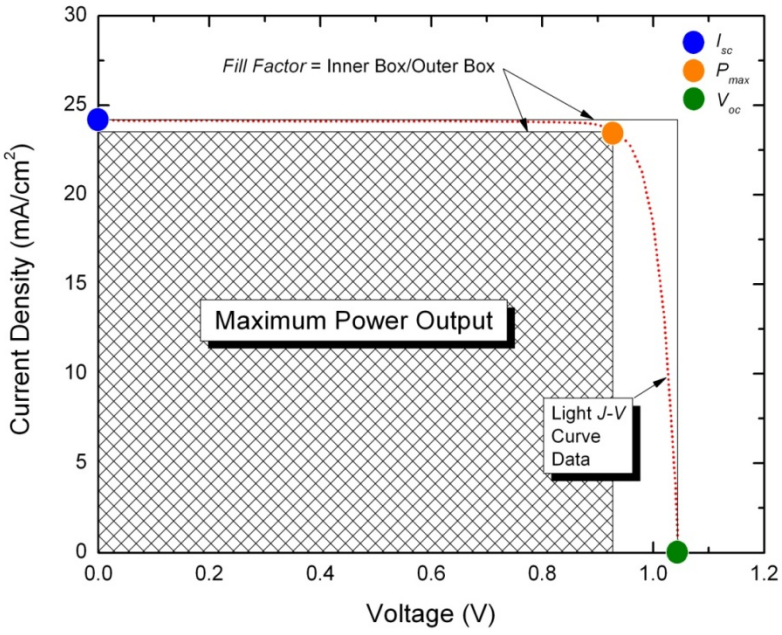

Figure 2.6**.** Light J-V curve indicating important extractable solar cell parameters from data.

A typical illuminated measurement lies in the fourth quadrant, but is commonly mirrored into quadrant one for ease of display. In this plot, it is easy to see the parameters that are of importance in solar power production. The blue dot indicates the short circuit current density (0 V) under this specific illumination condition. The point at which the current is zero (or where the light-generated current is equal to the forward bias-induced current) is the open circuit voltage and indicated with a green dot in Figure 2.6. The product of any current density value with its corresponding voltage value, give the particular power density at that given point on *J-V* curve. The location at which this product is maximized is denoted as the maximum power point, and is labeled on the plot

in orange. The power generated here divided by the power of the incident spectrum gives the device efficiency. Equation 2.15 shows this quotient and its constituents,

$$\eta = \frac{P_{\max}}{P_{inc}} = \frac{J_{\max}V_{\max}}{P_{inc}} = FF\frac{J_{sc}V_{oc}}{P_{inc}} \qquad 2.15$$

where J_{max} and V_{max} are the current density and voltage values at the maximum power point. Also from this curve, we can obtain the device fill factor (*FF*), which collects losses from shunt and series resistance in a single ratio. Graphically, it is the ratio of the shaded box and the bigger box (defined by J_{sc} and V_{oc}). In equation 2.16, we have,

$$FF = \frac{P_{\max}}{J_{sc}V_{oc}} = \frac{J_{\max}V_{\max}}{J_{sc}V_{oc}} \qquad 2.16$$

The fill factor is a single, quantitative metric describing the departure from an ideal diode by losses such as series and shunt resistance. Series resistance becomes significant when there is internal voltage reduction throughout a device. The most significant loss in FF, for high-quality solar cell materials, is ohmic contact resistance, R_s. The diode equation is altered by including both series and shunt resistance, R_{sh}, as follows.

$$J(V) = J_0\left(e^{q(V+JAR_s)/kt} - 1\right) + \frac{V + JAR_s}{R_{sh}} - J_{sc} \qquad 2.17$$

From this, it is clear that shunt (series) resistance must be maximized (minimized) to obtain a minimized 2nd term, or ratio, in this equation. At any given voltage, the size of this ratio will determine the squareness of the diode, and can be represented by the fill factor.

Current generation in a junction (or multiple junctions) can be experimentally spectrally resolved by obtaining characteristic spectral responsivity (*SR*) measurements. Spectral responsivity is a measure of a photo-electrical conversion as a function of the

spectral wavelength and is very sensitive to the material quality. Taking equation 2.10 and dividing out the spectrum, we get:

$$SR(E) = \frac{1}{qb_s(E)(1-R(E))} j_{sc}(E) \qquad 2.18$$

where $j_{sc}(E)$ is the integrand of equation 2.10. This integrand, j_{sc}, is a sum of the current contributions from different regions of the solar cell. In this way, a reduction in the *SR* can be directly associated with a loss in a particular region's diffusion length. This can be useful in determining the identification of losses within a *p-i-n* junction.

The technique allows calibrated incoming monochromatic light to be absorbed and converted by the cell, while a wavelength-specific short circuit current is measured. This *SR* measurement can then be converted to an external quantum efficiency value (*EQE*) which is also spectrally resolved, but is independent of the photon energy. This can be calculated from the *SR* using equation 2.19:

$$EQE = \frac{(1240eV * nm)(SR)}{\lambda} \qquad 2.19$$

where λ is the specific wavelength of the given *SR* data point. Quantum efficiency is a well known optoelectronic metric and is used for LEDs and photodetectors. A plot of the experimental external quantum efficiency for a single junction GaAs solar cell is shown in Figure 2.7. This was taken using an Optronics Laboratories 750 series spectroradiometer equipped with an internal lock-in amplifier at 167 Hz. Here, we can see the peak is about 71% at 700nm. If this cell was a perfect absorber, it would give 100% at all wavelengths. Much of the light hitting the solar cell is reflected (almost 30% averaged over the wavelength) and light at energies lower than the electronic bandgap is

transmitted. If these are taken into account, the plot gives internal quantum efficiency (*IQE*) and is much closer to 100%. This can be seen in the following equation:

$$IQE(E) = \frac{EQE(E)}{1 - R(E) - T(E)} \qquad 2.20$$

where *T(E)* is the transmission of light as a function of photon energy.

Also of note here is the semiconductor's absorption bandedge. The bandgap of GaAs is 1.42eV at 300K. This is equivalent to energies of photons with wavelengths of about 880nm and below. This is shown here as the *EQE* quickly drops to 0% at or near this wavelength value. This can be seen in equation 2.20 as a transmission of unity at these wavelengths. Photons with energy less than the bandgap will not be absorbed by the material, and therefore the smaller the bandgap, the more current the junction will generate. However, since voltage is highly dependent on the bandgap of the material as well, a smaller bandgap will results in a lower voltage. This tradeoff has been outlined in Chapter 1 using the detailed balance calculation. It is in this manner that QDs show the potential of lowering the bandgap to gather more of the sun's emitted photons, without sacrificing the higher voltages of the host bandgap.

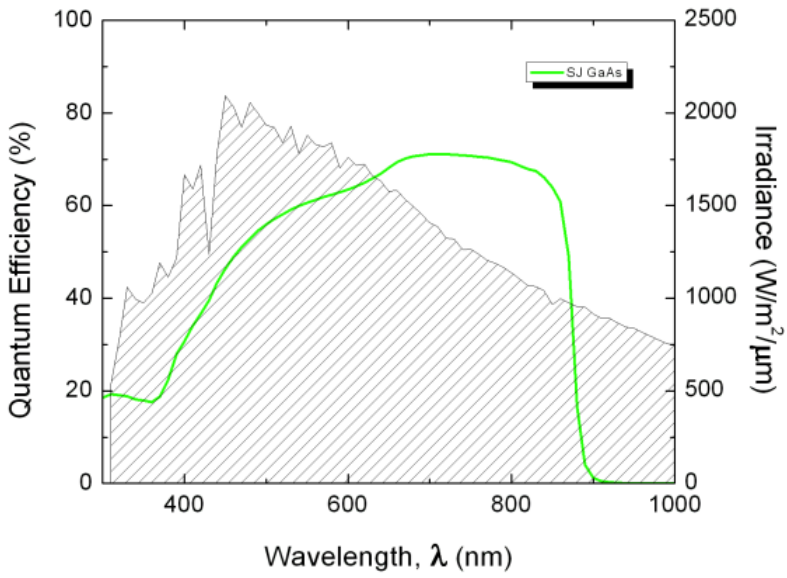

Figure 2.7. Spectral resolution of current generation in SJ GaAs solar cell overlaid on the AM0 solar spectrum.

Throughout the next four chapters, the work completed will be shown in order to provide preliminary details on how these devices can be improved upon with the ultimate goal of improving solar cell efficiency, while also further characterizing the phenomenon of in the insertion of low dimensional, quantum confined structures into optoelectronic devices with the specific focus on photovoltaic energy conversion.

2.3. Device Design

The design of a solar cell layer structure the layer structure of a solar cell, of the utmost importance can be the layer doping and thicknesses. Higher doping will widen the chemical potential, improving the open circuit voltage, while also decreasing diffusion length and mobility due to scattering effects. Layer thickness follows a similar optimization, with the necessity to be thick enough for maximum absorption, but remaining on the order of the diffusion length to avoid recombination of minority carriers

prior to reaching the junction. The absorption of photons decays exponentially into the cell based on the Beer-Lambert law:

$$I = I_0 e^{-\alpha x} \tag{2.21}$$

where α is the absorption coefficient of the material. This leads to the same exponential dependence of carriers generated throughout the material. Therefore, it is necessary to place the physical junction (i.e. point of highest electric field) near the approximate halfway point of this generation function. Additionally, since the majority of the carriers are generated near the surface, a highly doped emitter layer (quasi-neutral region closest to the incident photon flux) to ensure efficient minority carrier collection. These two constraints lead to designs with much thinner emitters (100-700 nm) than base (quasi-neutral region physically beneath the emitter and *i*-region) layers (few microns). In this section, we will outline the basic device design used at RIT in more detail and subsequently discuss the modifications necessary to incorporate nanostructured superlattices.

2.3.1. The p/i/n junction

The *p*-*i*-*n* junction is often used in III-V solar cells (and particularly in amorphous Si) as it is simple to grow epitaxially (as opposed to diffusion-created junctions often used in crystalline Si). An extended *i*-region is advantageous for the exploitation of an higher absorption volume of low-doped, higher lifetime material. The extended electric field increases the ratio of drift-driven to diffusion-driven carriers. This is especially important in minority carrier devices in which carriers photogenerated in quasi-neutral regions have a likelihood of not reaching the junction. Since devices used for this work make use of QD-embedded superlattices placed in the high-electric field region, it is also

convenient to have a comparable *i*-region thickness for comparable nanostructure-excluded control, or baseline cells. An outline of the layer structure for the basic GaAs cell is included in this section.

2.3.2. Growth and Fabrication

The materials used in this work are predominantly lattice-matched to GaAs. This is the clear choice for the investigation of GaAs-lattice-matched triple junction devices and therefore results from this work can easily transfer to that system. as that is the cheapest III-V substrate, and in-depth studies of the InAs/GaAs QD material system requires a GaAs host. The single junction solar cells used for these studies are comprised of the following layers grown on the n-type substrate (in order of growth):

1. 250 nm n-type Si doped GaAs epitaxial seed layer
2. 50 nm n-type Si doped 1 x 10^{18} cm^{-3} InGaP "window" layer used for blocking minority carrier holes from diffusing to the n-type contact layer
3. 2000 nm n-type Si doped 1 x 10^{17} cm^{-3} GaAs base layer
4. 100 nm unintentionally doped n-type 5 x 10^{15} cm^{-3} GaAs *i*-region layer
5. 500 nm p-type Zn doped 1 x 10^{18} cm^{-3} GaAs emitter layer
6. 50 nm p-type Zn doped 2 x 10^{18} cm^{-3} InGaP "window" layer used to reduce front surface recombination
7. 160 nm p-type C doped 2 x 10^{20} cm^{-3} GaAs contact layer

All layers are grown in a Veeco 3 x 2" rotating disk metal chemical vapor deposition (MOCVD) reactor shown in Figure 2.8. Precursor metal-organic alkyl gases used for the epitaxial layers include Trimethylgallium (TMGa), Trimethylindium (TMIn)

for the group III elements, and precursor hydrides used include Arsine (AsH_3) and Phosphine (PH_3), for the group V elements. N-type dopant sources used are Diethyltelluride (DETe) and Disilane (Si_2H_6). P-type dopant sources used are Diethylzinc (DEZn) and Carbon Tetrachloride (CCl_4). Temperatures for most GaAs and InGaP layer ranged between 575 and 675C. Chamber pressures are typically held at 60 Torr for standard bulk growth. Typical growth rates under these conditions vary from 1-2 μm/hr depending on material. For bulk GaAs and InGaP layers, the V/III ratio was 58, maintaining the AsH_3 overpressure necessary to prevent the formation of group III metal islands.

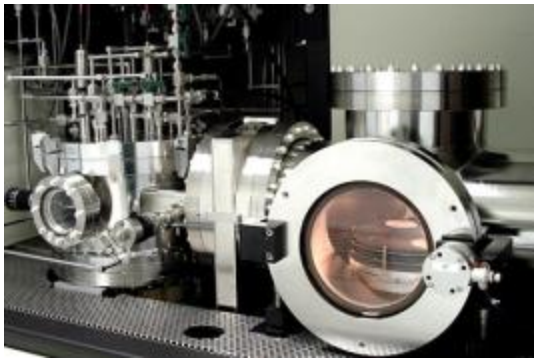

Figure 2.8**.** Image of the MOCVD reactor at the NASA Glenn Research Center.

Figure 2.9 shows the layer structure described above, with the addition of multiple-layer QD superlattice in place of the 100nm intrinsic layer. The embedded QD superlattice layer structure consists from five to one hundred repeat units of the following 5 layers in growth order:

1. InAs wetting layer and QD array
2. Low temperature GaAs capping layer
3. High temperature GaAs spacer layer
4. GaP strain balancing layer

5. High temperature GaAs spacer

Epitaxial QD arrays are grown by the Stranski-Krastinow (SK) growth method elaborated on in a later section. Typical growth temperatures for this growth mechanism are 100-200°C lower than is required for the growth of high quality GaAs bulk and spacer layers. Growth temperatures are raised to 575°C for the remaining GaAs and GaP layers to avoid low-quality defective 2D layers typical of low temperature growth. To prevent InAs from evaporating during this rise in temperature, a thin (2.1 nm) GaAs layer is deposited before the temperature increase. The GaAs (4.6 nm), GaP (1 nm, nominal) and subsequent GaAs (4.6 nm) layers are all grown at the higher temperature before returning to 490°C for the beginning of the next repeat unit (InAs). This sequence is repeated for the desired number of repeat units, each of which results in approximately 14 nm of material. For reference, this results in *i*-region thicknesses of 140 nm for a 10-layer repeat unit structure, and 560 nm for a 40-layer QD superlattice. The GaP and high temperature GaAs spacer thicknesses are varied for particular studies which will be addressed in subsequent chapters.

The procedure for growth of solar cells embedded with these superlattices, are varied only after the base layer (GaAs) is completed. After the desired superlattice is complete, 33 nm of unintentionally doped GaAs is grown at 620°C. The doped emitter layer then continues the sequence identical to a solar cell without a superlattice-embedded *i*-region. For test structures grown for this study were grown with the same 250 nm epitaxial seed layer, followed by the superlattice discussed above. A 33 nm GaAs cap layer is then deposited for quantum mechanical barrier isolation of the multiple quantum dot layers. A layer of InAs wetting layer and QDs is then grown on the surface

as the final layer for surface characterization using Atomic Force Microscopy (AFM). Growth and optical, electrical and mechanical characterization of these arrays and their superlattices are deeply investigated in further sections and chapters.

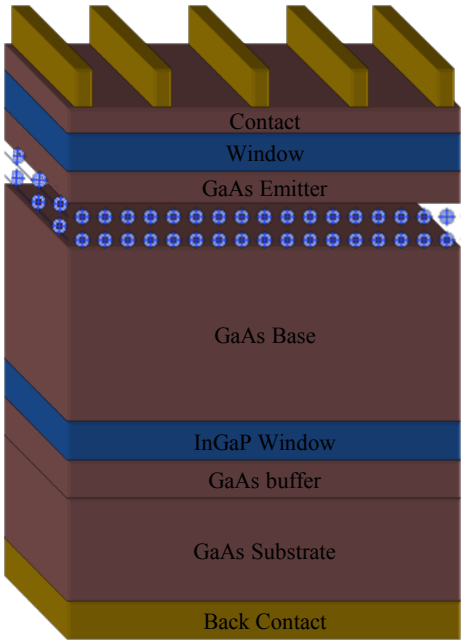

Figure 2.9**.** Cross section of GaAs single junction solar cell embedded with QDs.

This is then followed by the typical metallization contact layer as in step 6 of the GaAs cell. Quantum dot embedded solar cells are grown in the intrinsic region of the GaAs junction, replacing step 3 in the growth steps (and as depicted in Figure 2.9).

Standard solar cell fabrication processing is used to make epitaxially grown layers into actual power producing solar cells. The device is contacted on both the top and bottom of the device, with metallization systems that accommodate both p-type and n-type GaAs. P-type GaAs allows for ohmic contacting to metals with lower work functions, such as eutectics of Au-Zn, Ag-In, Ag-Zn and In-Zn [47]. In this work, the Au-

Zn alloy is used. A final layer of thick, current-carrying Au is the deposited. Au is chosen for its low reactivity and high conductivity. Zn has a fairly low melting temperature lending itself well to thermal evaporation systems. For n-type ohmic contacts, the Au-Ge alloy is used. This alloy is chosen since, for p-on-n devices, the n-type doped side of the device is a 300 nm thick substrate. Ge has a very high diffusion coefficient in GaAs, but can afford to be used here since there is low chance of the Ge atoms to puncture the physical junction, preventing carrier shunt pathways. Other potential n-type metallization layers include Au-Si, Au-Te and also Ag-In [47]. All metallization is performed with thermal evaporation equipment, and alloys are sequentially deposited during the same low pressure ($< 10^{-6}$ torr) chamber evacuation.

An annealing step is then used for the diffusion of the metal/alloy into the semiconductor lattice. This was optimized by testing various temperatures and minimizing the contact resistance using a standard semiconductor TLM method. P-type metallization was found to give the best results at 406°C and n-type metallization was optimized at 372°C. For this reason, typically the p-type anneal is performed prior to the n-type anneal.

Lift-off photolithography is used for patterning of the current distribution grid. The non-photoactive lift-off resist, LOR-10A is used in two spin-cast (3000 rpm)/bake steps of 1 um thickness each. The bake temperature used was 180°C, for 6 minutes. A photoactive resist layer is then deposited. MicroChem Microposit S1813 is spin-cast at 3000 rpm and baked

The photoactive resist is exposed through a patterned, chrome coated photolithography mask. The mask includes seven 1 x 1 cm^2 cells designed for 1 sun

illumination. Also included are three 1 x 0.5 cm^2 concentrator-designed grid cells, two quantum efficiency pads, transmission line model (TLM) measurement pads A broadband/g-line ultraviolet light source was calibrated to 10 mW/cm^2 irradiance. A 12.5 second exposure provides an energy density (dose) of 125 mJ/cm^2. A photoresist development step is then performed using MicroChem Microposit MF CD26 developer solution, after a Hexa-Methyl Disilizane (HMDS) surfactant surface preparation. After a two minute developer immersion (approximately 1 minute for the photoactive layer, and 1 minute for the development of the LOR resist), the wafers are rinsed with de-ionized water, and dried with a nitrogen jet. After the image is transferred into the photoresist pattern, An overhang sidewall profile remains due to the isotropic dissolution of the LOR resist. Thermally deposited metallization is then applied. To realize the grid structure and remove the underlying resist, a strong polar solvent, N-methyl Pyrrolidinone is used (Nano Remover PG by Microchem) for the removal of all photoresist, lifting off the metal of the negative image of the mask, leaving only the desired pattern. The annealing step is then performed described above.

For the isolation of the cells and a wet-chemical mesa isolation step is then used to define (physically and electrically) the dimensions of the cell. A simpler photolithographic process is used for masking the etchant. For this process, approximately 1 μm of S1813 photoresist is deposited after an HMDS surface preparation. A 60 second exposure is used under the same dose as above, followed by a 1 min bake at 115°C and a 2 minute develop in MF CD-26 developer agent.

Common etches for III-V materials make use of acids such as HCl, H_3PO_4, and H_2SO_4. These are typically combined with an oxidizer such as H_2O_2 and can be diluted in

H_2O. For this work, a mixture of H_3PO_4, H_2O_2, and water (in a ratio of 3:4:1) is used for the etching of (100) oriented GaAs layers. The phosphoric acid is particularly suited for binaries ending in -As group V elements. It is an aggressive GaAs etch with etch rate of 0.16 μm/s. The hydrogen peroxide oxidizes the semiconductor, upon which the acid dissolves the oxide. The anisotropic nature of the phosphoric acid mixture results in the slowest etch rate in the {100} plane family [47]. For a (100) surface, this etch results in a 90° sidewall. HCl is commonly used for P-ending group V compounds. For the InGaP layers, this was used without dilution, providing an etch rate of 0.3 μm/s.

All photolithography, liftoff resist dissolution, and wet chemical etches were performed in a class 1000 cleanroom at RIT. When possible, experimental QD solar cells are fabricated in tandem with SJ GaAs control cells, or "baselines."

2.4. Growth of QDs

2.4.1. Strain in Epitaxial Layers

The deposition of epitaxially grown material by either Molecular Beam Epitaxy (MBE) or MOCVD is controlled on the atomic level and very abrupt interfaces between layered materials can be realized [48]. One of the essential mechanical properties of these heterostructured materials is the lattice constant, a_0. This value, in an unstrained environment is a result of the delicate competition between ionic and covalent force interaction in compound semiconductors between, for instance, the binary atoms (Ga, As) in GaAs. This energy minimization results in this natural atomic distance, a_0. As a layer of a material is deposited by either of these techniques, the lattice constant of the substrate is replicated by the newly deposited layer, regardless of its own lattice

parameter. This property is called coherent growth and a layer with the same lattice parameter as the underlying material is called lattice-matched.

When a material is lattice-mismatched, or the deposited material has a lattice parameter slightly larger, or smaller than the underlying material, a phenomenon called tetragonal distortion occurs depicted in Figure 2.10 (left). When atoms of one lattice parameter (a_0), are forced to a different value ($a_{||}$), the minimum energy formation of the unit cell is altered, and the lattice parameter in the growth direction ($a_{\perp}$) shifts to accommodate. This is shown in this figure for both materials with both smaller and larger lattice constants than the substrate material beneath, resulting in material in tension and compression, respectively, in the in-plane direction. Assuming zero relaxation of the lattice, this geometry persists through the extent of the layer thickness.

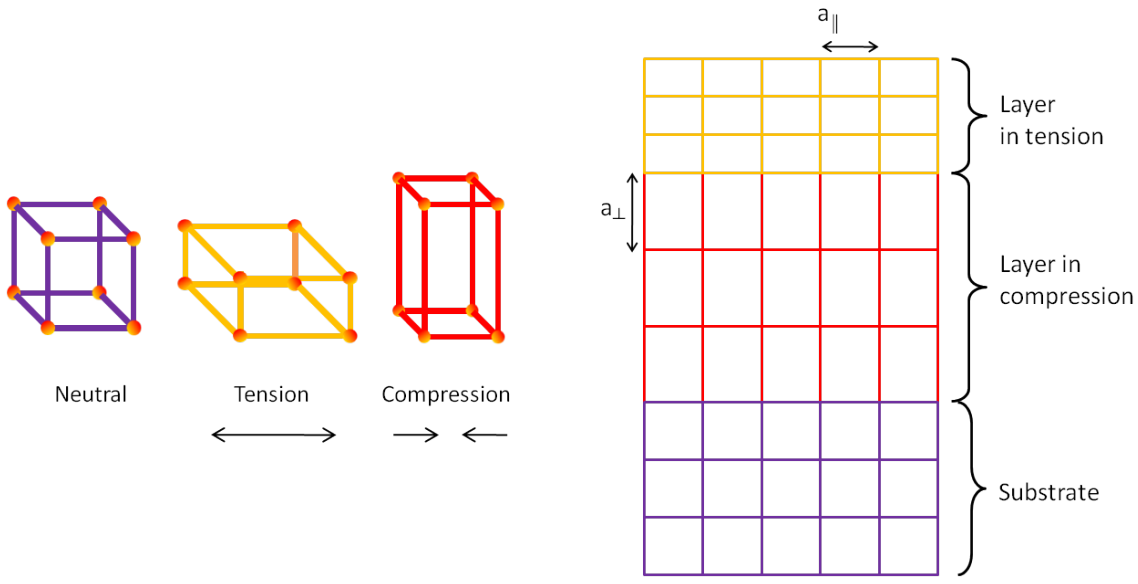

Figure 2.10. Illustration of tetragonal distortion and its two and three dimensional representations.

Tetragonal distortion directly affects the out-of-plane lattice parameter as well. As a material with a larger $a_{0,layer}$ than the substrate $a_{0,subs}$, the former assumes the value of the latter, becoming $a_{||} = a_{0,subs}$. The result is that $a_{\perp} > a_{0,layer} > a_{||}$ in this case, following the elastic theory of solid body mechanics and taking into account the stiffness coefficients of materials. The equation describing this relationship can be seen in equation 2.22 where n is Poisson's ratio, described by 2.23 [49]. This results in the third equation shown 2.24, where the stiffness coefficients are now seen, represented by C_{ij}.

$$a_{\perp} = (a_0 - a_{||})\left(1 + \frac{2\nu}{1-\nu}\right) + a_{||} \qquad 2.22$$

$$\nu = \frac{C_{12}}{C_{11} + C_{12}} \qquad 2.23$$

$$a_{\perp} = (a_0 - a_{||})\left(1 + \frac{2C_{12}}{C_{11}}\right) + a_{||}. \qquad 2.24$$

For quantum wells, this calculation is specifically important for strain balancing, a technique which uses layers of material with lattice parameters which alternate values higher and lower than the substrate value. This is outlined further in section 3.2. For quantum dot arrays, tetragonal distortion subsists, but an additional mechanism becomes prevalent at higher lattice-mismatch values.

2.4.2. Stranski Krastinow Growth Mode

For use in quantum confined devices, quantum dots must have the following characteristics: (a) the material must have a lower bandgap than the host, and (b) the material must have a larger lattice constant than the host. The first consideration affects the confinement and therefore the design of the absorption band (always red-shifted from the host). The second requirement results from the lattice mismatch necessary for the

special growth conditions that lead to QD formation. The first to observe this growth condition were Ivan Stranski and Lyubomir Krastinow in 1937 [50] who gave it their namesake.

Epitaxial growth modes for lattice-mismatched layers are typically categorized in three groups. Purely layer by layer growth often occurs at low lattice mismatch values (approximately 2% or less), and is called Frank van der Merwe mode. Vollmer-Weber (VW) mode refers to a relatively high strain energy differential (due to high lattice-mismatch) resulting in large, defective island formation. This is the most undesirable growth mode for optoelectronic devices, as its energy minimization is a result of the formation of lattice dislocations. If a material has a lattice mismatch of approximately between 2% and 10% [51], it is energetically favorable for small, coherently strained, defect-free islands to form instead of a continuous layer. This is known as the SK growth mode, and is an alternative to defect-generating relaxation occurring in the VW mode. These three modes are depicted in Figure 2.11 with their associated lattice-mismatch ranges.

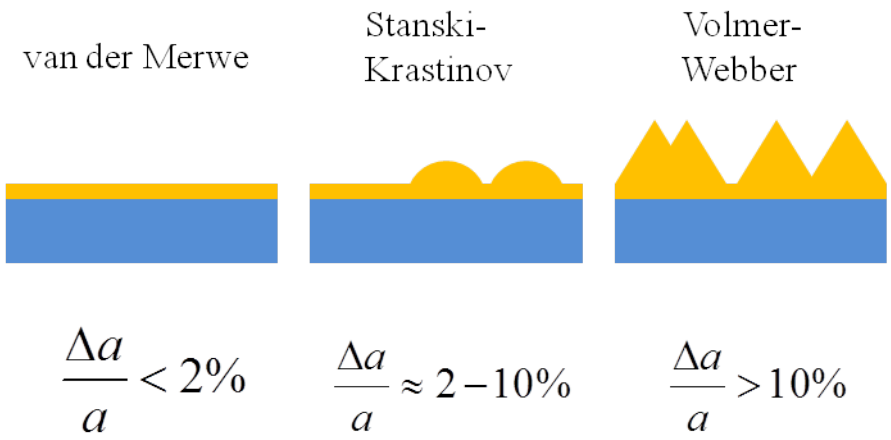

Figure 2.11. Visualization of the different growth modes based on lattice match and surface energy parameters.

These ranges are typically more approximations since the physical mechanisms take into account the strain-related surface energy (γ) relationships. The following equation relates the layer surface energy, γ_2, the substrate surface energy, γ_1 and the interface energy, γ_{12}. Two dimensional layer formation (Frank van der Merwe mode) occurs when the substrate

$$\gamma_2 + \gamma_{12} < \gamma_1 \qquad \text{van der Merwe} \qquad 2.25$$

$$\gamma_2 + \gamma_{12} > \gamma_1 \qquad \text{SK \& VW} \qquad 2.26$$

layer energy is greater than the sum of the interface and layer surface energies (equation 2.25). VW mode occurs when this sum is the larger quantity, but is typical of layers with higher interface energy, in which the substrate surface energy does not play as large a role. The layer surface energy, γ_2, increases with layer thickness, θ. SK mode occurs when equation 2.25 is satisfied during initial deposition, but gradually approaches and finally surpasses the inequality represented by equation 2.26. This is typical of layers exhibiting slight lattice-mismatches, but high thickness-dependent layer surface energies [17].

The two dimensional transition occurs when the left and right side of equation 2.25 or 2.26 are equal, and SK growth mode continues. This transition correlates with the system's critical thickness, θ_c. This value for the InAs/GaAs system is typically near 1.5 ML [17]. Beyond this thickness, quantum dots begin to nucleate. The density becomes then becomes highly dependent on further increased layer thickness illustrated in Figure 2.12. Shown in this figure are the effects of coverage value on QD nucleation and density with the critical thickness of 2D to 3D transition identified. QDs are typically spherical

hemi-ellipsoidal in nature, with an aspect ratio of 1:5 height to width. This can be seen in the Leonard equation plotted in Figure 2.12.

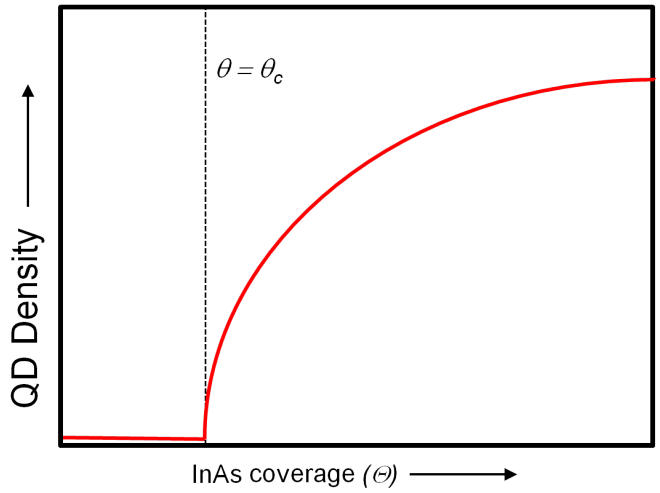

Figure 2.12. A plot of the Leonard equation with an indication of the onset of QD nucleation.

During and after the island formation, a 2D 'wetting layer' remains. This wetting layer (WL) remains coherent and lattice matched to the host material (here, GaAs), while the QD begins to relax to its natural lattice constant through the vertical axis of the QD. Therefore, in a higher bandgap matrix, the WL exhibits quantum well-like behavior, while the QD is truly confined in 3 dimensions.

2.4.3. QD Nucleation and Ostwald Ripening

The physical location of QD formation (or nucleation site) also is in large part due to surface energy effects. Thus far, we have discussed growth on the (100) planes of GaAs substrates. However this is not quite accurate. In vicinal substrates, atomic steps are a standard feature in the surface morphology. The ridge of these steps provides a discontinuity in the GaAs lattice. The termination of these lattice points provides a low energy as there is a relaxed constraint of coherence site conducive for InAs bonding [52].

This is evident in two cases. Preferential alignment of QD formation along terrace step edges has been observed [53]. This can be observed in Figure 2.13. Secondly is the degree of which miscut plays a role in the nucleation of these sites. As the terrace step edges created by this vicinal nature are increased, with increasing miscut angle, the QD density increases [53].

A secondary growth mechanism can occur subsequent to coherent island formation. Ostwald ripening, or the maturation of large, coalesced QDs begin to form at higher coverage values. This process becomes energetically favorable when the surface of the coherent QDs provides a new energy minimization site for other existing QDs. At growth temperatures, the In and As adatoms are mobile enough to allow for surface translation. The coalesced QDs are much larger (up to 25/100 nm in height/diameter) [54]. The interfacial nature of multiple QD coalescence provides a phase difference in morphology in which lattice dislocations can occur. This formation is detrimental to optoelectronic device operation due to high non-radiative recombination occurrences that may be present at these dislocations, and avoidance of this growth regime is desirable. This topic is addressed extensively in chapter 4.

2.4.4. Experimental QD Test Structures

Test structures were grown with QDs uncapped, and atomic force microscopy (AFM) was used to reveal size, density and shape of the QDs. Figure 2.13 shows an example of an AFM image of these nanostructures on the surface of GaAs. From these images, we obtain QD sizes of between 25-45 nm diameter and 5-10 nm height values. Shape is generally hemi-spherical and QD density was found to be 5×10^{10} cm^2. It should

be noted that since the QDs used for AFM images are "uncapped" or do not have any material grown subsequently, that they may not be representative of the QDs buried under layers. It is known that In and Ga atoms can diffuse during subsequent high temperatures steps and the outer edges of the QD can become Ga rich, and the surrounding GaAs layer can become In rich [55]. This may change shape and size characteristics, but not QD density. The growth of superlattices is left for the much more detailed discussion on strain in chapter 0.

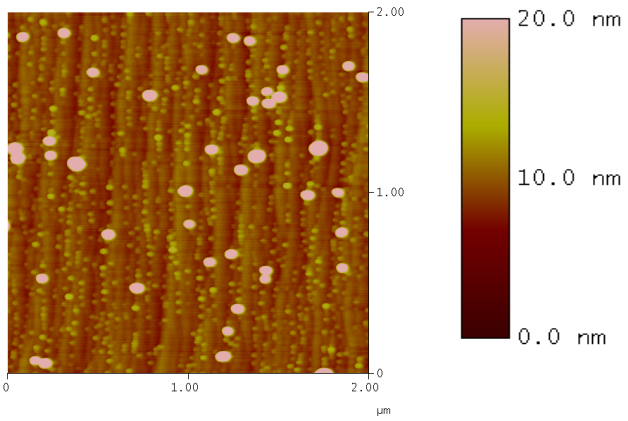

Figure 2.13. A 2 x 2 µm atomic force microscopy image of 2.17 ML of InAs QDs grown on GaAs substrate.

2.4.5. QD superlattices

In order to fully utilize the effects of the inclusion of these nanostructures in optoelectronic devices, it is desirable to maximize the exploitation of the quantum effects. To address this, a simple way to compound the absorption volume and to ultimately increase the short circuit current, is to increase the number of layers included in the *i*-region of the device. In addition, the requirement of the overlap of the wavefunctions is necessary for the IBSC device operation (discussed in chapter 5). This functionality can

be obtained only by including multiple wells or dots separated by an energetic barrier. It is for this reason that stacking the arrays of quantum dots is of critical importance. Strain balancing in these systems becomes essential to the material quality as well, but will be left for chapter 0. More importantly here, is the consideration of absorption depth as the layer numbers increase.

The absorption coefficient (α) can be defined with the simple form of the Beer-Lambert law (equation 2.21) can be used to determine the loss of intensity through a medium, or the absorptivity (I/I_0) [56]. This can be implemented using the absorption coefficient of a quantum dot or well. Therefore absorptivity increases with amount of material. In multiple quantum structures, layers are inherently thin and therefore increasing the number of layers is the primary method of increasing the absorption volume. Similar to emission-based devices, an increase in volume of the confined or tuned absorbing media improves sensitivity in the case of a detector, [57, 58]. Similarly, in photovoltaic devices, whether pursuing an IBSC or a bandgap tuning approach, an increase in the absorbing media, as will be discussed, improves short circuit current density and ultimately device performance.

2.5. Conclusion

In this chapter the origin of photovoltaic action has been established. The current III-V technology is introduced and discussed. The current methods of splitting the solar spectrum using the variation in bandgaps are outlined and an alternative was introduced using nanostructured photovoltaics. The operation of a solar cell and the physics of these devices were outlined. The regions of a solar cell were evaluated and their contributions to device operation explained.

The InAs/GaAs QD system was identified for its use in these devices with benefits including high-profile literature exposure and broad knowledge base, and the compatibility with existing GaAs technology. Device fabrication steps were outlined and the importance of the specifics used here was justified. Device testing was introduced and will be valuable for the understanding of subsequent chapters. Device design was explained in the light of the inclusion of nanostructures in the intrinsic region. Epitaxial MOCVD growth of both semiconductor layers and QDs was described in detail and the mechanisms of SK growth were clarified. Application of these in superlattices was introduced and the need for this structure was explained with a focus on increasing the number of layers included.

3. Strain Balancing QD Superlattices

3.1. Introduction

It is well known that heterostructure materials with mismatched lattice constants will grow 'pseudomorphically' until a relatively predictable thickness. This thickness, known as the 'critical thickness' was first evaluated by Matthews and Blakeslee [59]. Their analysis began with a force balance between the force exerted by the misfit strain (involving the Poisson's ratio, the shear modulus and the angle between multilayer interface and slip plane), and the force resulting from the tension line of the dislocation [59]. This force balance may exhibit an inequality, in which either dislocations form or lattice coherence is observed. This development lead to the first derivation of the following transcendental equation for the determination of the critical thickness, h_c, of a strained layer grown on a theoretically infinitely thick substrate [60]:

$$h_c = \frac{a}{\kappa\sqrt{2}\pi f}\frac{1-0.25\nu}{1+\nu}\left(\ln\frac{h_c\sqrt{2}}{a}+1\right) \qquad 3.1$$

where a is the lattice constant of the strained layer, κ is the structural coefficient, ν is Poisson's ratio, and f is the mismatch factor defined by $\Delta a/a$. The structural coefficient is simply an integer (1, 2 or 4) based on whether the structure is a superlattice, single QW, or single strained layer, respectively. It is clear from this equation that at higher mismatch factors, h_c is reduced. Using this method, critical thickness for pure InAs on GaAs is $h_c <$ 1 nm, for GaP it is $h_c \approx 10$ nm. Although a superlattice is used here, the factor of $\kappa = 1$ for this structure is not quite accurate since this is a strain balanced superlattice. As we will discuss further in the following sections, a method of stain-balancing is used to grow

layers much thicker than the resulting critical thickness without this technique, since the overall system mismatch factor decreases. In QW systems, correct stain balancing can theoretically provide the ability to grow superlattices infinitely thick, since overall mismatch results in a net factor of zero. Because of the three-dimensional nature of the strain field, this is thought not to be possible with QD array-based superlattices.

In order to understand why stain balancing is necessary, it is important to first understand the conditions that are present when strain balancing is not used. Initial quantum dot solar cells grown without strain balancing, it was apparent that there was significant degradation in cell material. TEM imaging of a test structures indicated undesirable material qualities, showing inhomogeneous QD geometry, and threading dislocations, leading to reduced lifetimes in both the intrinsic and emitter regions. Shown in Figure 3.1 (left), is a 5 layer QD superlattice which has not been strain balanced. The original QD size is not maintained in the growth direction. As each additional layer is grown, the GaAs capping layer is stretched to the relaxed InAs lattice constant and slowly relaxes back to its lattice constant before the next QD is grown. If the GaAs does not fully relax, then the next layer of QDs will not be as mismatched as the first QD, resulting in a wider, more pancake like structure. With each additional layer, this trend continues approaching a more QW-like superlattice. This effect can be seen with different materials systems, since if the lattice mismatch factor is larger, the interfacial strain energy (γ_{12}) will be higher, which causes greater self-accumulation of InAs, directly affecting aspect ratio [61].

Point defects originating in the superlattice material, or *i*-region in a device, can propagate as threading dislocations, in the material grown subsequently, in this case, the

solar cell emitter, see Figure 3.1 (middle). These defects cause unwanted recombination in both the space charge (SCR) and the quasi-neutral regions of the device. These problems become very obvious when looking at the illuminated forward *J-V* characteristics (Figure 3.1, right). Recombination in the high defect density emitter can reduce the amount of carriers that will complete the path to the metalized contacts. This manifests itself in the reduced current shown in Figure 3.1 (right) for the 5 layer QD p-i-n device when compared to the baseline with no QDs. Recombination in the SCR, places device operation in the ideality of n = 2 region of a traditional diode curve. This domination of the SCR term in equation 2.13 is due to the lifetime reduction shown in the denominator of equation 2.9, significantly increasing the device reverse saturation current, J_0. As per equation 2.14, we see how this increase can degrade the open circuit voltage of the device, and is also apparent in Figure 3.1 (right) by the loss of about 500mV with the addition of QD layers (red curve). This corresponds to an increase of eight orders of magnitude in the J_0 value resulting from a shift in the domination in terms of equation 2.13.

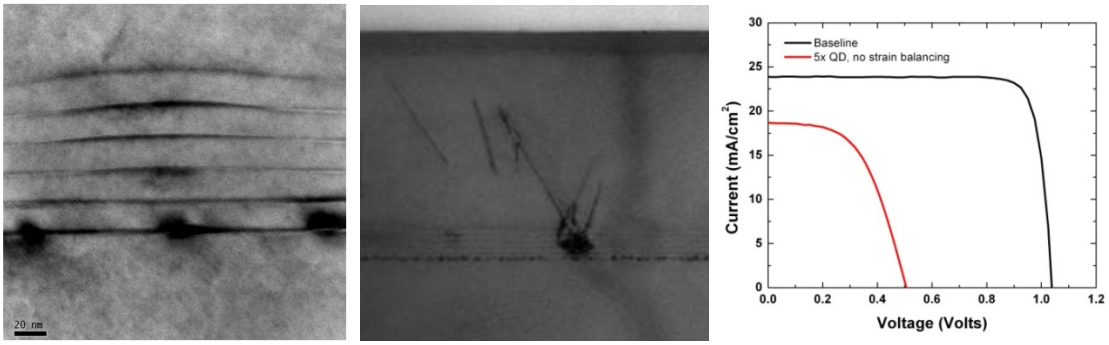

Figure 3.1. Left: TEM image of 5 layers of QDs with no strain balancing describing size non-uniformity in the growth direction. Middle: TEM image of propagating defects into the emitter region above QD-embedded *i*-region. Right: J-V characteristics of baseline and unstrain-balanced QD-embedded solar cells.

The defects in shown in Figure 3.1 are typical in lattice mismatched material. The strain associated with this lattice mismatch is principally undesirable for optoelectronic device operation. However, if the strain can be controlled and minimized, it is possible to use lattice mismatched material in devices. Examples of this include strained multiple quantum well lasers [62], step-graded buffer pseudo substrates [63], as well as high efficiency solar cells,

3.2. Strain balancing in QW solar cells

Balancing the strain in these complex structures can be simple in the case of a quantum well. Since deposition with near-atomic precision can be achieved, balancing this strain is necessary. Well known theories of strain balancing have been thoroughly studied, and quick calculations can be used to determine, given both the strained layer layers [64].

Following a specific formula (Ekins-Daukes compares 3 different formulas [64]), for quantum wells, it is simple to determine the thickness of the GaP layer that will correctly compensate for strain in the originally strained layer. The simplest of these, namely the average lattice method (ALM) [64], was used originally to compare our samples with and those without strain compensation. In this method, the thickness/lattice constant product is used to determine the appropriate strain balanced condition. If t_{sl} is the thickness of the originally strained layer, and t_b is the to-be-determined strain balancing layer, then,

$$t_b = t_{sl}\left(\frac{a_{sl} - a_0}{a_0 - a_b}\right) \qquad 3.2$$

The thickness weighted method includes the thickness as a weighting, assuming that a thickness-lattice constant product is more influential to strain balancing than purely the lattice constant alone and is described by:

$$t_b = t_{sl}\frac{a_b}{a_{sl}}\left(\frac{a_{sl}-a_0}{a_0-a_b}\right) \tag{3.3}$$

And finally, the zero stress method includes the stiffness coefficients of each material. The values of these are different enough between semiconductors such that the inclusion of them into the strain balancing calculation is necessary, and is shown in equation 3.4:

$$t_b = t_{sl}\frac{a_b^2}{a_{sl}^2}\left(\frac{a_{sl}A_{sl}-a_0A_{sl}}{a_0A_b-a_bA_b}\right) \tag{3.4}$$

where:

$$A_i = \left(C_{11}+C_{12}-\frac{2C_{12}^2}{C_{11}}\right)_i \tag{3.5}$$

where a_{sl} and a_b are the lattice constant values of the strained layer and the balancing layer, respectively.

3.3. Strain Balancing in QDs

For quantum dot material, there is less of a layer and more of a non-continuous array of islands. Therefore, this strain balancing can be more complex, as the strain fields are now in three dimensions, instead of nominally one. The material choices for strain balancing are limited to those with lattice constants less than that of the host material, in this case GaAs (a_0 = 5.6533Å). Referring again to the crystal grower's chart (Figure 2.2), we see III-V materials that can be utilized for this purpose as having a higher bandgap

than the InAs QD structures as well as the GaAs host and spacer layers. The materials available from the OMVPE reactor at NASA GRC, including trimethylgallium (TMGa), trimethylindium (TMIn), trimethylaluminum (TMAl) (as group III precursors) and arsine (AsH_3) and phosphine (PH_3) (for group V precursors) were used for alkyl and hydride sources, can be used for growing most binary and ternary compounds.

Although ternary materials can be and often are used for device design and managing strain, binary compounds are used when possible, due to their ease of growth. The single binary III-V compound with a shorter inter-atomic distance than GaAs is GaP. This material is also convenient for the purpose of keeping the layer thin, aiding in both carrier transport and miniband formation, which requires a high degree of proximity for the confined states. The lattice constant of GaP is a_{GaP} = 5.45Å resulting in a lattice mismatch with GaAs of ~3.6%. When GaP is grown directly on a layer of GaAs, its lattice constant is stretched in the parallel-to-wafer-surface direction, hitherto referred to as the parallel direction. Biaxial stress in a single unit cell of GaP grown on GaAs causes the lattice constant in the perpendicular-to-wafer-surface direction to decrease, as described by the material property Poisson's ratio, ν (typically in the range of 0.3-0.35 for semiconductors). This general mechanism is outlined extensively in section 2.4.1 and can be visualized in Figure 2.10.

3.3.1. Test structures

Using the basic balancing equation (3.2), early test structure and solar cell samples were grown with varying strain compensation thicknesses near the optimal thickness (14Å) for 2.15 ML of InAs. Test structures with these varying thicknesses were

used to perform high resolution x-ray diffractometry (HRXRD) in order to determine the amount of residual out-of-plane strain present.

High Resolution XRD is an extremely sensitive tool used to determine structural aspects of single-crystal materials. In these materials, slight changes in lattice constant due to strain can give specific intensity signatures with respect to diffraction angles (θ and 2θ) which are often not reliably detectable with standard XRD techniques. This is specifically of interest when working with lattice mismatched materials, as the residual strain can determine the material quality of subsequently grown epitaxial layers. Small slit sizes are coupled with high x-ray intensities to provide extremely detailed XRD signatures for materials capable of quantitative characterization of material strain (shift in lattice constant in space) and other helpful information like layer thickness and interface quality.

Classical XRD theory begins with the Laue condition that, when satisfied, particular angles produce intensely diffracted x-ray reemission. This was simplified by Bragg with his equation describing the angle at which these re-emitted x-rays constructively interfere. The Bragg equation (equation 3.6) states that for n planes of a particular material with a plane spacing of d, a diffraction angle exists, θ, at which an intense peak in intensity can be detected, and at theoretically all other angles, no x-rays will be detected.

$$n\lambda = 2d \sin\theta \qquad 3.6$$

Implicit differentiation along with the replacement of the plane spacing with the lattice constant, a, allows the evaluation of the strain, $\Delta a/a$ as a function of the Bragg angle, and the separation of the Bragg angle and "layer" peak associated with the lattice

constant of the strained layer (equation 3.7). In the case of a superlattice grown epitaxially on a pre-existing semiconductor surface, the average out-of-plane lattice constant of the entire superlattice is interchangeable with the lattice constant of a single layer. In equation 3.7, this can be also quantified as the lattice mismatch between the layers.

To evaluate the effects of designed lattice mismatch, three samples were grown with no GaP, 14Å (5.1ML), 18Å (6.6ML) in order to investigate no strain balancing, calculated value of correct balancing, and a sufficiently over strain-balanced condition. Figure 3.2 shows the [004] HRXRD scans of these three samples. The [004] plane allows for a symmetric HRXRD scan, providing out-of-plane lattice constants for the three samples in a single scan. The peaks centered at zero arc-seconds (denoted as the Bragg peak) indicate the high intensity of diffracted rays

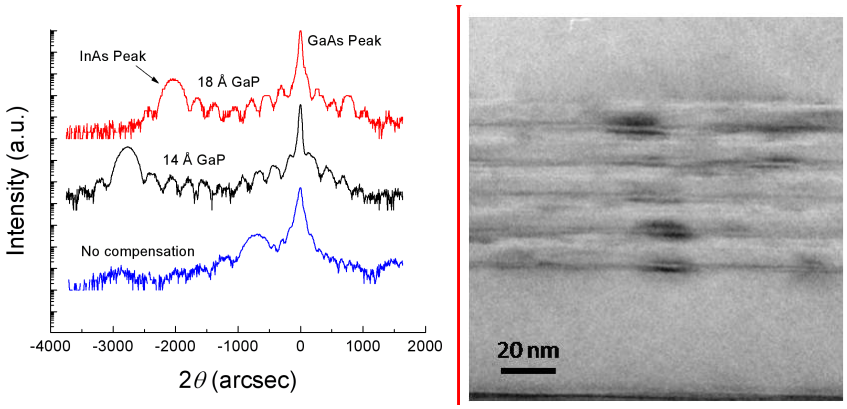

Figure 3.2. Left: HRXRD scans of three QD superlattice samples with varying the strain balancing condition. Right: Cross-sectional TEM image of strain balanced 5x QD test sample.

from the substrate (GaAs), where the peaks to the left (labeled InAs) indicate the superlattice (-1) peak and the superlattice (0) peak, (SL(0)) shows up to the right of the Bragg peak. The difference between the SL(0) peak and the Bragg peak is an indication

of the amount of out-of-plane strain that remains in the sample. The fractional lattice mismatch can be determined by,

$$\frac{\Delta a}{a} = \Delta\theta_{sl} \tan\theta_b \qquad 3.7$$

where θ_b is the measured Bragg angle, and $\Delta\theta_{sl}$ is the difference in radians between the Bragg peak and SL(0).

As seen in Figure 3.2 (left), the sample with 14Å of GaP shows a SL(0) buried in the Bragg peak indicating very little out-of-plane strain (400ppm), while the 18Å GaP sample was calculated to have about 5000ppm. Figure 3.2 (right) shows a TEM image of a strain balanced stack of 5 layers of QD structures. Here, it is shown that the QD structures align vertically and are uniform in size from layer to layer (comparing to Figure 3.1, left). Clearly, the addition of GaP is instrumental in balancing the strain in the sample which is essential to minimizing defects (avoiding devices like that shown in Figure 3.1, right).

As stated in chapter 0, maximizing the absorbing volume of nanostructures is of much interest to general quantum optoelectronic devices. 400ppm in a five layer structure is sufficiently low for optoelectronic device performance [64]. However, increasing the number of layers of these structures brings the potential for a higher accuracy of strain balancing. To further illuminate the optimal balancing point, simulated HRXRD was performed using the LEPTOS DIFFRAC^{plus} software (provided by the Bruker Discovery D8 tool package). This simulation uses a genetic algorithm method to fully solve the Laue equations for the exiting x-ray spectrum. The actual experimental conditions of x-ray diffraction are used along with given layer thicknesses and material (included is a library of material properties such as x-ray susceptibility, lattice constant etc.). Keeping

all other layers constant, and assuming an InAs layer thickness (QW) of 2nm, the GaP thickness was varied from 0.1nm to 1.5nm in steps of 0.2nm. Figure 3.3 illustrates the results from this simulation. The peak labeled SL(0) is the 0^{th} order superlattice peak and its offset indicates magnitude and sign of strain in the layers. For the 1.5nm through the 0.9nm curves, the SL(0) peak lies to the right of the Bragg peak, indicating a respectively decreasing magnitude of tensile strain (+). From 0.1nm to 0.5nm, the SL(0) peak lies to the left of the Bragg peak, indicating a respectively decreasing magnitude of compressive strain (-). At 0.7nm of GaP, the peak is buried under the Bragg (GaAs) peak indicating it is the layer stack closest to being strain balanced.

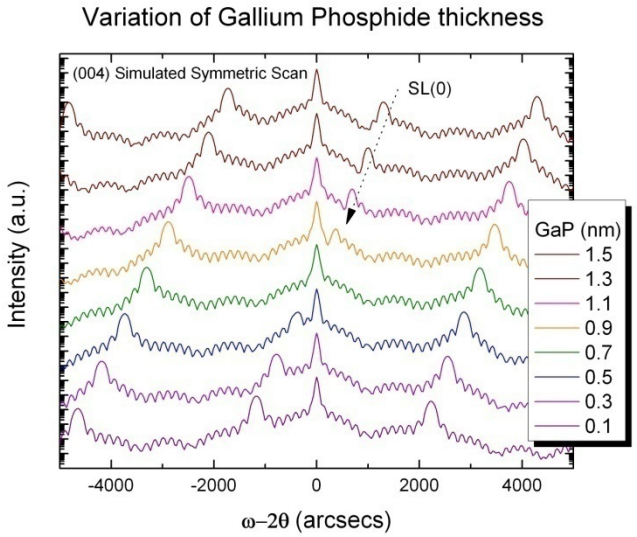

Figure 3.3. Results of HRXRD simulation of 10-layer test structure illustrating the effects of varying the thickness of the GaP strain balancing layer.

Extracting the out-of-plane strain value using equation 3.7 from both experimental and simulated data and plotting these together (Figure 3.4), the trends become obvious. First, as expected, there is a positive slope in both sets of data, as thinner GaP thicknesses

will inherently result in a more compressive superlattice. GaP is strained to a lattice constant larger than natural, so with a thicker layer, a larger volume of the superlattice is comprised of GaP material, resulting in a more tensile layer stack. Second, there is a shift in the "0" intercept, or the strain-neutral condition between the data and the simulation. This shift is non-negligible and is due largely to the fact the simulation assumed no relaxation (coherently strained condition. This no relaxation condition is not the case with most materials, and therefore more GaP (in this case) is needed to make up for loss due to relaxation. Also, the simulation is of quantum wells, not three dimensional structures which were estimated to be only 1nm continuous layer for the simulation. The 2D-3D assumption can give drastically under-estimated thicknesses of required GaP since the QDs (~5-6nm) are roughly an order of magnitude thicker than the 2D wetting layer. This second point motivates the need to a more comprehensive solution to the strain balanced condition when considering 3D islands such as QDs, and provides the ground work for modifications discussed in section 3.3.2.

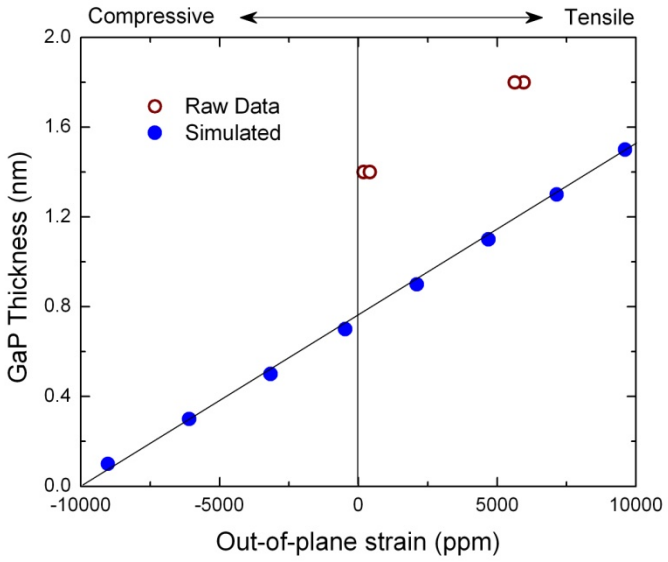

Figure 3.4**.** Plot showing the amount of out-of-plane strain in both experimental and simulated samples as a function of GaP layer thickness. The line is provided as a guide for the eye.

With preliminary conclusive evidence of the efficacy of strain balancing, it was clear that solar cell testing could provide further device-related information for samples without and with strain balancing layer thickness, as well as the variation of this thickness. A series of 5x QD solar cells were grown along with a baseline GaAs *p-i-n* solar cell. Of the 3 solar cells with QDs, one had no strain compensation, one with 14Å and one with 18Å of GaP inserted between each layer of QDs as the SB layer. Figure 3.5 (left) indicates the results of this series of devices. The black curve indicates the baseline GaAs sample giving typical values of about 23.5mA/cm^2, 1.042V, and an efficiency of 15%. The cell with 5 layers of quantum dots and no strain compensation has severe losses in both current density and voltage when compared to the baseline.

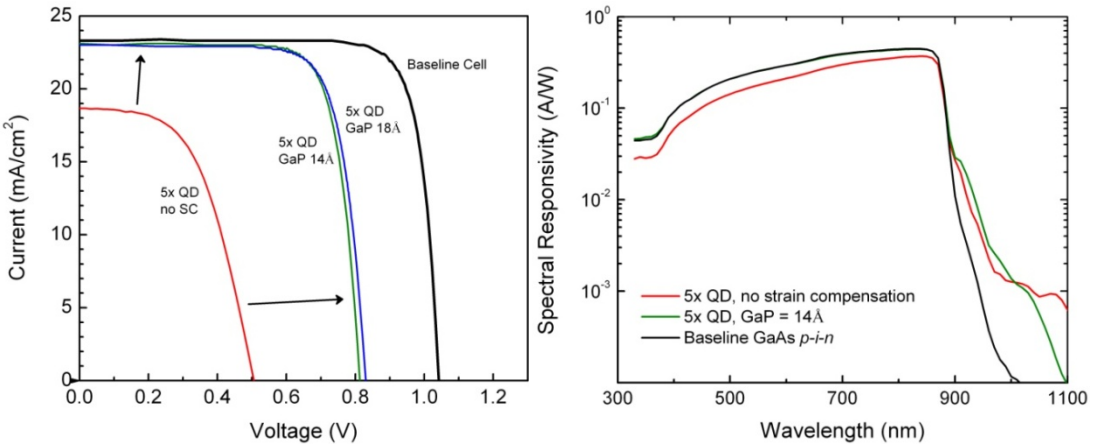

Figure 3.5**.** Left: IV curves of solar cells grown with and without quantum dots including a comparison of strain compensation layer thicknesses. Right: Log scale external quantum efficiency of the same samples giving spectral resolution to current losses.

Minority carrier devices such as solar cells are inherently very sensitive to minority carrier diffusion length which increases as a function of dislocation density.

Therefore, devices with a high defect density, will cause a high number of carriers that recombine before they cross the junction and will not contribute to the current. In this case, material grown after the QD region cab be a source of these defects. Emitter degradation can be as a spectral responsivity loss in the entire visible region (above GaAs-bandgap) as in Figure 3.5 (right). The open-circuit voltage is also affected with a value at about 0.5V or half the expected GaAs voltage. Although this can attributed to a logarithmic loss in short-circuit current, the most likely cause of the voltage drop in all of these samples (referencing the baseline), is a significant increase in the dark current density as described by equation 2.14. Although dark current measurements were not taken for these cells, high dark saturation currents (J_0) typically stem from a poor (high) non-radiative recombination caused by the high defect density associated with no strain balancing. Here, a fill factor loss is observed indicating internal series resistance originating from the decreased mobility of the emitter layer due to defects. Defects due to the QD layers have had a negative effect on each solar cell parameter, when compared to the baseline. Upon the insertion of GaP strain compensation layers, improvement in each parameter is observed. The short-circuit current is virtually restored to the baseline value indicating severe recombination has been avoided. Some voltage reduction is still observed, which can be attributed to the remaining unavoidable defects in the intrinsic region due to the inhomogeneous strain present. The fill factor improves to almost that of the baseline indicating a higher quality emitter material. It is clear that not only do the SB layers improve material quality, but including them in QD solar cells drastically improves devices performance.

Careful investigation into the atomistic mechanisms of the superlattice can reveal further details regarding the perfectly strained condition. Equation 3.2 is a very basic, lattice constant/thickness average that can be rearranged from the Matthews and Blakeslee formulation [59]. Two further formulations have been proposed to Ekins-Daukes in his paper on the strain balancing of QW solar cell [64]. As previously discussed, the thickness-weighted method (equation 3.3) weights the product of the lattice constant and the thickness for the determination of the balanced condition. The second alternate method is known as the zero stress method (ZSM) [64], which applies the continuum elasticity theory (CET) of mechanics [65] and is shown in equation 3.4. In this theory, the stiffness coefficients as well as lattice constants and thicknesses are inputs and the in-plane stress is minimized in order to ensure that no shearing occurs at any lattice plane.

Plotting these three relationships illustrates the differences in their determination of the condition with zero strain in the out of plane direction. Figure 3.6 shows these relationships plotted with the HRXRD-determined strain values as a function of GaP layer thickness. There is a relatively small difference between the determined optimal thickness using the average lattice and the thickness weighted methods. The zero stress method, however, shows quite a reduction in the thickness required from the strain compensation layer to obtain the minimally strained condition. In comparison, samples were grown with 3.5, 4.5, 6.4 and 7.5 ML of GaP, and the HRXRD data follows quite well with the first two theories. This is contrary to the anticipated result since the zero stress method is accepted as the most accurate theory as it takes into account the elastic coefficients of the materials and the other two do not. The only explanation was that the

data was coming from a 3-D, discontinuous medium (quantum dots) and the theories represent the balancing of two dimensional layers.

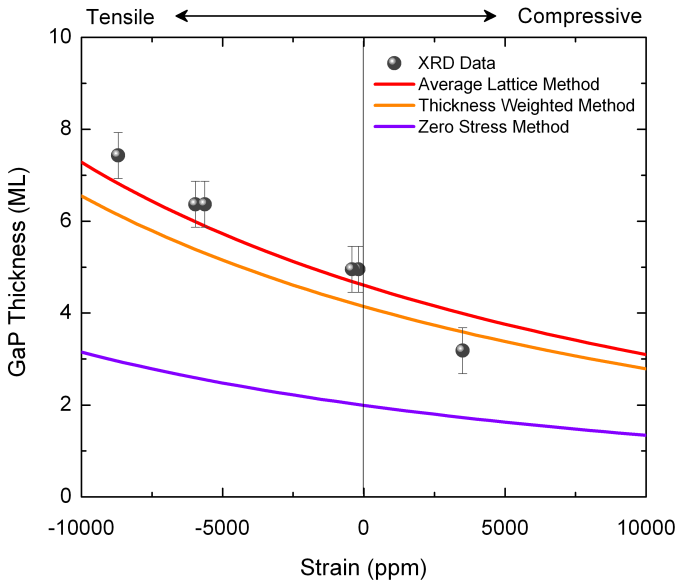

Figure 3.6. Three strain balancing methods plotted along with the data from high-resolution x-ray diffraction.

Looking at a cross section of the layer structure as the simplified cartoon shown in Figure 3.7, we can see the strain (represented by the lattice constant ratio here), is very sensitive to the layer thicknesses. In the middle diagram, the blue line represents the relative value of this ratio. When InAs is placed on top of the GaAs, the GaAs stretches in the horizontal direction, so the ratio gets higher than 1. Initially, what is known as the wetting layer is considered, "coherently strained," and maintains the GaAs lattice constant. Above this point, as the QD grows, its lattice constant increases until it is fully relaxed at the top of the QD, represented by the top of the yellow layer. The GaAs grown above the InAs at this point begins coherently strained to the InAs, but relaxes slightly back towards its natural lattice constant, reducing the ratio. GaP has a lower lattice constant that GaAs, so it naturally moves the ratio back towards 1, and a final GaAs

theoretically relaxes back to its own lattice constant. This is ideally how using GaP for strain balancing should work. One can see by looking at the left (under balanced) or the right (over balanced), how too little or too much GaP can immediately alter the strain energy in the stack. Since these diagrams only represent a single repeat unit of a much higher order superlattice, a layer of InAs will inevitably be grown on top of the last layer of GaAs. In the left or the right case, the behavior of this secondary InAs layer will behave differently than the first (shown). And the difference will propagate up through the superlattice. If this difference is small, the effects may not compound significantly enough in only 5 layers, but may still be present and could not show up until 10 or more layers are grown. It is this added constraint that indicates the criticality of getting this layer thickness correct.

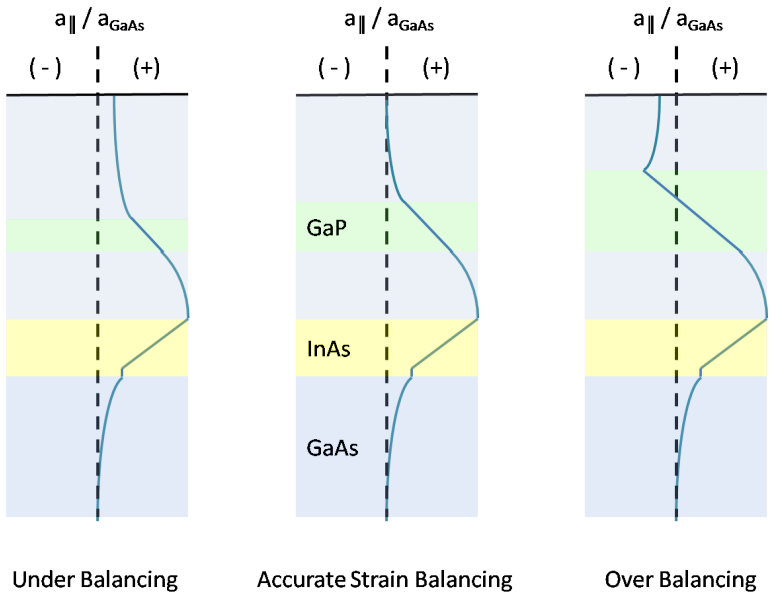

Figure 3.7**.** The effects of balancing layer thickness on the overall strain throughout a single repeat unit of the QD superlattice structure used in these devices.

Combining the critical nature of the layer thickness sensitivity with the 3D nature of the QD layers, clearly a more accurate method is needed for the design of QD superlattices. As shown with the material characterization, as well as electrical device characterization, structural and optical degradation of QD-embedded devices can be problematic. Fundamentally, an optimal strain balancing layer would be one in which there were different thicknesses above each individual quantum dot as opposed to above areas with no QDs. This, of course would require the growth of QDs with the balancing material, which is impossible due its lattice constant ratio to GaAs being less than 1.

3.3.2. Three Dimensional Modification

Proposed here is a new method making use of both the most accurate zero stress method, but also taking into account the three dimensional nature of the QD layer. This method uses the thickness calculated from the ZSM above a QD and also the thickness calculated from the ZSM above the wetting layer only. These two values are then weighted by the QD density. This is illustrated for visual aid in Figure 3.8.

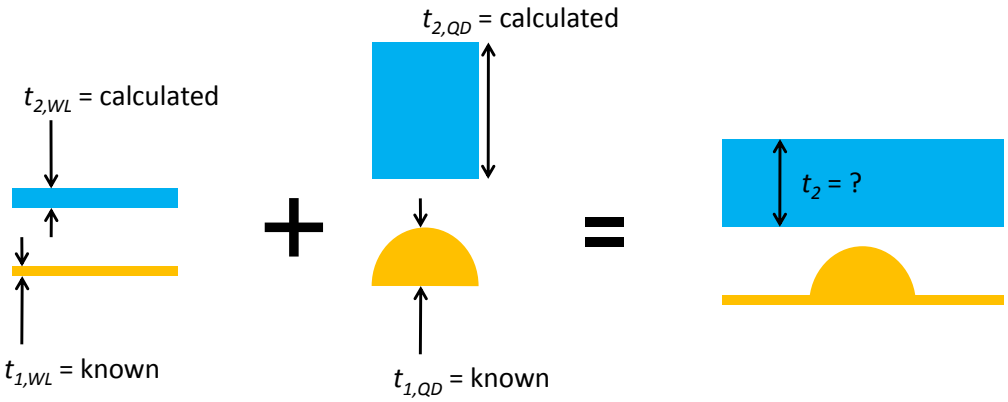

Figure 3.8. Illustration of the modified zero stress method for strain compensation of quantum dot arrays.

Here, the yellow material denotes material that requires balancing, and the blue material indicates the GaP (or other material) that is used for balancing. Since first two thicknesses $t_{2,WL}$ and $t_{2,QD}$ can be calculated, a 3D t_2 can be then estimated by weighting the effects of the wetting layer and the QDs by their respective areal densities. The equation describing this weighting is shown here:

$$t_2 = \rho\sigma t_{1,QD} + \left(1 - \rho\sigma t_{1,WL}\right) \qquad 3.8$$

In this relationship, ρ is the two dimensional density of QDs and σ is the areal footprint of a single QD. Thickness subscripts denote the known (estimated) QD/WL thickness (1) and the GaP thickness (2). The value t_2 was determined for this system to be a GaP thickness of 3.9ML. A series of 10x QD test structures were then grown centered on this expected value by varying the GaP thickness (3.1ML – 5.0ML). These structures were

not solar cells and therefore were only tested for their mechanical properties (HRXRD) and their optical properties (photoluminescence).

Figure 3.9 (left) shows the results from the x-ray measurements. As before, the 0^{th} order superlattice peak does show up offset from the Bragg peak in most samples. But, as seen in the simulation (Figure 3.7), there is a point at which the 0^{th} order superlattice peak passes through the GaAs Bragg peak (adjusted to 0 arcseconds). This offset is used as before to calculate the out of plane strain, and then using a formulation of Poisson's ratio [64], the in-plane strain were determined. These five data points can be seen in Figure 3.9 (right) plotted with the three other theoretical relationships and the modified zero stress method described by Figure 3.8. The general trend of all of these theories show that with increasing thickness of GaP, the in-plane strain becomes increasingly negative, indicating a more tensile case. This stands to reason, as the GaP is naturally in tension on a GaAs substrate. Clearly, a value between 4.2 and 4.7ML for the thickness of this layer in this system would result in an in-plane strain-neutral condition. Although the thickness predicted by the modified method (green curve in Figure 3.9, right) of 3.9ML does not fall in this range, it does follow the experimental results much more closely than the unmodified zero stress method (purple curve).

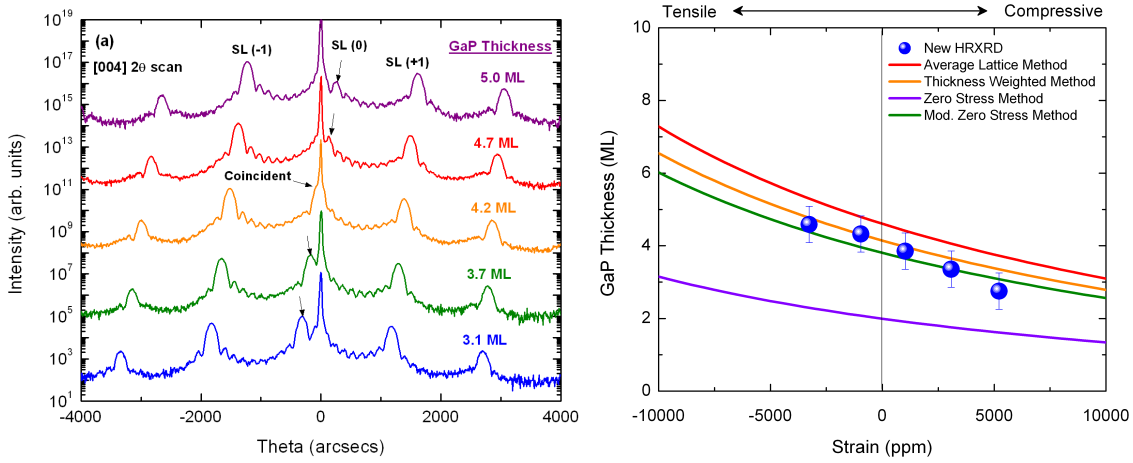

Figure 3.9**.** Left: HRXRD $\omega/2\theta$ scans revealing the out of plane strain in the superlattice of the samples. Right: the extracted in-plane strain plotted with various strain balancing theories [66].

In order to investigate the effects of proper (or improper) strain balancing on the optical quality of these arrays, the samples were then subject to experimental optical testing. Photoluminescence (PL) is a method in which the optical quality of a material can be evaluated. Typically, electron-hole pairs are separated due to incoming optical excitation, and their radiative recombination processes can be observed by detecting emitted photons. In the event that recombination occurs non-radiatively, the emitting spectrum is reduced, as radiative events are lost to non-radiative events. This measurement is highly sensitive to material quality since an increased defect density can be correlated to a reduction in radiative recombination directly observable by PL.

Here, the five samples were excited by a 514nm Argon Ion laser, with a beam flux of 0.477 W/m^2, and their spectra were recorded using an Ocean Optics NIR512 cooled InGaAs array spectroradiometer. Since QD size varies spatially on the wafer, PL measurements were taken on the same locations on all samples (± 2mm). The results of these measurements are shown in Figure 3.10 (left). The curves' peak values maximize at

the 4.2ML sample, with the 4.7ML sample very similar. More importantly, the integrated PL intensities (shown in Figure 3.10, right), clearly indicate that the sample with 4.2ML has the highest number of radiative recombination events. This correlates to the highest optical material quality of all of the five grown samples. Both mechanical and optical experimental outcomes have been shown to support the modified theory. It is therefore proposed that this theory is applicable to any material system being utilized for strain balanced QD arrays.

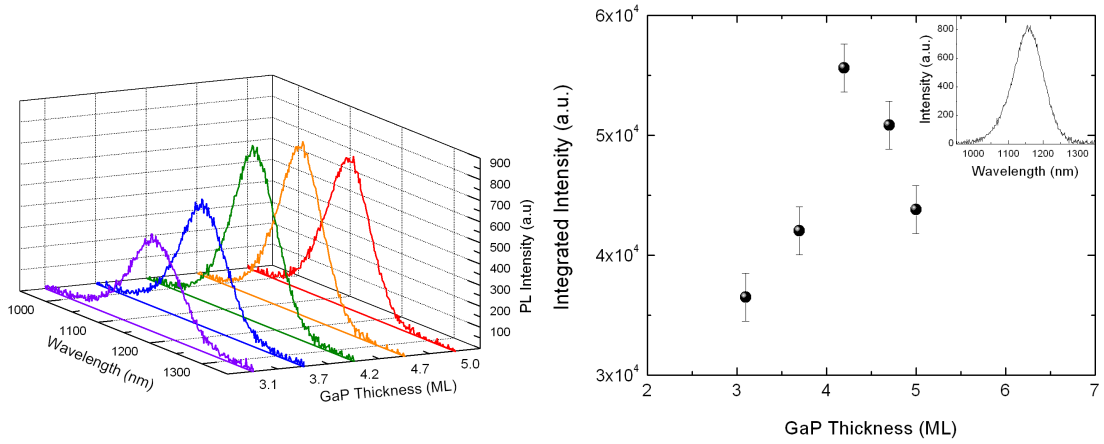

Figure 3.10. Left: Photoluminescence spectra for each of the five samples with varying GaP thickness. Right: shows the single integrated values for each of the five samples [66].

3.3.3. Other balancing materials

In this work, GaP was chosen as for the strain balancing layer first because of the tensile lattice constant it provides in reference to GaAs. Additionally, the availability of this compound with the given precursors and its simplicity of growth as a binary material made it the ideal candidate. Strain balancing of QD arrays for superlattices has been

achieved successfully using other materials such as GaNAs [67], GaAsP [68], as well as a unique double-GaP layer shown by Laghumavarapu [12]. Of these methods, GaAsP is the most promising alternative to GaP. The degree of growth complexity increases due to the ternary nature of this compound, with the addition that ternaries with composition trade off in the group V element can be especially difficult due to sensitivity of composition to both thermodynamic and kinetic growth processes [48]. However, because these layers are being grown between layers of GaAs, it may be advantages to use GaAsP for this purpose, as the AsH_3 precursor does not need to be removed and replaced during growth of these very thin layers. An additional benefit of using GaAsP is that the addition of the As element allows for a reduction in bandgap (GaP = 2.24 eV, $GaAs_{0.2}P_{0.8}$ = 2.1 eV), which, in the barrier material, may assist transport through the intrinsic region and remove some necessity to tunnel through pure GaP. Unfortunately, the reduced lattice constant associated with the inclusion of As in the alloy, requires a thicker layer for appropriate strain balancing. This can be detrimental to carriers that are required to tunnel, thought this effect is competitive in nature with the lowered barrier height. Since the lattice mismatch of GaP is 3.6%, this layer is kept on the order of single monolayers. A result of the need for thicker balancing layers with the addition of As is that more thickness control is available and uncertainty in the thickness can be minimized, and more accurate balancing may be obtained.

This complex set of advantages and disadvantages can be visualized in Figure 3.11. Here, a depiction of the energy band diagram (not to scale) is shown as a function of As content (0, 10 and 20%). Here we can see the reduction in barrier height impeding

electron transport and also the variation in thickness necessary to maintain strain balancing.

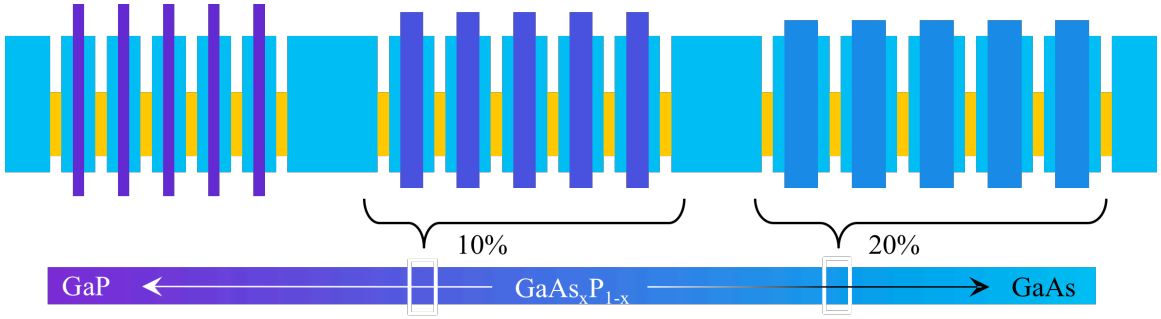

Figure 3.11. Cartoon depiction of the energy band diagram and layer structure of a varied As composition strain balancing layer.

The equation used for GaP can be similarly applied in the case of the inclusion of As in the alloy. As expected, the required thickness of GaAsP for appropriate balancing increases with As composition. Where, with GaP the thickness was determined to be 4.1 ML, with an As composition of 15%, the thickness increases to 4.8 ML. The calculation is provided at various As composition values is provided in Figure 3.12. Moving to a value 40% As moves the strain balancing layer thickness to about 6.5 ML. Assuming the lower threshold for uncertainty is 1 ML, this reduces the uncertainty in growth from approximately 25% to 16%.

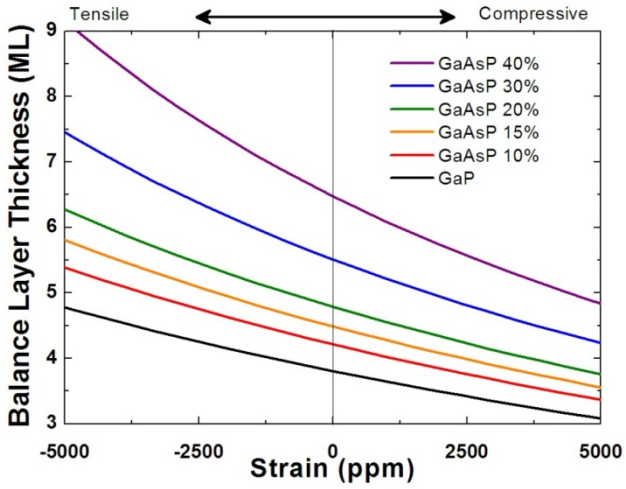

Figure 3.12. Calculation of necessary thickness of strain balancing layer for different As compositions.

3.4. Solar Cell results

Strain balancing techniques derived from this work have been shown to prove to improve both optical and mechanical properties of otherwise highly defective quantum dot superlattices. These improved strain balancing techniques should therefore improve solar cell device parameters, such as V_{oc}, since material quality and the photoluminescence intensities have been shown to improve, as shown in Figure 3.10. Previously, the open circuit voltage values gave just over 1 V for the baseline GaAs cell, while QD-embedded devices shown near 150 mV degradation. Devices were fabricated using both and optimized GaP thickness as well as the GaAsP alloy (at 15% As). Shown in Figure 3.13 (left) are the light *J-V* data for these two devices. The GaP-balanced devices showed improved V_{oc} values of 0.89 V and the GaAsP sample gave 0.95 V. Furthermore, the inclusion of GaAsP may be responsible for the further enhanced V_{oc}

value. In the latter case, the balancing layer may be more accurate due to improved growth rate accuracy associated with the thicker layer. This improvement can lead to further reduction in *i*-region recombination losses. The improved V_{oc} values, similar short circuit current densities and fill factors lead to an increase in solar cell efficiency from 11.7% to 13.3%

The material quality in the layers grown above the intrinsic layer (predominantly the emitter) has also shown evidence of improvement. Figure 3.13 (right) shows the external quantum efficiency of the same two devices. The low wavelength bulk EQE (indicative of high energy photons absorbed at the top of the cell) increases slightly for the device with GaAsP balancing layer. The inset in this figure shows that although there are differences in the current generated by the QD layers and this can be potentially associated with reduced tunneling thickness in the GaP-based superlattice.

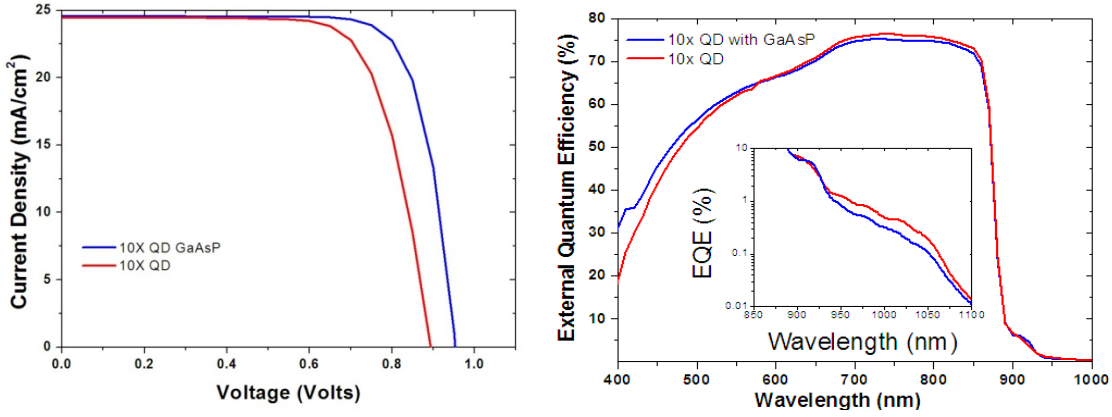

Figure 3.13. Left: Light J-V measurement of standard strain balanced 10-layer QD solar cell and modified GaAsP strain balancing layer. Right: EQE measurement of the same two samples.

It is beneficial for many types of QD-embedded devices to expand upon the limit of number of these layers. Even with the correct strain balancing conditions, there may be

a limit to this number, due to the inhomogeneous strain inherent in a three dimensional array such as we have here. Once a more accurate generalized theory for strain balancing the arrays was characterized, the implementation of increased numbers of layers could be confidently investigated. Two solar cells were subsequently grown, one with forty and one with sixty layers of strain balanced QD arrays. These were fabricated into photovoltaic devices and complete PV characterization was performed. Table 3.1 gives the raw extracted parameters from Figure 3.13 (left).

Table 3.1. Table of solar cell parameters from light *J-V* curve in Figure 3.13 (left).

QDSC Strain Balancing Material	J_{sc} (mA/cm^2)	V_{oc} (V)	*FF* (%)	η (%)
GaP	24.4	0.89	73	11.7
GaAsP	24.6	0.95	77	13.3

Figure 3.14 (left), shows the inverted AM0 illuminated *J-V* curves for a baseline sample and three QD embedded devices with 10, 40 and 60 layers of QDs. The baseline sample exhibits the typical solar cell parameters for a GaAs p-i-n cell of 1.04V, 24.1 mA/cm^2 and relatively high fill factor (FF) (83%). With 10 and 40 QD layers, the fill factor immediate drops (78%, 76%) due to small defects in the emitter region causing a decreased mobility and higher series resistance through the complex intrinsic region. The current is enhanced 24.9mA/cm^2 and 26mA/cm^2, respectively, with drops in voltage to 0.96 and 0.88V, respectively. This observed drop in voltage is most likely due to the increased dark current due to recombination in the *i*-region of these samples when compared with the low defect *i*-region of the baseline. Table 3.2 shows the solar cell parameters extracted from these curves.

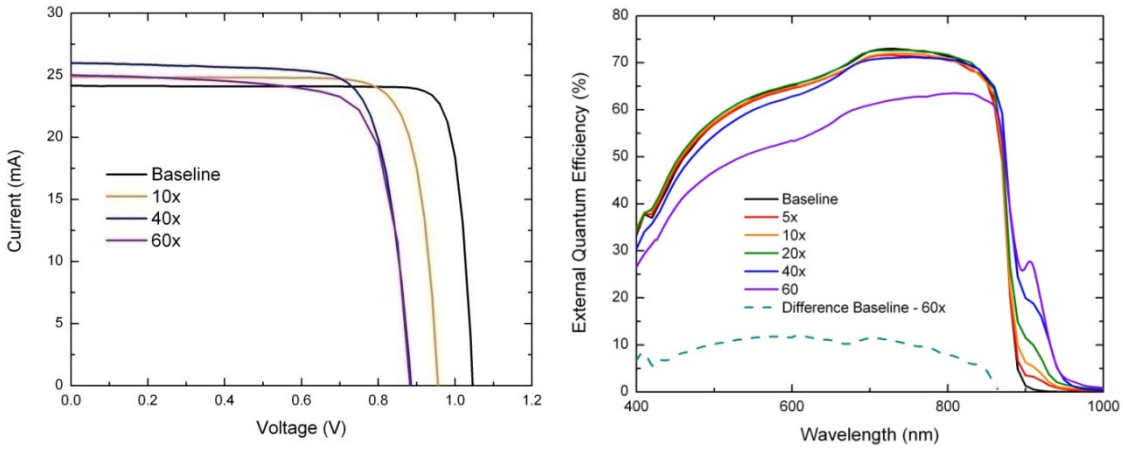

Figure 3.14. Left: I-V curves for 1cm^2 solar cell devices with increasing number of QD layers. Right: external quantum efficiency spectra for QD embedded *p-i-n* devices with varying number of QD layers.

When 60 layers of QDs are implemented, although there is a similar voltage loss compared with the 40x, the current does not continue this upward trend, and a significant shunting characteristic appears. This is due to the existence of defect pathways between the doped quasi neutral regions not present in the 10 and 40 layer devices. It is possible that in the 60 layer device, the superlattice critical thickness has been reached and significant relaxation has occurred, providing the propagation of threading dislocations often seen in highly strained semiconductor layers. The loss in current can be investigated by spectrally resolving the current generation in the devices. Figure 3.14 (right) shows these data as external quantum efficiency. It is apparent that although there is a continuous upward trend in the sub-GaAs bandgap "knee" with increasing layers of QDs, the loss in the visible wavelengths is significant (2 mA/cm^2, estimated extrapolation from 10x) in the 60x QD sample when compared to the others.

Table 3.2. Table of solar cell parameters from light *J-V* curve in Figure 3.14 (left).

	J_{sc} (mA/cm^2)	V_{oc} (V)	*FF* (%)	η (%)
Control	24.1	1.04	83	14.7
10x	24.9	0.96	78	13.6
40x	26.0	0.88	76	12.2
60x	25.0	0.88	69	11.3

To verify that the loss from the 60x is originating from material degradation, a model of the external quantum efficiency was created to simulate the effects of an emitter with decreasing carrier lifetime values. This model, (demonstrated by Nelson [69]), sums the current densities in all regions of the solar cell as a function of incoming photon wavelength. It takes into account current generation terms which can be obtained using the absorption coefficient and the incident spectrum, solving the continuity equation and Poisson's equation and arrives at a modified version of the current density equation shown in chapter 0.

Figure 3.15 (left) shows the effects of a decreasing emitter lifetime alongside the effects a decreasing lifetime in all device regions. This isolates the effects originating specifically from the emitter and illustrates the specific decrease in *EQE* from a decreased emitter carrier lifetime of only a few orders of magnitude. Adjusting lifetime values in this model and fitting to the data, evidence is conclusive that the material grown after the 60 layers of QDs has a significantly reduced carrier lifetime (11 ps) when compared to the samples with the control cell and the 10 and 40 layer structures (~1 ns). This suggests that somewhere between 40 and 60 layers, the QDs are reaching a critical limit as a superlattice since subsequently grown material appears degraded. This fact

confirms the above suggestion that relaxation is occurring at this number of layers and indicates a need for a more accurate method of strain compensation than that which was proposed here. Another possibility explored in the next chapter, is that QD structural characteristics are playing a role in the material quality in subsequently grown material. The strain balancing theory proposed here may work to a certain limit, but the balancing may become exceedingly sensitive with more and more QD layers.

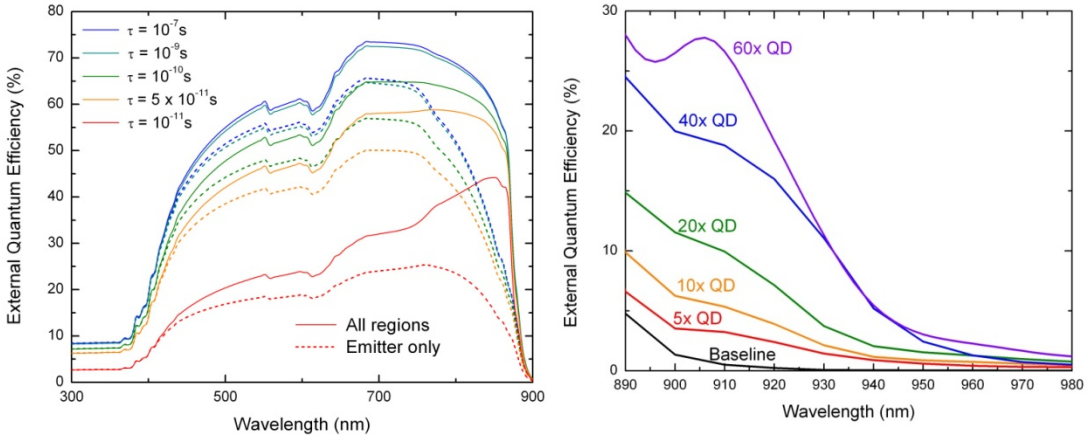

Figure 3.15**.** Left: Hovel model of EQE indicating degradation due to a decrease in carrier lifetimes. Right: a zoom in of Figure 3.14 (left) showing the detail of the sub-GaAs bandgap current increase.

This drawback does not seem to significantly affect the absorption and collection of carriers below the GaAs bandgap. Figure 3.15 (right) shows the systematic increase seen if focusing more closely on the wavelengths absorbed by the QD layers. The 60-layer QD sample, although degraded in the visible, shows an EQE value of ~28% above 890nm. Integrating under these curves and convolving with the solar spectrum, it is possible to extract the current generated by the device at specific wavelengths. A comparison of these values is shown in Figure 4.11 (left). Table 3.3 tabulates these values indicating the systematic increase provided by the inclusion of the QD layers.

Table 3.3. Integrated J_{sc} above 890 nm for the EQE curves in Figure 3.15.

	Integrated J_{sc} above 890 nm (mA/cm^2)
Control	0.10
5x	0.21
10x	0.30
20x	0.41
40x	0.79
60x	0.99

Fermi-Dirac statistics allow for a band-tail of absorption in the baseline sample's curve at room temperature (seen in Figure 3.15 (right). A systematic increase in the *EQE* values at these wavelengths is observed with increasing number of QD layers. At 60 layers, the current density contribution approaches 1mA/cm2. A slope is easily fit to these data points and a sub-GaAs bandgap current contribution can be obtained per quantum dot layer (0.017mA/cm2/QD layer). In order to truly capitalize this current boost, attention must be given to the loss in voltage with increasing number of QD layers. In order to do this successfully, the defects in the emitter must be minimized, minimizing emitter degradation and its associated current density loss. Also loss in voltage from defects arising from the intrinsic region must also be minimized. This second issue is addressed largely in the following chapter.

3.5. Conclusion

The improvement of strain balancing accuracy has been shown by this work to provide drastic improvements in material quality and device performance alike. However,

there are potential points of improvement that can be pursued within this subtopic. One of the advantages of using a weighted strain balancing thickness determination method is that it better approximates the necessary stress minimization necessary to avoid material defects. This is the first time an application of this method has been applied to any quantum dot system, and has proven very successful at device improvement. Its application to other type of quantum dot devices should also be considered with such success in solar cells.

However, this approximation is merely one of a first-order. Second order calculations can be made which take into account the inhomogeneous strain in the material within the superlattice layers. Again, just above the QD, the material is assumed to be in tension owing to the partial relaxation of the InAs at the top of the QD. Above a purely wetting layer location, the opposite effect may be seen, since this layer is still psuedomorphicly strained to GaAs. These two regions themselves may interact and there may be further deleterious effects un-accounted for in this approximation. A full, atomistic calculation such as those provided by other authors may be possible to better calculate an energy minimization for this system [55, 70].

Other materials for balancing layers may also be evaluated. A relatively simple study would be to continue the use of GaAsP with increasing As content. A series of samples stepping through this value of composition may be able to shed light on the effects of this thicker/lower barrier height material. InGaP may be another potential material choice as it avoids the group V composition variation undertaken by growing GaAsP. Further materials characterization may also be available for atomic lattice constant variation throughout the QD/balancing layer superlattice. High resolution TEM

is becoming more commonplace and is used to evaluate localized lattice constants in today's QD arrays [71].

In order to make successfully operating devices that can be applied to both the progress of bandgap-engineered solar cells and the intermediate band solar cell, it is important to solve the problems outlined at the end of the last section. The ultimate goal of all of these techniques would be to provide a pathway to growing a very high number of QD layers (100+) consistently and without degradation to the emitter (current loss) or the *i*-region material quality (voltage loss).

4. Optimum QD growth conditions

4.1. Introduction

Until this point, the focus of this body of work has been primarily on a single layer of the superlattice, namely the strain balancing layer. Although it has been shown that this layer is of high importance for proper device operation, it became a natural step within this thesis work to investigate the other layers of the repeat unit. The GaAs spacer layers haves some requirements such as being kept relatively thin for adherence to the intermediate band approach (see section 5.4). The InAs layers, however, have the highest degree of variability based on growth conditions because they are grown within the kinetically-driven growth regime (low temperatures, 495°C). Additionally, in these layers are those which give the device improved current densities, result in the scientific need to evaluate their formation mechanisms, structural characteristics, and ultimately their growth conditions.

Within these growth conditions are a number of variables which have been relatively widely studied for the InAs/GaAs system. Some of the most significant growth conditions which affect QD nucleation and arrangement are as follows:

- Temperature
- V/III Ratio
- Chamber Pressure
- Injector Flow Rate
- InAs Coverage Value

Temperature effects on QD growth have been studied since their growth began. More recently, studies have been performed under the lens of photovoltaic device incorporation

by Hubbard [72]. It was found that a growth temperature of 495°C give the strongest PL signal. This was in part due to the lack of surface energy provided at low temperatures limiting In adatom surface diffusion leading to disorganized, polydispersed QD sizes. At higher temperatures, In desorption can occur, also resulting in lower QD densities. This study, among others for MBE [73] and MOCVD [74] show that V/III ratio can affect dot densities. Reduction in V/III ratio also led to drastically improved spatial uniformity [72]. A ten-fold increased in grow rate was found to slightly improve QD density (from 49-57%) [73]. Although chamber pressure and alkyl injector flow rate are very important to QD growth, they are not discussed here, as their conditions vary between MOCVD reactors and are difficult to conclude upon for the scientific community.

One of the most critical parameters for QD growth is the coverage value. Beyond the critical thickness of 3D island formation (θ_c), there is a period which only small, coherent QDs form. It is these that are of interest for these devices as they exhibit the highest optical quality and most uniform size. Beyond this point, Oswalt ripening occurs, forming large, incoherent, optically inactive islands begin forming, due to the coalescence of the smaller, mobile InAs structures [75]. This results in point defects at the site of nucleation, which can cause second order defects in subsequently grown material, such as threading dislocations. In order to avoid these latter conditions, the InAs coverage value was studied in an attempt to optimize this parameter in the frame of the photovoltaic devices used here.

4.2. InAs coverage

The QD formation includes both the physical islands, as well as the wetting layer. This two-aspect layer system imparts a difficulty on the definition of a thickness value. It

is for this reason that a 'coverage value,' θ, is defined and accepted among growers of the S-K mode. It is a value that represents an effective thickness of a layer based on growth rate (0.26 monolayers (ML) per second) and time, and is therefore reported in units of length. This was calculated by depositing a thick InAs layer, and using a scanning electron microscope measurement to determine average height of pyramidal islands.

For the InAs/GaAs QD system, it is well understood that there is a narrow range of InAs coverage (1.7 – 2.5 ML) in which acceptable optical performance can be achieved [76]. The samples grown here fall within this range at θ = 1.82, 2.10, 2.17, 2.24, 3.31 ML, calculated by growth rate and time. To investigate the structural and optical results of varying the InAs coverage, low temperature PL as well as both AFM images and HRXRD was performed.

With any superlattice structure involving layers with different lattice constants, it is important to quantitatively characterize the strain in the samples. It has been shown previously that the strain balancing layer (GaP) can be reasonably tuned using a 1st order calculation of the appropriate strain compensation layer thickness section 3.3. This method is employed here, but despite QD dimensional changes, the GaP layer thickness is maintained throughout the structure. This choice was made so that the only experimental variable was the InAs dot size. Dot diameters did not change enough to justify an increased QD footprint. Although QD densities did increase for the larger dots, the decrease in the smaller dots accounts for some of this increase. As will be shown, QD height is the most significantly varied geometrical dimension for the small QDs. Altering the GaP thickness from previous studies would have also altered the tunneling probabilities of the transition states investigated here and was therefore avoided.

4.2.1. Atomic Force Microscopy

From visual inspection of the AFM images, there exists a bi-modal distribution in the QD size. The smaller sized QDs, on the order of 3-5 nm thick, and 25-35 nm in diameter are coherent, unrelaxed, defect free, islands of InAs. The larger islands in the images are almost an order of magnitude in size difference with heights of 20-25 nm and diameters ranging from 65 to 105 nm. These islands are a combination of coalesced smaller islands and additional InAs which adsorbs after relaxation, as the lattice constant that exists and these surfaces is energetically favorable to unsettled InAs. Consequently, they have phase interfaces and relaxation locations resulting in point defects acting as recombination centers and are considered optically inactive [75]. These centers can cause severe loss in open circuit voltage in quantum dot embedded solar cells. Threading dislocations arising from these point defects can propagate into the emitter, and as discussed in chapter 3, can then cause short circuit current density losses in these cells. It is therefore these large QDs that that are undesirable for these devices as well as any optoelectronic device which take advantage of quantum confinement via quantum dots.

Figure 4.1 shows the AFM images of the 1.82, 2.17 and 2.31 ML InAs coverage values. Smaller QDs align themselves with the step edges discussed in chapter 2. It is less clear whether this is occurring with the larger QDs. Interestingly, the smaller dots decrease in density with increased Θ. This is largely due to the increase in density of the larger mode of QDs. The smaller dots range from $3.6 \times 10^{10}\ cm^{-2}$ to $2.0 \times 10^{10}\ cm^{-2}$ as the coverage value increases. Larger dot densities range from $1.5 \times 10^{8}\ cm^{-2}$ to $1.21 \times 10^{9}\ cm^{-2}$ indicating the favorability of InAs to form larger islands with increased availability of In and As atoms.

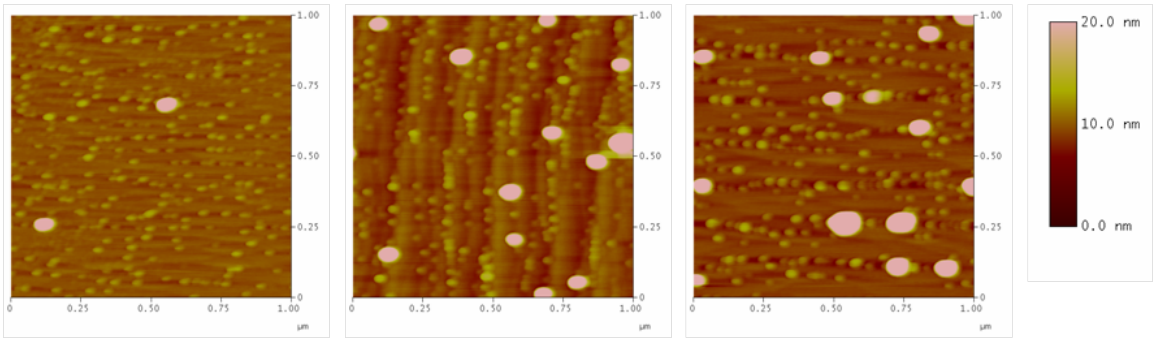

Figure 4.1**.** Atomic force microscopy images of surface of test samples with varying InAs coverage. QDs appear in a two mode distribution. Increasing QD size and density track roughly with coverage value. Images read left to right: (θ = 1.82, 2.17 and 2.31 ML)

QD diameters do not show any particular trend in size ranging from 20 to 45 nm for the small mode, and 65 to 125 for the larger QDs. QD heights however, did show an interesting trend. The small QDs increased in height with increasing coverage values, from 3.65nm, 4.20nm to 5.54 nm. The larger QD size did not show any significant trend. These results indicate that increasing InAs coverage leads to increasing small dot heights and increasing large dot densities. Table 4.1 outlines these statistics obtained from analysis of the AFM images using the software provided by the Dimension AFM, DI Nanoscope Image. Five line scans were taken for each image independently for both small and large QDs. 2 x 2 cm^2 images (not shown) were used, in order to reduce uncertainty associated with anomalies in a 1 x 1 cm^2 image, to count the number of quantum dots by hand.

Table 4.1. Statistical data extracted from AFM images in Figure 4.1 and binned by "small" and "large."

Small QDs				
InAs (ML)	Density (cm^{-3})	Min. Dia. (nm)	Max. Dia. (nm)	Height (nm)
1.82	3.6×10^{10}	24	38	3.65
2.10	3.0×10^{10}	20	38	3.81
2.17	2.5×10^{10}	20	45	4.20
2.24	2.0×10^{10}	25	45	4.86
2.31	2.2×10^{10}	25	40	5.54

Large QDs				
InAs (ML)	Density (cm^{-3})	Min. Dia. (nm)	Max. Dia. (nm)	Height (nm)
1.82	1.5×10^{8}	75	100	21.0
2.10	5.0×10^{8}	65	105	24.7
2.17	9.0×10^{8}	65	105	22.2
2.24	1.0×10^{9}	65	125	23.3
2.31	1.2×10^{9}	70	120	23.1

A separate statistical image analysis program, Scanning Probe Image Processor, uses a height flooding method to recognize entities in data set containing x and y coordinates and associated height values. This is used to gather the height and diameter data from the AFM images for histograms which are plotted in Figure 4.2 for the first three coverage value samples. These three samples give us the finest detail of the five for information pertaining to the mechanics before and after the onset of the large quantum dot formation. It is immediately apparent that in the sample with the lowest InAs coverage value, 1.82 ML, there appears to be a very tight distribution of both height and (to a lesser degree) diameter peaking at roughly 2 nm and 15 nm, respectively. Height values shift by roughly 1.5 nm between the two software programs used, and is assumed to be a result of an incorrect offset made by the SPIP program, and the DI Nanoscope Image software is used as a baseline.

As the InAs increases in coverage value, and we approach and pass the onset (or critical thickness) of the large, incoherent QD formation, these QD counts begin to appear more significantly. In the sample with 2.17 ML a second, distinct peak in the data

begins to occur. In the 2.10 ML sample it is clear that the small-dot peak has shifted in height by about 0.75 nm. This is due to an accumulation of InAs at the top of the QD. The average QD height returns to a value of 1.5 nm as the secondary, large-dot peak begins to form indicating that InAs has migrated to the larger QDs from the top of the small QDs. These larger-dot peaks can be estimated to be at an average of 12 and 55 nm for the height and diameter, respectively. This evolution of the larger, optically inactive islands (coalesced QDs) becomes very apparent.

It is also of note from Table 4.1 that the small QD density decreases with increasing coverage value. This indicates that the InAs used to form the larger QDs consists not only of atoms that have been relocated from the top of QDs, but also of entire small QDs. This supports the fact that small QDs are coalescing. The fact that the large QD density increases with increased coverage value also corroborates this mechanical process.

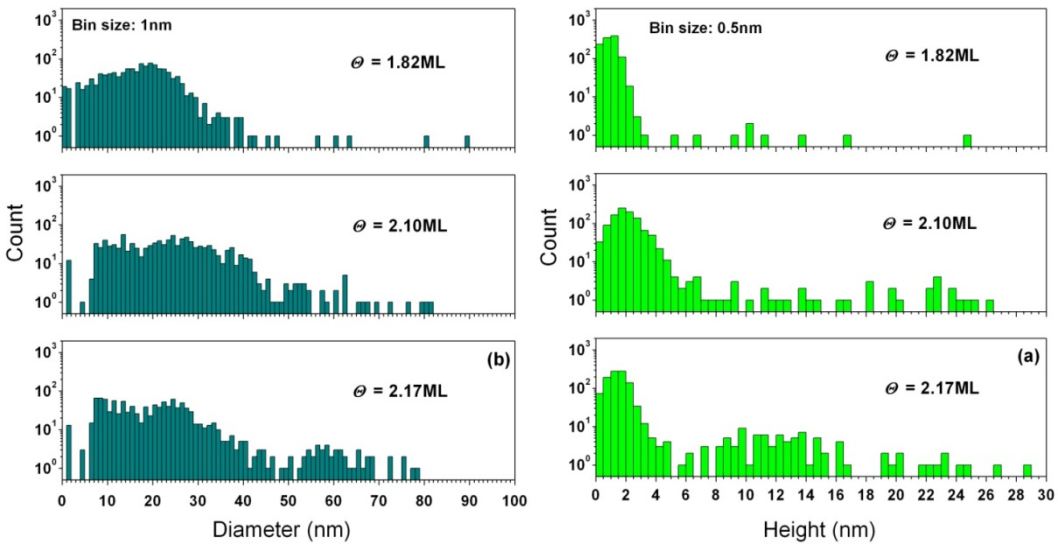

Figure 4.2**.** Histograms of QD diameter and height obtained from AFM images for QD test structures with varying InAs coverage values.

It is clear from these data that a reduced InAs coverage value is a pathway to avoiding large, defective quantum dots. Both a reduction in large dot density is observed with decreasing InAs coverage, and in particular for the 1.82 ML coverage value, a negligible density of QDs is found. This pathway is of interest for pursuing optoelectronic devices that use these structures as it is a simple, quantifiable method of improving physical material properties of these structures. Subsequent sections of this chapter address other characterization techniques with these samples.

4.2.2. Photoluminescence and High Resolution X-Ray Diffraction

One of the most significant measurement of the optical quality on these types of test structures is photoluminescence, as it is a direct measurement of the radiative recombination of carriers in the confined states. After a carrier excitation event such as a photon separated electron-hole pair occurs, it is subject to an array of possible paths including both non-radiative and radiative recombination, thermal excitation (out of the confined state), tunneling (into another confined state), and other recombination processes such as Auger. When performed at low temperature, photoluminescence measurements can provide very high detail due to suppressed of the thermal excitation process, thereby increasing the carrier available for all other processes, including radiative recombination and can increase the radiative lifetime in the confined states.

Increased carrier lifetime in the QD states allow for very high emission efficiency. Shown in Figure 4.3, are the PL spectra at 80 K as a function of InAs coverage value. The larger the QD heights, the deeper the QD state is expected to be, and this is the case here. The smallest θ value gives the shallowest state, and therefore the highest emission energy. This effect systematically red-shifts with increasing coverage, indicating a slight

increase in energy state. This is a shift from 1.22 to 1.18 eV (40 meV difference). More interestingly, however is the shift in the full-width at half-maximum (FWHM). This is indicative of inhomogeneous broadening associated with the natural distribution of QDs. These curves show broadening with increasing coverage value indicating an increase in the distribution in the QD size which corresponds to the increased volume of the InAs producing a larger variation in QD height.

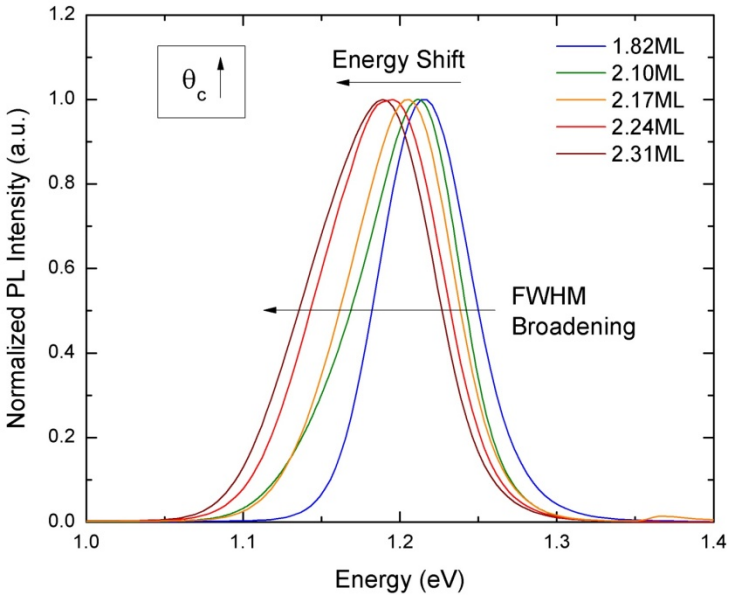

Figure 4.3**.** Low temperature PL measurements of QD test structures with varying InAs coverage values.

High resolution x-ray diffraction is used to study the strain in these samples. Figure 4.4 shows symmetric 2θ/ω scans in the [004] plane for each of the five test structures and provide insight into the structural integrity of these test samples. The 0^{th} order superlattice peak, labeled SL(0), can be seen just to the left of the GaAs Bragg peak indicating slight compressive residual strain in the layer structure.

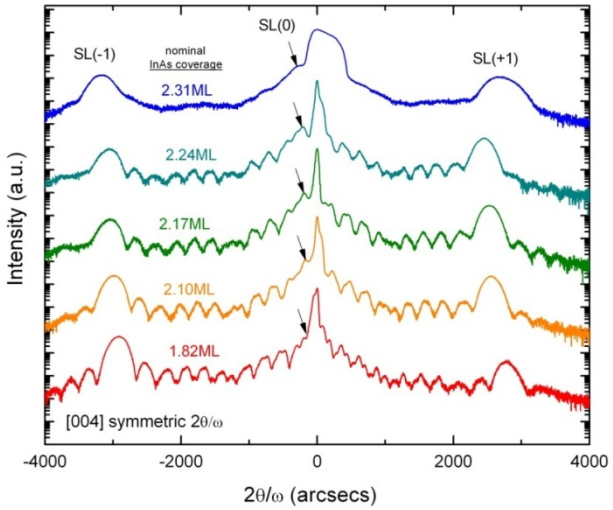

Figure 4.4. HRXRD measurements of QD test structures with varying InAs coverage values.

The strain and periodicity are extracted as discussed in chapter 3 and can be seen in Table 4.2. This strain value gradually moves more negatively in 2θ value with increasing coverage value. This is clearly due to the increasing compressive strain associated with the larger volume of InAs. As the larger quantum dots begin to form, the GaP strain balancing become insufficient for proper balancing. No significant trend in periodicity is seen for the samples between 1.82 and 2.17ML InAs, ranging from 19.4 to 20.2nm. The 2.31ML InAs sample, however decreases below this range at 18.9nm. This suggests that there is some relaxation in the superlattice, and as the average lattice constant shifts to larger values, the lattice mismatch is smaller than the previous four samples. This results in an altered SK growth mode. This claim would be better supported with the measurement of asymmetric XRD scans as these can provide in-plane lattice constant shifts. Pendellosung fringes can be seen clearly in all three samples of lower InAs coverage. These disappear in the 2.31ML sample, indicating a loss in interface quality characteristic of layer relaxation. Also interesting is the much broader GaAs Bragg peak associated with the 2.31ML sample. This indicates diffraction from a

tensile layer, most likely the 33nm spacer GaAs layer. This layer might be in tension since the relaxation of the SL below it now has a larger lattice constant. The range of samples tested here illustrates that the InAs coverage value plays a role in strain balancing in the superlattice, and at a critical thickness can cause significant layer degradation. The lowest value of Θ_c gives not only the lowest bi-modal spread, but also the least strained superlattice.

Table 4.2. Extracted periodicity and strain values from HRXRD shown in Figure 4.4.

InAs coverage (ML)	Strain (ppm)	Periodicity (Å)
2.31	916	189
2.24	1297	202
2.17	1016	197
2.10	802	199
1.82	265	194

No significant shift in periodicity of the superlattice repeat unit was found with coverage value, as it is thought that the increased volume of InAs on the surface manifests primarily in QD height increases, and increased density of larger, incoherent QDs. The table below shows the periodicities calculated from the x-ray in Figure 4.4. Also shown is the calculated strain values, which for does not change much for the coverage values between 2.1 and 2.31 ML. These data can be compared in Table 4.2. This is most likely due to the onset of the larger QD islands sometime after 1.8 ML of growth, as confirmed by the AFM images in section 4.2.1. The strain is minimized in the sample with 1.8 ML indicating that the GaP thickness designed uniquely for these smaller

sizes QDs is accurate, but departs from ideal upon the onset of the larger, undesirable islands.

4.3. Solar Cell Results

The results thus far in this section showed that with coverage of 1.8 ML of InAs, smaller, more uniform coverage of QDs can be realized. They show improved PL FWHM (or narrowing inhomogeneous broadening), they can be better designed for strain balancing, and the large, optically inactive islands are reduced to a relatively insignificant density. It is therefore of interest to move to explore slightly smaller InAs coverage values in order to approach more uniform distribution and improve radiative recombination characteristics in these devices in the pursuit of the improvement of solar cell device parameters.

Figure 4.5 shows the 1 sun AM0 illuminated J-V curves for the baseline GaAs *p-i-n* and the 10x QD GaP strain balanced solar cells with the lower InAs coverage value. The baseline sample exhibited characteristics typical of GaAs single junction solar cells with a J_{sc} of 22.6 mA/cm^2. In the QD embedded sample, J_{sc} was enhanced to 23.1 mA/cm^2, giving a 2.2% increase in short circuit current over the baseline solar cell current. This increase is larger than typical of QD enhanced solar cells, shown to give increases as high as 0.025 mA/cm^2/QD layer calculated by the slope of J_{sc} plotted versus QD layer number in Hubbard, et al. [77] and can be seen here in Figure 4.11. This may be due to small differences in measurement of the bulk GaAs absorption wavelength region. The open circuit voltage for the standard control GaAs cell was typical of a high quality GaAs solar cell with a value of 1.041 V. The ten layer QD sample showed slight degradation of this voltage value, with a loss of about 47 mV. The source of this

improved voltage value compared to that of the control is due to an improvement in the strain balancing by the significant suppression of the density of the secondary, larger coalesced QD mode using a reduced InAs coverage. This V_{oc} value, 0.994 V is the highest InAs/GaAs-based QD solar cell voltage to date. The fill factor variation was insignificant between the two samples, and the efficiencies are comparable at 13.8 and 13.5% for the control and QD solar cell, respectively with negligible different in fill factors (~81%).

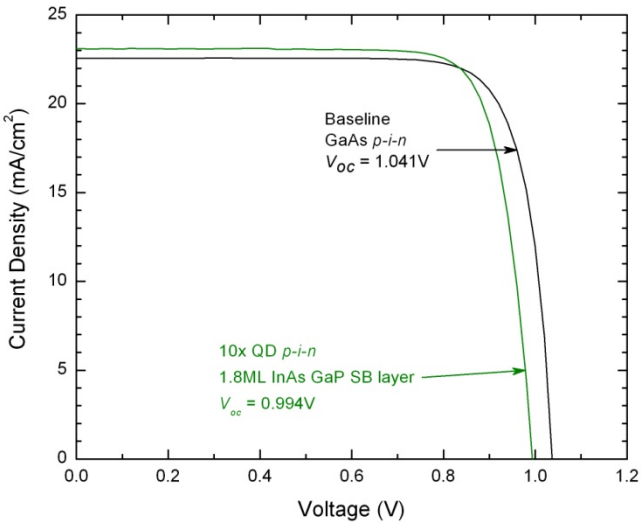

Figure 4.5. Light J-V measurements showing 10X QD solar cell with only 50 mV loss in open circuit voltage.

Spectrally resolving the short circuit current density can be evaluated using spectral responsivity measurements and then converted to external quantum efficiency (EQE). Figure 4.6 (left) shows the comparison of this data for the two samples shown in Figure 4.5, with the addition of the solar cell with 2.1 ML InAs to show how the spectral sensitivity has changed below the GaAs bandedge. Peak bulk *EQE* values are equivalent for all samples near 73%. Typical measured reflectivity values for these samples were ~30% [56] giving an internal quantum efficiency near unity. The sub-GaAs bandgap (> 880 nm) absorption is clearly enhanced for all InAs QD devices indicating the source of

the improved J_{sc}. The numerical integration of the spectral responsivity and the AM0 spectrum (data vectors) was used to calculate the expected short circuit current values and deviated from the illuminated light *J-V* measurements by 7-12%. In addition, this calculation was performed specifically for the sub-GaAs absorption portion of the spectrum (> 880 nm), and was found to be relatively constant across all 3 QDSC samples, varying by only 4%. Slight differences in the bulk wavelength EQE offset any influence of the absorption above 880 nm on the differences in the J_{sc} values of the QD enhanced devices.

In Figure 4.6 (right), the sub-GaAs bandedge EQE is scaled (semi-logarithmic) to highlight the fine structure and compared with the electroluminescence (EL) spectra (linear). EL was measured using an injection current density of 200 mA/cm^2. All three EQE spectra show absorption features near 940, 985 and 1035 nm. The 2.1 ML sample shows weaker absorption at the 940 nm peak. This near band-edge peak is typically associated with the QW-like wetting layer (WL) [36]. It is also apparent that emission seen in the EL spectra, correlate well with the slope changes of the EQE absorption peaks. These peaks appear at 950, 995 and 1050 nm, indicating a Stokes' shift of 10-15 nm (12-20 meV). This shift is inherent in confined structures and represents the difference in energy observed by absorption and emission. The reciprocal nature of absorption and emission differ only by collection and injection efficiencies in the case of EQE and EL measurement. The domination of radiative recombination (seen in the EL spectra) in the deeper infrared (IR) states (1050 nm) of the 2.1 ML sample is thought to be due to an increase in volume of QDs (from height increase). The reduced collection efficiency of the deeper IR QD states is due to the larger conduction band offset of these

states in comparison to the wetting layer emission (950 nm). This is primarily due to the reduced thermal escape and Fowler-Nordheim tunneling event probabilities associated with deeper confined energy levels.

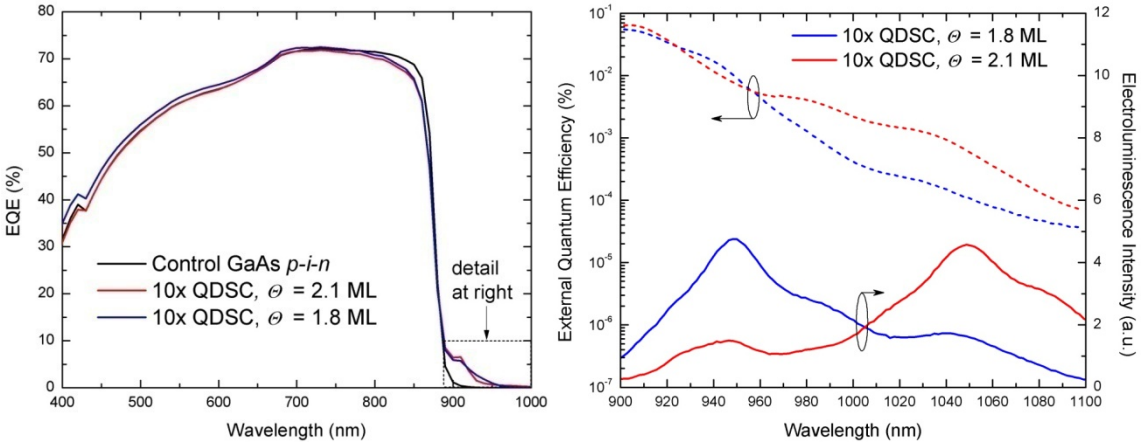

Figure 4.6. Left: EQE measurements of baseline, standard QD solar cell and QD solar cell with reduced InAs coverage value. Right: EQE and electroluminescence data for both QD solar cells.

With the success of the lowered InAs coverage value when fully implemented into the 10-layer QD solar cell, it became the obvious next step to increase the number of layers and look for further current enhancement and continued prevention of V_{oc} loss. The ten-layer structure was repeated with 20 and 40 layers for comparison.

Figure 4.7 shows the 1 sun AM0 illuminated *J-V* curves for the baseline GaAs *p-i-n* and the 10, 20, and 40-period QD solar cells. The device parameters are tabulated in

. The baseline sample exhibited characteristics typical of GaAs single junction solar cells with a J_{sc} of 22.47 mA/cm^2. In the 40-period QD embedded sample, J_{sc} was enhanced to 23.78 mA/cm^2, giving a 5.8% increase in short circuit current over the baseline solar cell current. The increase with 10 and 20 periods is systematic at 3.3 and 4.8%, respectively. The open circuit voltage for the control GaAs cell was typical of a high quality GaAs solar cell with a value of 1.039 V. The ten layer QD sample showed

slight degradation of this voltage value, with a loss of about 42 mV. The source of the improved voltage value compared to that of the control is due to an improvement in the strain balancing by the significant suppression of the density of the secondary, larger coalesced QD mode using the reduced InAs coverage [38].

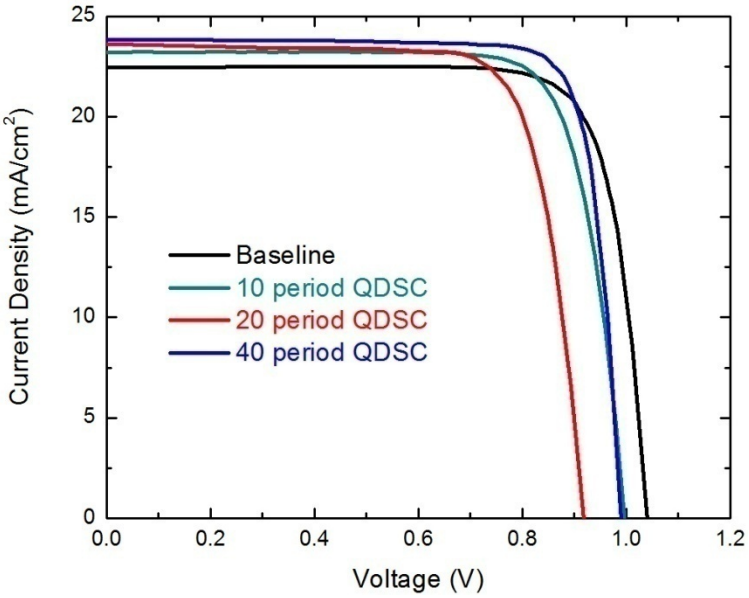

Figure 4.7. Light *J-V* measurements of baseline and QD solar cells with increasing number of QD layers.

The 20-period device showed a significantly degraded voltage value. The cross-wafer standard deviation for this sample was 36 mV and a reduced fill factor was observed, indicating a potential variation in wet isolation etch-depth and poor metallization contacting adhesion. The 40-period QD cell exhibited a voltage of 0.990 V, comparable to that of the 10-layer cell. The improved current and fill factor for this device resulted in an efficiency value of 14.3%. This is a relative efficiency improvement of 3.6% over the control cell, or an absolute efficiency improvement of 0.5%. The fill factor variation is not insignificant between the 40-layer and the control cells, but represents only 2.7% relative efficiency improvement contribution from the fill factor. This indicated that the 40-layer structure would still exhibit enhanced efficiency with an

identical fill factor as the control cell.

Table 4.3. Solar cell device parameters extracted from AM0 light *J-V* measurements shown in Figure 4.7.

	I_{sc} (mA/cm²)	V_{oc} (V)	FF (%)	η (%)
Baseline	22.47	1.039	80.0	13.8
10x	23.21	0.997	78.5	13.4
20x	23.54	0.918	76.8	12.2
40x	23.78	0.990	82.3	14.3

Figure 4.8 (left) shows the external quantum efficiency (EQE) from this measurement as a function of number of QD layers (10-40x) and the control device. The response typical of a GaAs solar cell is exhibited with a bandedge near 875 nm for all four samples. Solar cells with layers of QDs exhibited relatively equivalent response in the visible wavelength region (400-875 nm). This indicates good material quality throughout the devices, signifying emitter degradation does not occur as seen previously in cells with high numbers of layers at higher coverage values [78]. With increased numbers of stacked layers, the sensitivity of strain balancing may be reduced with the use of 1.8 ML compared to 2.1 ML coverage of previous QD solar cells. Therefore emitter degradation seen previously may be mitigated with improved InAs coverage values and is not seen here. The absorption observed beyond 875 nm is due to the inclusion of InAs QD and wetting layer (WL) and is not present in the control cell. The relative increase in absorption and collection occurring at these wavelengths with greater numbers of QD layers can also be seen here.

This increase is highlighted in Figure 4.8 (right). This shows, in finer detail, the EQE of these cells beyond 880 nm. The peak values (~915 nm) range from 6 to 22% EQE. Using an integration with the AM0 spectrum, the contribution from the 40-period QD cell approaches 0.9 mA/cm^2. This leads to an approximate increase of 0.55% EQE per QD layer observed at this peak value. The suppressed responsivity peaks above 940 nm, is due to the poor extraction efficiency associated with absorbing states of this depth (100-180 meV below the conduction band (ΔE)), as opposed to the collection-dominating near-bandedge state at 910 nm (ΔE = 45 meV). This is further confirmed by electroluminescence measurements.

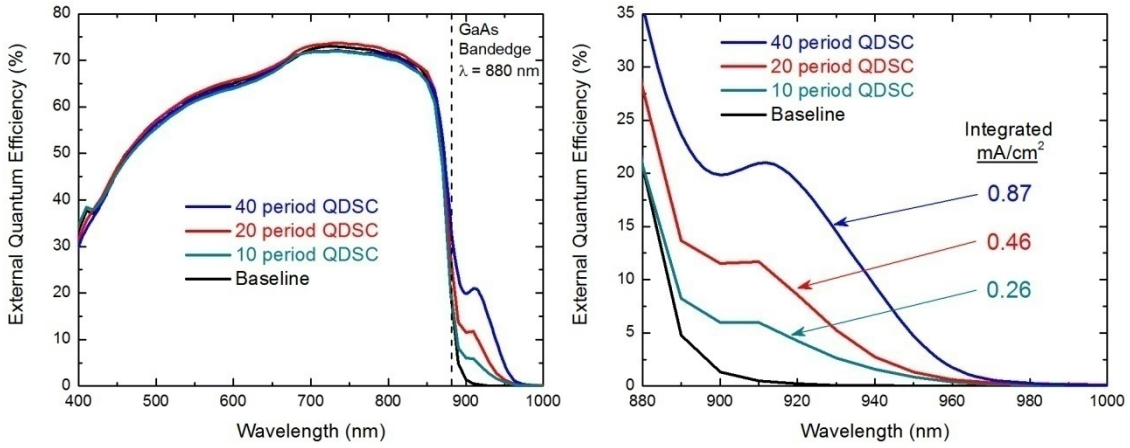

Figure 4.8**.** Left: External quantum efficiency measurements for the three QD and the baseline/control GaAs *p-i-n* solar cell devices, indicating no significant degradation in the bulk GaAs absorption wavelengths and a consistent increase in sub-GaAs bandedge EQE values with increasing numbers of QD layers. Right: External quantum efficiency measurements for the three QD and the baseline/control GaAs *p-i-n* solar cell devices, indicating no significant degradation in the bulk GaAs absorption wavelengths and a consistent increase in sub-GaAs bandedge EQE values with increasing numbers of QD layers.

4.3.1. Further Device Characterization

Electroluminescence (EL) was measured identically for the three QD samples, using an injection current of 100 mA/cm^2 and is shown in Figure 4.9 (left). Spectra

detection was performed using an Ocean Optics NIR512 InGaAs infrared photodetector and all samples were measured under equivalent optical distances. All three QD-embedded samples show a weak GaAs bandedge emission, indicating high QD injection efficiency. The 10- and 20-period samples exhibit a strong WL-like state near 940 nm, and a deeper QD emission region between 1000 and 1100 nm. The 40-period cell, however, exhibits a much stronger increase in the WL-like state, and degraded intensity in the QD emission regions when compared with the lower-QD number structures. This anomaly was thought to be explainable by a natural loss in strain at higher period numbers, removing the Stranksi-Krastinow mismatch requirement for dot formation, and did not contribute significantly to the devices results. However, HRXRD measurements (Figure 4.10) indicated insignificant shifts in out-of-plane superlattice strain values with 204, 485, and -32 ppm, for the 10-, 20-, and 40-period structures, respectively, indicating general structural integrity throughout the superlattice. Integrated EL curves (Figure 4.9, right) showed a systematic, linear increase in intensity with values of 1.0×10^6, 1.4×10^6, 2.2×10^6 a.u., for the 10-, 20-, and 40-period structures, respectively. This signifies equivalent overall device injection and emission efficiencies for all three QD embedded samples.

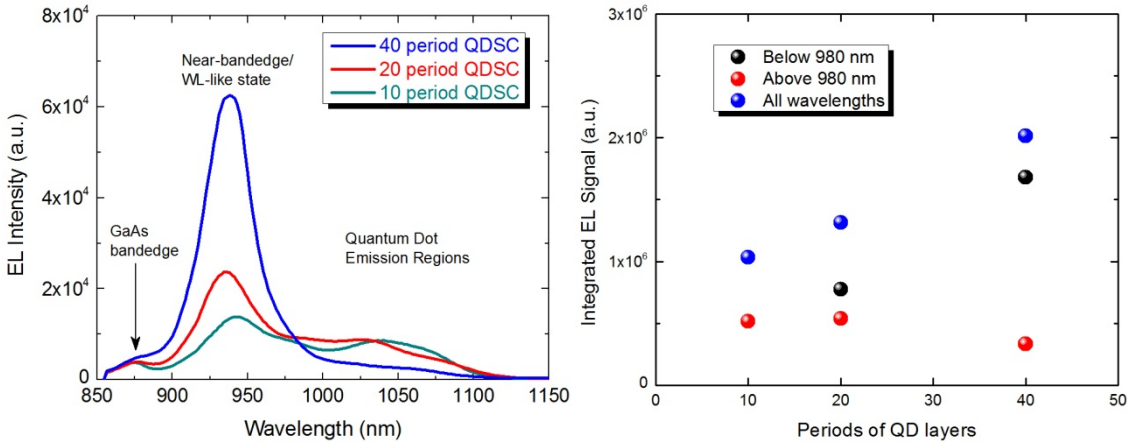

Figure 4.9**.** Left: Electroluminescence measurements for the three QD solar cell devices, indicating a strong increase in WL-states with increased QD layer numbers. Right: A breakdown of the spectral region of the EL indicating where majority of emission is coming from.

In order to further investigate the voltage loss associated with the 20x layer and to see if any other structural anomalies were present in these devices, HRXRD was performed on all three samples. Figure 4.10 indicates that the three samples are relatively lattice matched with the largest strain (20X sample) being 485 ppm (tensile). Also the periodicity did not change much with the values being 13.1 nm +/- 1 nm. These results are not convincing for a structure reason behind the loss in voltage for the 20 layer device. This indicates that the sample potentially had a fabrication problem and should be repeated for more accurate evaluation of the nature of this loss.

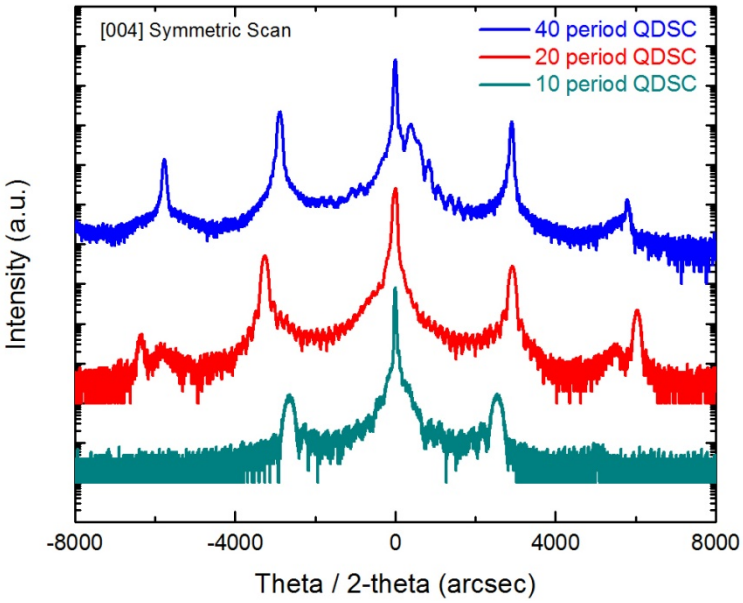

Figure 4.10**.** HRXRD measurement of series of solar cells with increasing numbers of QD layers.

Despite the 20-layer result, the high open circuit voltage (comparable with a standard GaAs solar cell), and improved short current density, of these QD enhanced GaAs solar cells is a promising result, as it represents a clear path forward using QD bandgap engineering for efficiency enhancement of III-V solar cells.

The continuation of adding more QD layers to the devices is one of the key factors in improving device performance. When arranged on the same plots, the trends in open circuit voltage and short circuit current shed light on the true potential of these devices. In Figure 4.11, these values are plotted. The voltage loss associated with the original growth type (Θ = 2.1 ML) systematically dropped to 150 mV lower than the GaAs cell. It appears to exhibit a saturation point with diminishing reduction in voltage with additional layers. It was shown, however, that at 60 layers, the loss in current due to emitter degradation began to become significant such that any advantage of voltage saturation with increased QD layers was eliminated [78]. With the improved QD epitaxy recipe, the minimization of the large, coalesced QD has resulted in only 50 mV reduction

from the control cell. In 9(b), the tracking of short circuit current with increased QD number can be shown to have slight improvement with the reduced Θ. Using the original recipe, a short circuit current gain was 0.017 mA/cm^2/QD layer [79]. Overlaid in this figure, are the short circuit current values from this study. There is a modest increase in the per-QD-layer metric to that of 0.020 mA/cm^2/QD layer. If emitter degradation and voltage loss mechanisms continues to be suppressed, higher number of QD layered-devices may be able to show further enhancements in efficiency and is the current focus of this research group.

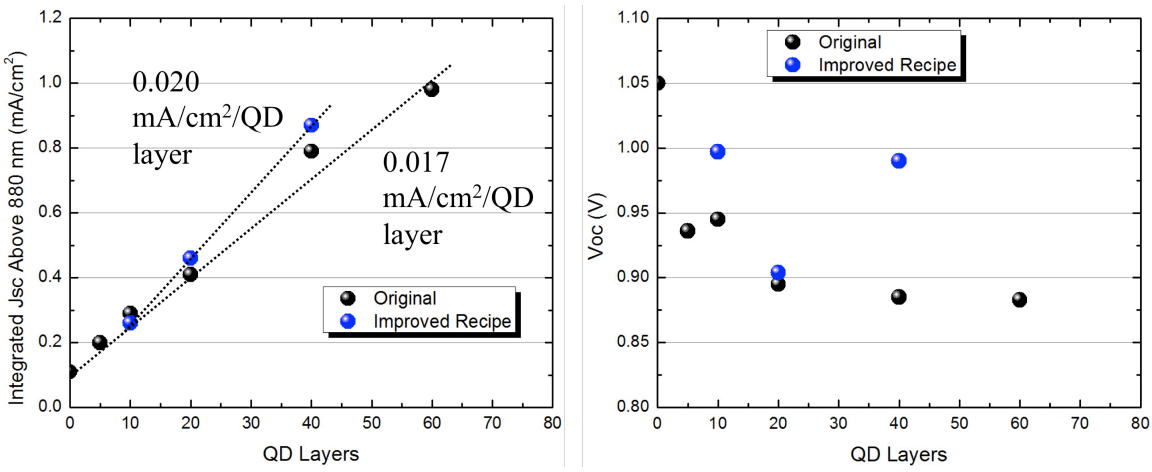

Figure 4.11. Left: Short circuit current tracking with QD layer number. This plot shows the improvement of slope of the improved QD growth scheme. Right: Open-circuit voltage tracking with QD layer number

4.4. Conclusion

Although there exist other methods in literature to limit the density of, and ultimately, eliminate large QDs, reducing the InAs coverage value is a simple and effective method which shows definitive improvement in material quality of both the superlattice region and the subsequently grown material. It would also be beneficial for

any optoelectronic device to remove these defective, coalesced QDs arising from Oswalt ripening, as they are detrimental to device performance and not optically active.

Reducing the coverage value has been shown here to not only improve the material quality, but the usage of the improved material has shown to improve solar cell device parameters. This includes both the avoidance of current density losses in QD embedded solar cells, as well as an improvement in open circuit voltage by over 100 mV. This has provided the first efficiency improvement in QD-embedded solar cells with an increase of 0.5% absolute efficiency.

5. Photon and Carrier Management

The physics of the operation of standard solar cells involve two major functions, absorption and collection. From the beginning of photovoltaic device research, efforts have focused on both of these functions for a wide variety of materials. For this reason, it is important to consider these functions when investigating nanostructured solar cells as well. This chapter will focus on a number these aspects with respect to incident photon intensity (concentration), introduce a third function in addition to absorption and collection specific to nanostructured solar cells, and evaluate these processes as they affect the intermediate band solar cell.

5.1. Solar cells under concentration

One of the most simplistic concepts in improving the efficiency of a particular solar cell, is by increasing the intensity of the incoming photon flux. It is well known that efficiency increases logarithmically with light intensity. Additionally, high injection conditions can potentially fill traps generate by defects and can therefore be a useful measurement to investigate this particular effect in QD solar cells [80].

A number of arguments lead to the potential improvement of efficiency using quantum dots in solar cells tested and operated under concentrated sunlight. Because QD solar cells have the ability to improve the short circuit current at one sun, it is logical to assume that this trend will continue linearly with concentration, therefore the efficiency should remain constant with increasing current from higher solar intensity. However, voltage improves on a scale of the natural log of the concentration as well. Under this assumption, efficiency should (and does) improve under concentrated sunlight for both a

baseline and a QD-embedded solar cell. The voltage for a QD cell, however, is much lower at one sun than the baseline, thus having higher capability of regaining low voltages due to trap filling. With this theory, quantum dot and baseline cells were grown and tested under concentration. Other important potential benefits include lower temperature dependence of QD solar cells has been previously shown.

Series resistance becomes a large limiting factor as sunlight is concentrated and currents increase (due to I^2R power losses). The PC1D solar cell simulator program was used in Figure 5.1 to determine the effects of series resistance on fill factor and efficiency as a function of concentration. At a reasonable series resistance value of 0.43 ohms (shown in Figure 5.1, left), the efficiency maximizes at about 8 suns. This is not ideal as current high efficiency cells are typically tested between 250-450 suns. This gave insight into the necessary grid metallization improvements that may be necessary for full device testing under concentration.

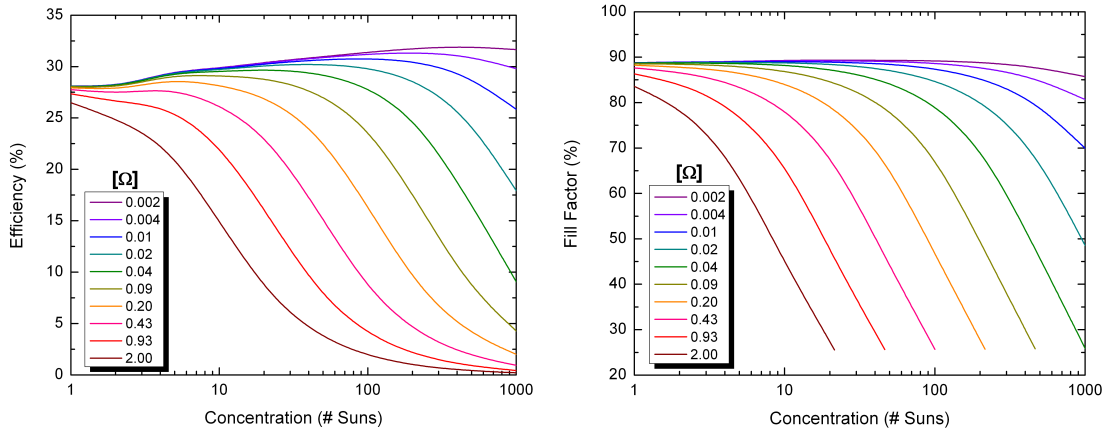

Figure 5.1. Efficiency (left) and Fill Factor (right) as a function of solar concentration factor for multiple series resistance values.

5.1.1. Concentration Measurements

Devices were fabricated as previously discussed with 5, 10 and 20 layers of QDs in the *i*-region, along with a baseline cell. Cells were tested at the NASA Glenn Research Center using a Large Area Pulsed Solar Simulator (LAPSS). This simulator used a variable-distance mount with fixed tungsten flash bulb. The wafer was placed on a chuck mounted on a monorail in the back of the room and a flash bulb was used to calibrate the system to 4 suns shown in Figure 5.2. Calibration is performed by mounting sample at the largest available distance and adjusting bulb current to AM1.5D one sun short-circuit current density. The devices were moved progressively closer (distance *d*) to the flash bulb increasing the effective solar concentration, proportional to $1/d^2$.

Typically, concentration value is calculated using the short circuit current density, as it scales linearly with concentration as shown in equation 5.1.

$$J_{sc}(C) = CJ_{sc}(1) \tag{5.1}$$

However, this can hide J_{sc}-related anomalies such as superlinearity of this relationship due to Auger recombination. Two-photon absorption processes are also expected to follow a superlinear relationship. Therefore a more sophisticated and accurate method is employed here for evaluation of concentration. A view factor is calculated to determine concentration value in an effort to independently characterize short-circuit current as a function of concentration [81]. This method calculates the fraction of the photon-flux exiting the bulb which is entering the surface of the solar cell. Below is the equation (5.2) describing the formulation:

$$F = \frac{1}{\pi A}\int dA \int \frac{\cos\phi' \cos\phi}{s^2} dA' \tag{5.2}$$

in which A is the area of the cell, A' is the area of the arc lamp, s is the distance between the cell and the source, and ϕ and ϕ' are the angles the edges of the cells make to the point source, which are calculated using the distance and cell dimensions. In this manner, all four solar cell parameters can be assumed independent of concentration during the measurement.

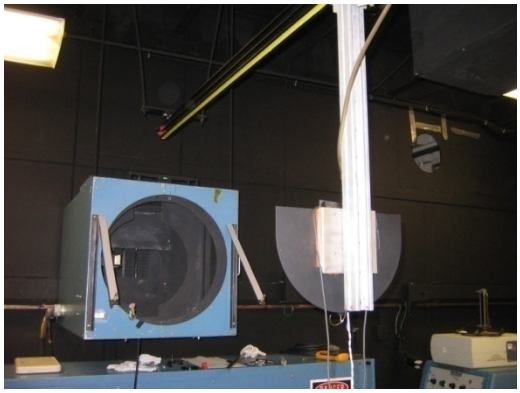

Figure 5.2. Image taken of the monorail-guided sample vacuum-chuck allowing one-dimensional translation towards and away from the flash bulb (back of blue box).

Preliminary results of this data are promising. Although the V_{oc} in Figure 5.3 (left) did not show significant improvement in slope when plotted logarithmically for the QD cells versus the baseline, improvements were seen in the efficiency due to the maintenance of the fill factor at higher concentrations. Peak efficiency increases with QD layer number shown in Figure 5.3 (upper right). Fill factor was observed to peak near 100-200X while efficiency peaked near 400X for most cells. This was consistent with our concentrator cell grid design. The QD enhanced cell gave near 18% power efficiency at 400X. This represented a ~1% absolute efficiency improvement compared to the baseline (6% relative improvement). Under concentrated sunlight, the reduced (longer wavelength) effective bandgap of the QD enhanced solar cell leads to direct improvement

in cell efficiency, since the optimal bandgap shifts to lower energy values with an increase in concentrated sunlight. The enhanced efficiency of the QD cells were a result of the enhanced J_{sc} combined with minimal V_{oc} loss.

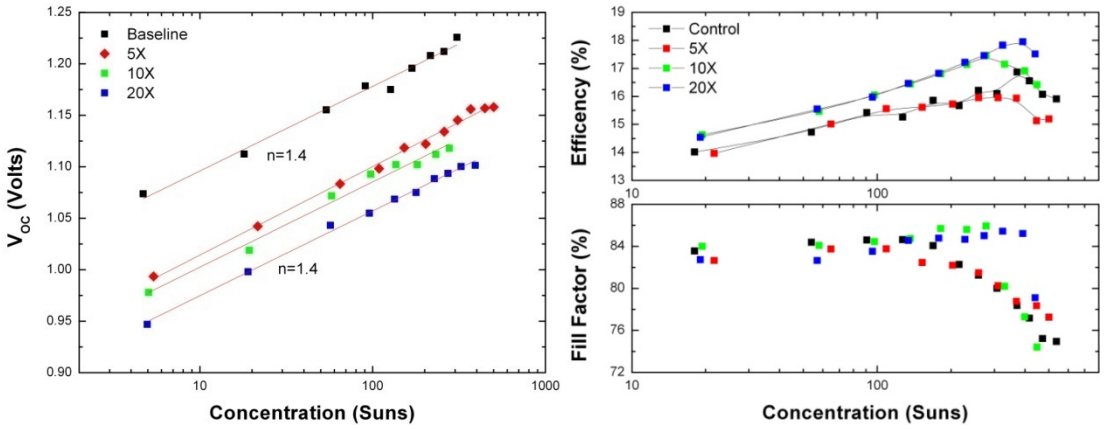

Figure 5.3. Measurements of V_{oc} (left), Efficiency (upper right) and concentration (bottom right) as a function of concentration for baseline, 5x, 10x, 20x QD solar cells.

In addition, the open circuit voltage versus concentration was fit to the following relation derived from the diode equation:

$$V_{oc}(C) = V_{oc}(1) + n\frac{kT}{q}\ln(C) \qquad 5.3$$

where n is the diode ideality factor. As seen in Figure 5.3 (left), all cells shows a good fit to this relation with an extracted ideality near 1.4. This number is indicative of cells operating between the Shockley Reid Hall (SRH) recombination in both the quasi-neutral and depletion regions. The fact that the ideality deviates slightly from 1 may indicate a slightly higher perimeter area recombination related to processing [82]. However, all cells show similar ideality and should be equivalent for comparison purposes.

5.2. Temperature Dependence of QD Cells

The scope of this thesis focuses on the subset of III-V materials which include nanostructured materials for spectrum enhancing and intermediate band effects. For these types of devices, attention must also be given to an additional function besides absorption and collection. Carrier extraction from confined states is a limiting factor of the enhancement these devices can provide. Temperature dependent spectroscopy can be used on devices and test structures including sub-bandgap-absorbing nanostructures.

Additionally, since most applications using concentrated sunlight expose the cells to temperatures much greater than room temperature. Therefore solar cells being evaluated for their operation under concentrated sunlight, it is necessary that temperature-dependent characteristics of the devices are investigated. As seen in previous sections, spectral responsivity measurements can enhance our understanding of the absorption and collection properties of these devices. Here, it was used to evaluate the effects of temperature on the absorption properties of both the bulk and the nanostructure absorption wavelengths.

In Figure 5.4, the temperature dependence of the spectral responsivity of a single junction GaAs cell (a), a single junction GaAs cell with 20 layers (b) and 40 layers (c) of QD is shown. Measurements were made using a Janis cryogenic probestation and cryostat tool coupled with a nitrogen dewar and connected with a Lakeshore Instruments temperature controller. The monochromatic light source was provided by an Optronics Laboratories 750 series spectroradiometer and was directed through the quartz window of the cryostat probestation. Temperature ranged from roughly liquid nitrogen temperature to 410K. As temperature increases, semiconductor band gap decreases. For photovoltaic

devices, this relationship results in an increase in current generation as more of the incoming spectral flux can be absorbed. The absorption bandedge in wavelength space thus moves outward with increasing temperature. All samples clearly showed this effect. In both QD devices, sub-GaAs band gap absorption and collection is observed. At low temperatures, carrier have less available phonon interaction, causing the effective lifetime of minority carriers to decrease. This effect is the suspected cause of decreasing *EQE* at lower temperatures in the low wavelength GaAs bulk absorption region. This effect is more pronounced in the 40x QD embedded device. This is expected to occur for all samples at much lower temperatures less than 100K [83], but an early onset may be occurring due to a reduction in minority carrier lifetime in material with more defects, and higher recombination rates may be present. *EQE* value slightly increases for the identifiable sub GaAs band gap peaks. At these wavelengths, absorption is from wetting layer states 40-100 meV below the GaAs conduction band edge [84]. Qualitatively, these peaks exhibit a similar blue shift with decreasing temperature as that of the bandedge. This suggests that the electron and hole-to-conduction band offsets of the WL state are relatively insensitive to temperature. This QD temperature-dependence is indicative of conduction and valence band offset following a similar temperature-dependence of the absorption energies in comparison with the bulk host bandgap.

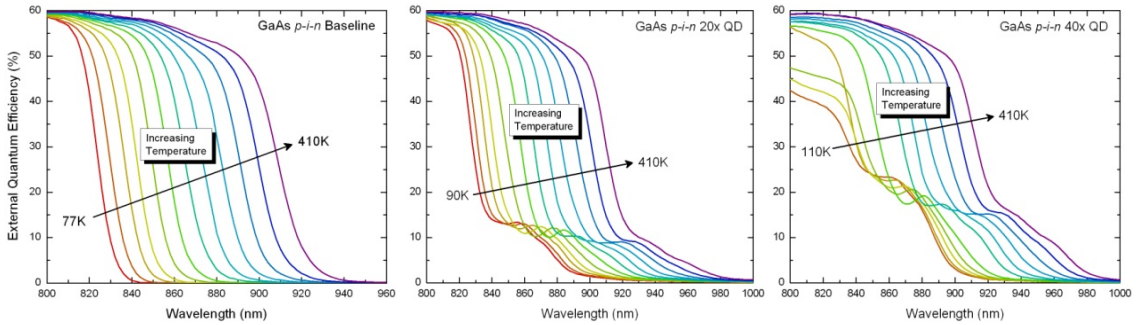

Figure 5.4. Temperature dependent EQE bandage of baseline, 20x and 40x QDSC devices.

A fitting routine was used to de-convolve the spectral responsivity of the three apparent QD peaks and the bulk bandedge for each temperature. Upon fitting an absorption edge function to the host GaAs bandedge, the remaining spectra were fit using three overlapping Lorentzian functions. A Lorentzian distribution was used for this fit in accordance with the distribution of transition energy values present in confined states associated with both the conduction and valence bands. This can be seen for electroluminescence data as an example in Figure 5.13. Since the band offset is relatively temperature insensitive, as temperature increases, the peak responsivity energies of the InAs nanostructures decreases in a trend similar to the expected bandgap versus temperature relationship for GaAs shown in the dotted line in Figure 5.5. This indicates that the bandgap widening affecting the confined states from lattice expansion or contraction, are relatively insignificant in comparison to the confinement effects on these states.

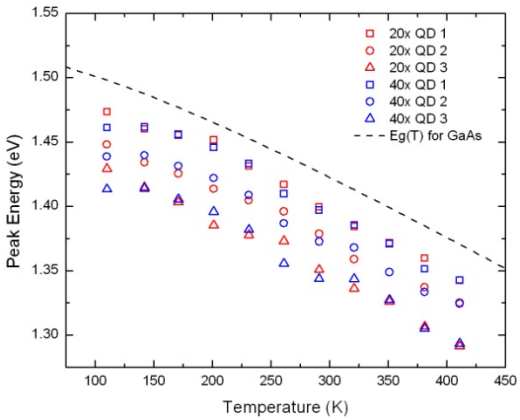

Figure 5.5. Extracted peak energies from EQE of 20x and 40x QDSC plotted with the bandgap vs. temperature relationship.

Also of importance is the temperature dependence of the absorption coefficient which can be directly related to the spectral responsivity through the following relationship:

$$SR = q\int_0^\infty \frac{1}{E}\alpha(E)\left[1-R(E)\right]dE \qquad 5.4$$

Here, $\alpha(E)$ is the energy dependent absorption coefficient and $R(E)$ is the surface reflectivity of the device. Numerical integration of the Lorentzian fits was performed to determine the relative absorption coefficient (spectral responsivity, assuming collection is constant) of the nanostructures as a function of temperature. Figure 5.6 shows the integrated spectral responsivity values as a function of temperature. Here, it is apparent that there is no significant trend with temperature, indicating any increase in apparent absorption intensity shown in Figure 5.4, is merely due to the proximity of the sub-bandgap transition to the bulk bandedge artificially enhancing the QD responsivity through convolution of Fermi-Dirac bandtail states in the bulk. This is a relatively encouraging result, as enhancing the temperature insensitivity of solar cells may be beneficial to those operating under concentration.

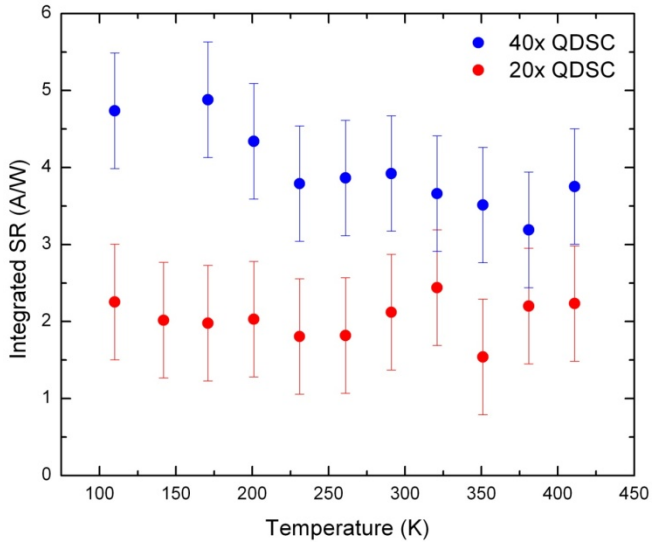

Figure 5.6. Integrated sub-bandgap spectral responsivity versus temperature for 20x and 40x QDSC.

These SR parameters can also be extracted from emission spectra. The inverse process of photovoltaic power generation occurs when the n/p-type region is injected with electrons/holes from a current source, and they are allowed to radiatively recombine emitting an electroluminescence spectrum. In this process, the lowest state in the conduction band provides nearly all of the electrons available for recombination with confinement levels in the valance band. This leads to emission from the lowest hole states transition value. Absorption processes can occur at a number electron states and be extracted. The difference in these two mechanisms can be seen when comparing these two types of spectra and is known commonly as the Stokes' shift.

In Figure 5.7 (left), the emission from a 200mA/cm^2 forward biased 5x QD solar cell sample is shown as a function of temperature. The temperature is varied from 80 to 410K. Three significant peaks can be resolved and assigned to QD states. A fourth peak can be fit and extracted and is in the correct range for a wetting layer emission [84]. Also fit is the bulk GaAs transition emission. All spectra were fit using sum of single

Lorenztian functions for each apparent transition. A general trend can be seen of increasing emission intensity with decreasing temperature. This is due to the same quenching effect of photocurrent allowing an increase in the available carriers for radiative recombination [34, 85, 86]. All five of these peaks' peak energy value is plotted in Figure 5.7 (right) and are fit to the Varshni equation. This is an empirically derived equation with parameters α and β, which are material dependent. The peak energy value for the GaAs bulk peak fits well with the Varshni equation for GaAs ($E_g(0)$ = 1.519 eV, α = 5.41 x 10^{-4} eV/K, β = 204 K). The other four peaks were fit allowing both $E_g(0)$ and α to float. β is assumed to be insignificantly different from bulk GaAs. These peak values are reported and discussed in Table 5.1, below. Included are also the extracted peak values from the spectral responsivity measurements shown in Figure 5.5 for comparison.

Qualitatively, it is observed that there is a relatively insensitive temperature dependence of the QD states. This has been observed elsewhere and is likely attributed to the excitonic nature of the highly confined nanostructures [87]. The emission WL state appears to be much less temperature sensitive than its absorption counterpart. This indicates the possibility of a temperature dependence of the Stokes' shift seen elsewhere in QW embedded devices [88, 89].

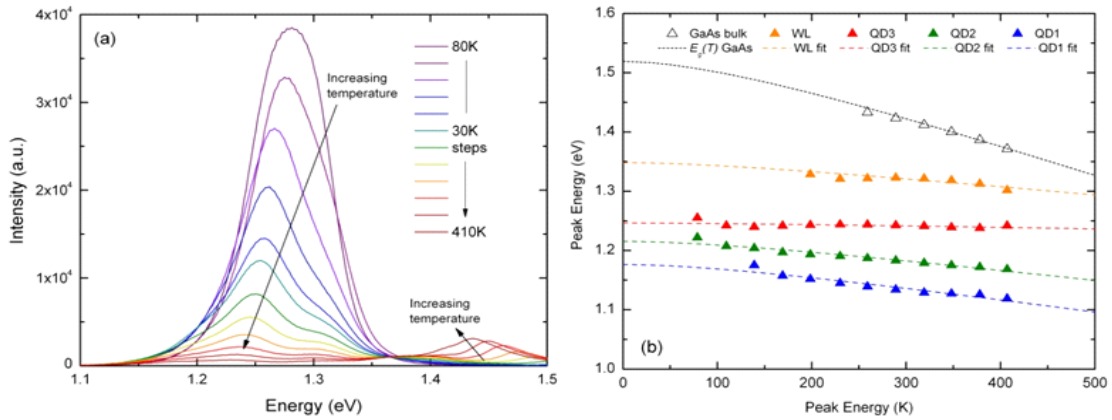

Figure 5.7**.** Left: Electroluminescence spectra of 5x QD solar cell as a function of temperature. Right: GaAs bulk peak value decreases with increasing energy while resolvable sub-GaAs band gap peaks appear less sensitive to temperature.

These trends are much more apparent in Table 5.1. Using the extracted $E_g(0)$ value, the conduction band offset tracks well with temperature for both the 20x and 40x QD samples. By holding β constant and equivalent to GaAs, the α value is allowed to be a fitting parameter. Despite this allowance, very little variation in this value is seen when comparing these WL states to the GaAs bulk. InAs bulk values are very different ($E_g(0)$ = 0.415eV, $\alpha = 2.73\text{x}10^{-4}$, β = 83K) indicating the strength of the temperature dependence of the WL states' relation to that of the bulk material. The emission-derived parameters are much different. The α values are much lower departure of the emission indicating a different temperature dependent nature of these two mechanisms.

Table 5.1. Extracted Varshni parameters $E_g(0)$ and α for 20x and 40x QD samples using *EQE* spectra and 5x QD sample using *EL* spectra, extracted from Figure 5.5 and Figure 5.7 (left).

	Absorption fits (SR data)						Emission fits (EL data)			
	20x QD			40x QD			5x QD			
Parameter	WL1	WL2	WL3	WL1	WL2	WL3	WL	QD1	QD2	QD3
$E_g(0)$ (eV)	1.50	1.47	1.45	1.49	1.47	1.44	1.35	1.18	1.22	1.25
α (10^{-4}eV/K)	5.51	5.22	5.63	5.55	5.32	5.42	1.54	2.26	1.85	2.80

Because of their empirically derived origin, the Varshni parameters are in widespread use and are much more valuable as a comparison tool rather than bearing a meaningful physical significance [90]. The difference in extracted $E_g(0)$ value indicates a very stable slope indicative of the temperature stability seen qualitatively. Interestingly, the wetting layer emission parameters has much different $E_g(0)$ and α values than its absorption process counterpart. This supports the potential for the temperature dependent Stokes' shift mentioned earlier.

5.3. Activation Energy

To investigate the nature of the competitive mechanisms involved in carrier escape and recombination in quantum confined structures, a number of studies have been performed on quantum well devices in which photoluminescence (PL) is performed as a function of temperature [34, 91, 92]. In these studies, an Arrhenius function was fit to the integrated PL signal to determine an activation energy for carrier escape into continuum.

Using this measurement along with the analysis of the emission spectrum both as a function of temperature, extracting information regarding the carrier dynamics of the quantum confined layers can be done. These experiments are performed using the InAs coverage variation samples from Chapter 4, in order to evaluate the effects of the size and density changes have on the activation energies.

In a GaAs matrix, InAs QD structures exhibit confined states below the energy value of the conduction band. Simplifying to a two-state system, the change in carrier population with respect to time (the rate) includes trapping by the QD, U, and anti-trapping to the barrier, $U\beta$. Injected carriers, P, add to the upper state carrier population n. Recombination of carriers from the lower state, m, to the valance band consist of radiative, R and non-radiative, R'. Figure 5.8 illustrates this concept showing all processes that interact with state n and m. Processes that involve electron recombination from m with holes associated with the valance band do not directly affect population of n, but do subtract from that of state m. These recombination events can be seen when they are radiative resulting in the spectra obtained by photoluminescence. Since $U\beta$ follows the exponential function [93], ($\beta \sim e^{-E/kT}$), the population of m will be largely affected by temperature. This population can be probed using techniques like PL, and as the temperature is changed, variations in this population can be monitored.

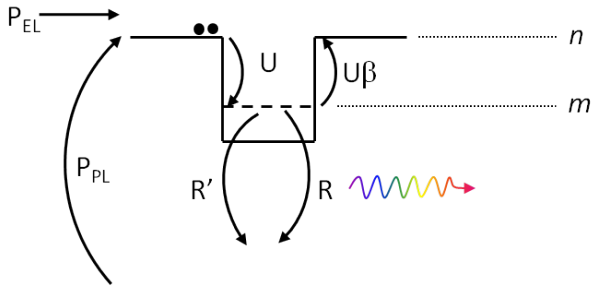

Figure 5.8. Carriers injected into state *n* by either photo- or electroluminescence can be trapped at state *m* and can either recombine or get promoted back to state *n*.

From this process diagram, we can write the following rate equations. For state *n*, we have:

$$0 = \frac{dn}{dt} = P - R'n - Un + Um\beta \qquad 5.5$$

And for state *m*, we have:

$$0 = \frac{dm}{dt} = Un - (U\beta + R)m \qquad 5.6$$

In state *m*, it is clear that there is competition between the thermally promoted carrier and those that recombine to emit luminescence. From this it is possible to obtain the activation energy, E_a, as well as a radiative to non-radiative recombination ratio which will be discussed further.

In an *EQE* measurement, both the photon generation of electron hole pairs, as well as the collection of them, at their respective potential, are evaluated without distinction between them. In order to isolate these two processes, it is important to optically characterize these devices. Photoluminescence measurements allow this, as it is an isolated measurement of the radiative recombination.

For the quantitative investigation of the carrier dynamics, further rearrangement of the rate equations mentioned above, must be made. Solving for the emission intensity I, or Rm, in the variables used, we get:

$$I(T) = \frac{P}{1 + \left(R'/U\right) + \left(R'/R\right)e^{-E_a/kT}} \qquad 5.7$$

Where the ratio R'/R is of importance as an extractable parameter representing the ratio of non-radiative to radiative recombination. Also appearing here is the energy obtained from the β expression. This term, now denoted as E_a, is representative of the activation energy in an Arrhenius relationship. In QWs and QD systems, this often represents the energy barrier seen by a trapped carrier, and is closely related to the difference in energy from the top of the barrier conduction band to the energy state of the carrier. Literature often refers to a simpler 3-parameter equation for the fitting of the integrated intensity variation with temperature. Plotted in Figure 5.9 (left), the data for the 1.82ML InAs coverage sample mentioned in chapter 4 is shown. The fit in Figure 5.9 (right) is using the 3-parameter simplification by the equation shown here:

$$I(T) = \frac{I_0}{1 + Ae^{-E_a/kT}} \qquad 5.8$$

where A is the non-radiative to radiative ratio discussed earlier. I_0 is the amplitude of the intensity and can be divided to the left hand side for normalization.

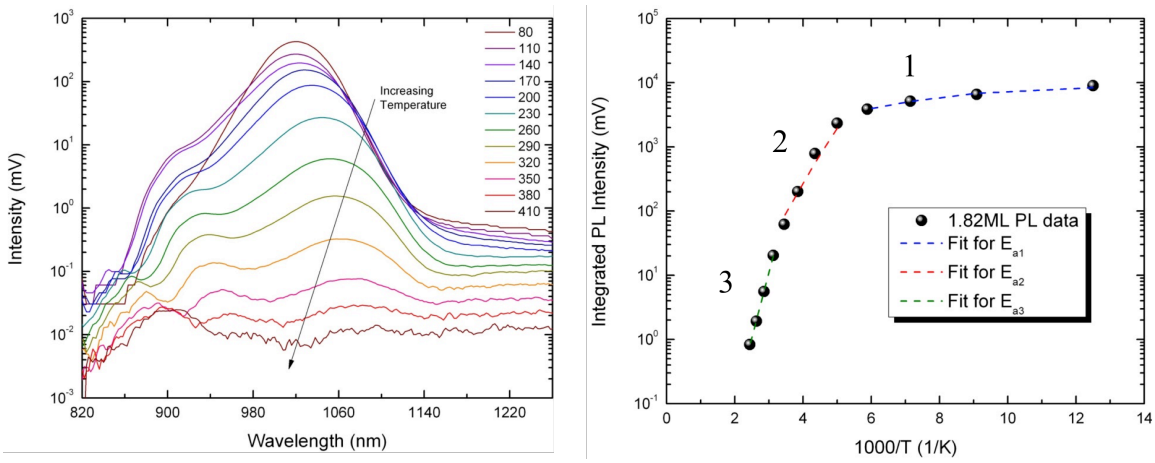

Figure 5.9**.** Left: Temperature dependent photoluminescence spectra of 10x QD test structure. Right: Integrated PL intensity of the sample with the lowest InAs coverage value. Three separate fits indicate three states that carriers are being extracted from.

Figure 5.10 is plotted with the zero value being equated to the conduction band continuum and the values of E_a are plotted below successively. The most obvious feature in Figure 5.10 is that the top most, or closest to the conduction band state decreases with increasing InAs coverage. This correlates with quantum mechanical theory and the state value corresponds with accepted literature value range of the WL state (1.25-1.35 eV) [94]. The two states below suggest QD states at values of roughly 200 and 400meV below the conduction band. These values appear to be relatively insensitive to the varying InAs coverage. In the near-conduction band state, however, this is not true. The effects on the emission of this WL state may indicate that radiative recombination lost to non-radiative recombination in the large, defective QDs is coming primarily from the wetting layers. This is reasonable since the small QDs (and their electrons) are physically separated from the large QDs. This is not so with the wetting layer, as it is a continuous layer. The ratio A, not shown, stays relatively constant for the QD states, but shows a significant shift upwards with increasing Θ in the wetting layer. This indicates that the sample with the lowest number of larger quantum dots and lowest InAs coverage has the

most efficient radiative recombination of all of the samples. This fact also corroborates the data in Figure 5.10, as the wetting layer showed an increase in non-radiative recombination.

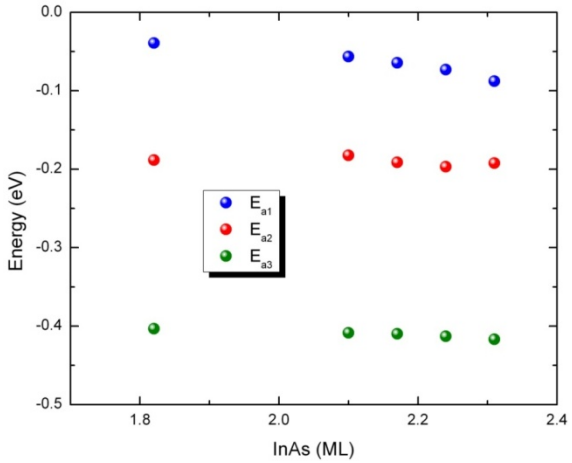

Figure 5.10**.** Extracted activation energy data for QD test structures with varying InAs coverage values.

With the improvement of optical quality and the reduction in non-radiative recombination, quantum efficiency can be improved and higher current values may be available for collection from the QD structures. A further contribution will enhance the benefits of these structures to the over solar energy conversion efficiency. The improved accuracy of the strain compensation associated with a monodisperse QD distribution may also improve the ability to increase the number of these layers available for i-region insertion. This would increase the absorption cross section of the lower-bandgap material, contributing further to the current.

Similar EL measurements were performed on the GaAs and GaAsP strain balancing solar cells discussed in section 3.4. Temperatures were varied from 80K to 295K. Figure 5.11 (left) shows this data and the extraction of activation energies can be seen in Figure 5.11 (right). Two activation energies were extracted for each of these

devices. Relatively little difference in activation energies were seen which is consistent with the assumption that the additional thickness added for GaAsP is negligible, or offset by the reduction in barrier height. The non-radiative to radiative recombination ratios do differ by an order of approximately 3X for the GaP sample indicating a possible increase in non-radiative recombination associated with the decreased accuracy with strain balancing in this sample.

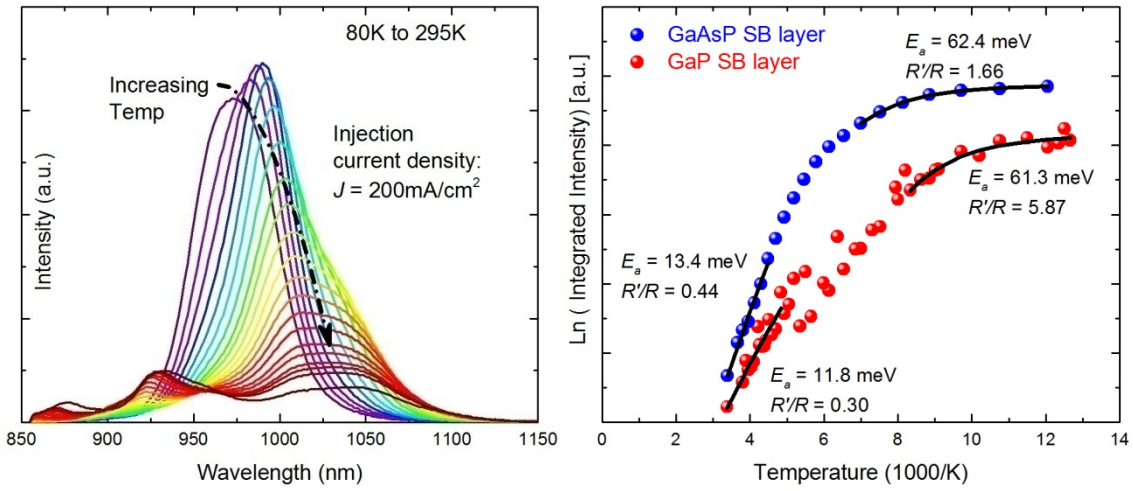

Figure 5.11. Left: Temperature dependent electroluminescence measurements for both GaP and GaAsP type strain balancing layers. Right: Integrated EL intensity versus temperature used to extract activation energies and recombination ratios.

These results further stress the importance of both the InAs coverage value and the sensitivity of strain balancing. At higher InAs coverage, the non-radiative recombination was found to be subtracting from carriers in the WL states, which are key to the current enhancement in these devices. With the improved accuracy of GaAsP strain balancing, the non-radiative recombination ratio drops when compared to the GaP sample. Further characterization of both temperature and voltage would be a desirable next step to more deeply reveal carrier dynamics in these devices.

5.4. Intermediate Band Solar Cell

In 1997, Luque and Marti release their seminal paper entitled, “Increasing the Efficiency of Ideal Solar Cells by Photon Induced Transitions at Intermediate Levels” [26]. In this paper, they introduce the intermediate band solar cell. They derive, using a detailed balance approach, a theoretical efficiency value of a solar cell embedded with an impurity level. They assume transitions not only from the valence band (VB) to the conduction band (CB), but also from the VB to the “Intermediate Band” (IB) and from the IB to the CB. Figure 5.12 outlines the primary photon absorption bands. These transitions can be modeled similarly to the multi-quantum well system due to the sub-baseline-bandgap absorption condition. Their efficiency prediction yields a 63.1% solar cell. At this finding, the novel PV community began seeing increased efforts towards this thrust since the most efficient cell at the time was just below the Shockley-Queisser limit [15] of 31%.

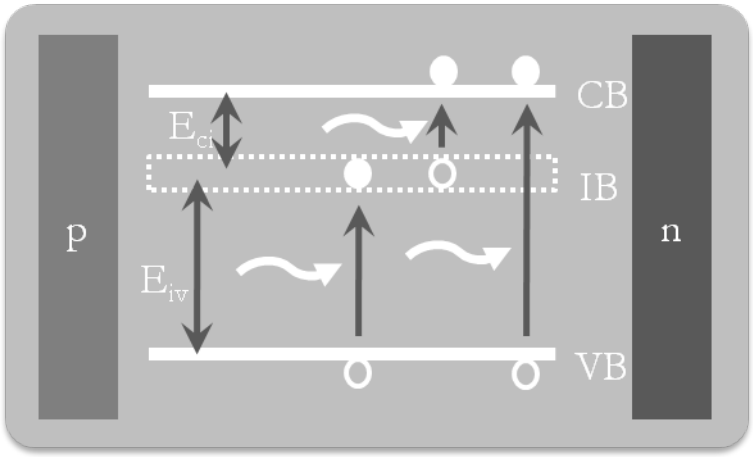

Figure 5.12**.** Operational band diagram for the intermediate band solar cell incorporating 3 distinct bands, providing 3 distinct absorption pathways.

5.4.1. Requirements

The pursuit of the intermediate band solar cell is a more specific, focused use of quantum confined material within a solar cell. This concept's full potential uses very specific assumptions, such as a concentration value of 46,000 suns, no non-radiative recombination, and infinite carrier mobilities [26]. This is meant to be an upper limit calculation, so these are reasonable, but estimates using more practical numbers approach the upper 40%. Also, the thermal isolation between transitions is restricted, as only two supplied photons are the means of operation. One constraint that is realizable is the calculated energy band values for the individual transitions. Their 63% result corresponds to a total host bandgap of 1.93eV, with the intermediate band at 1.23eV from the valence band. Quantum well structures would otherwise be useful for this concept except that the isolation requirement of the intermediate band can only be ideally satisfied by a band with zero-dimensional density of states (Figure 1.1). For this reason, this concept has drawn much attention to solar cells embedded with QDs as the most viable means of realizing such a device [45]. It is these two potential solar technologies that motivate the work done here.

5.4.2. Determination of WF Overlap

In the design of the intermediate band solar cell, it is proposed that there exists the formation of "minibands" within the bandgap of the host embedded with QDs. These are seen in Figure 5.12 as the intermediate band. With thin energy barriers between confined structures, the individual wave functions may overlap significantly enough to widen the energy level to an individual band [44]. Previously, QDs were modeled as QWs in a GaAs matrix, using Silvaco ATLAS device simulator to approximate the wavenumber as

a function of depth through a 1D superlattice [95]. This substitution was justified for modeling the quantum dot samples in this study because of their high aspect ratio (6 x 25 nm, height x diameter). Thus, the energy of a single quantum dot will be dominated by confinement along the growth direction. It was found that with a barrier thickness of 35 ML, there was no significant wavefunction overlap from well to well. This was defined as a system with eigenvalues above 10^{-6} $cm^{-1/2}$ [95]. However, the samples modeled here, with the thinner barriers exhibited significant overlap, $O(10cm^{-1/2})$.

To fully realize these results, epitaxially grown *p-i-n* devices with two sets of QD superlattices (5x and 10x repeat layers) embedded in the *i*-region were designed with varying barrier thicknesses above and below the wavefunction threshold mentioned above. Electroluminescence measurements were taken and analyzed. The peak energies of these samples are compared and trends extracted. Figure 5.13 (left) shows the EL spectra for the 21ML barrier thickness and the de-convolution of the spectrum into fitted Lorentzian functions in order to more accurately extract peak energies. The full-width half-max (FWHM) values are 45-70meV per state. Figure 5.13 (right) shows the transition energy values of the fitted electroluminescence functions for all six samples.

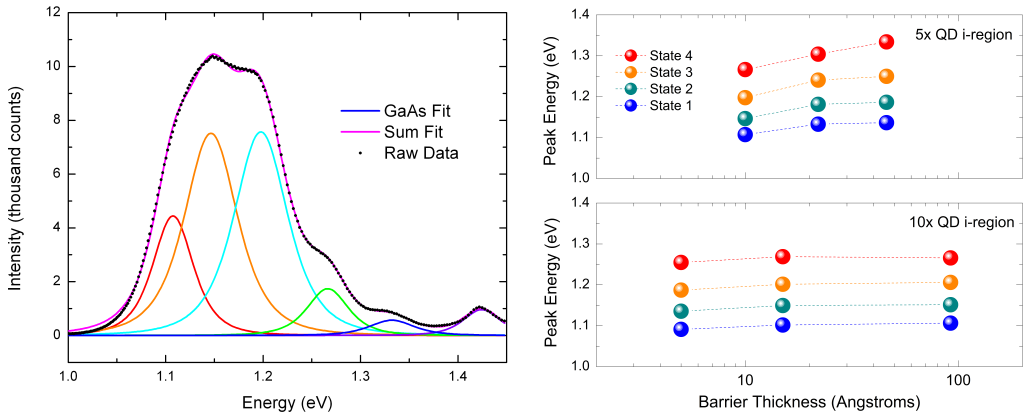

Figure 5.13**.** Left: Lorentzian-deconvolved and fit electroluminescence spectrum of 5x QD sample with 21ML barrier thickness. Right: Peak energies extracted and plotted as function of barrier thickness.

State 1 is represented as the lowest energy transition from the ground state to the first heavy hole [96]. In the 5x QD sample set, progressively decreased energy transition values can be observed in all four states with decreasing barrier thickness (from 43 to 17 ML). Decrease in energy values ranged from 15 meV (state 1) to 60 meV (state 4). This systematic decrease is indicative of less confinement in the QD states as the thickness of the barrier decreases. This effect is indicative of wavefunction overlapping and correlates with data shown in [97]. In order to rule out radiative recombination from multiple size QDs, samples were forward biased at increasing values as shown in Figure 5.14. Here, it is shown that the normalized peak intensity saturates for each of the

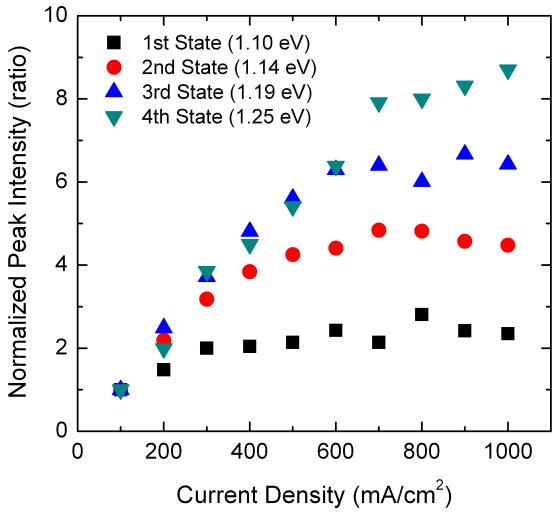

Figure 5.14**.** Normalized peak intensity values as a function of forward injected current density.

states. It is apparent that a single state saturates only after that of the state of lower energy. If the EL-contributing QD size distribution was poly-modal, saturation would not be energy dependent. This systematic saturation can then be assigned to a single QD size. This is confirmed by AFMs shown previously, where the small, optically active QDs are mono-modal in nature, with only inhomogeneous broadening as the geometrical variation.

Further characterization involved a more detailed investigation of the barrier widths using test structures grown at some smaller thicknesses (0.8, 1, 1.2, 1.4, 3, 4, 8, 25 nm) and spreading over a larger range. Figure 5.15 (left) shows the normalized photoluminescence spectra of these samples. Extracting the peak values from these data revealed two separate trends (Figure 5.15, middle). Shown here are the peak energy values as a function of barrier thickness. The trend shown in the three largest thickness samples, is decreasing energy values as the barrier thins. This can be assigned to miniband thinning and has been discussed in literature [98].

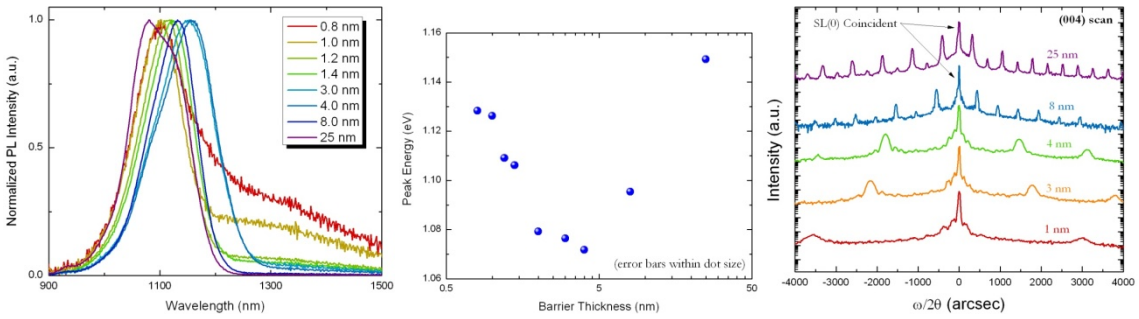

Figure 5.15**.** Left: Normalized photoluminescence spectra; Middle: extracted peak energies from data shown in at left; Right: HRXRD of 5 thickest barrier samples.

The trend shown with the samples with much thinner layers is increasing as the barrier thins. This counters the convention of the three thickest layer samples. There is a reasonable explanation for this, since as these layers become on the order of the QD height (or thinner), there is very little GaAs material to allow for relaxation resulting in large amounts of inhomogeneous strain. In support of this explanation, Figure 5.15 (right) shows the high resolution x-ray diffraction data ([004] 2θ scan) for the five thickest barrier samples. As seen in both the 25 and 8nm samples, the superlattice peaks are very intense indicating high material quality. Strain was relatively minimized, as no deviation from the Bragg peak is noticed in the superlattice peaks. This indicates that the samples are all well strain balanced. This is a reasonable conclusion since the only layer changing thickness here is GaAs. Samples with thinner barriers showed degradation in this aspect, as their SL peaks have decreased in intensity, and FWHM has broadened. This effect is especially significant in the 1nm sample. Data for even thinner samples was not taken as the superlattice peak spacing was beyond a reasonable scan range. These samples are assumed to have followed this trend as the 1nm sample was already roughly an order of magnitude smaller than QD heights.

5.5. Conclusion

As mentioned, QD layer number should be increased and further concentration measurements can be taken to observe the effects of more quantum dot layers on the various solar cell parameters at high concentration values. Short circuit current as a function of concentration is of particular interest because of the expected behavior of a baseline cell and that of a potential intermediate band solar cell. In the intermediate band case, there may be the ability for a two photon absorption process. This manifests in a short circuit current on the square of the concentration. This will typically be very small in magnitude when compared with one-photon processes and therefore has not been observed with low quantum dot number stacks and at lower concentrations. However, if this affect is taking place, it will be more observable at higher QD layer numbers and higher concentration values. Particular attention will be paid to these concepts with future experiments.

Further studies regarding the temperature dependence can be made as well. More recent activation-energy related data has shown an independence of the absorption energy as a function of temperature, contradictory to Figure 5.6 involving the spectral responsivity. This indicates the potential for a temperature dependence of the Stokes' shift and will be investigated in detail using all means of spectroscopy. This has been shown in the literature for quantum well structures [99, 100].

Delta doping QDs has also been accepted as a large requirement of the IB solar cell. The theory being that the intermediate band itself needs to be half filled providing necessary carriers for absorption from IB to CB and VB to IB. One method of testing the efficacy of actual devices with delta doped QDs is to use samples with and without delta

doping and perform photoluminescence experiments at energies lower than the bulk bandgap of GaAs (1.42eV at room temperature). This can be done by using a 980nm HeNe laser (1.26eV). Also, increasing the delta doping value (equivalent to approximate number of carriers per QD), can be used in this experiment to observe the onset of a threshold, above which delta doping may become an effective method for this half-filled condition.

Additionally, further characterization of the tunneling process can be used to evaluate the alternative escape mechanisms to better approximate the probability of the 2^{nd} photon effect as a carrier pathway. To vary the tunneling effects, biasing the solar cells may be possible during the EQE measurement itself. By using a negative or reversed bias, the band structure will bend systematically, and sub-gap EQE can be monitored for any changes as a function of bias. Increasing carrier extraction under further reverse bias can give a dependence of extraction based on tunneling. By normalizing this to the current value at zero bias, one could theoretically extract a ratio of carriers removed purely by tunneling. This, coupled with an increase in extraction under IR light biasing, may be able to give ratios of the effectiveness of all three escape mechanisms.

6. Conclusion & Future Work

This body of work has described in extensive detail the materials science and device physics of InAs QD-embedded superlattice-based *p-i-n* GaAs solar cells. We have seen the importance of strain balancing in light of its effects on structural and optical metrics, as well as its effects on photovoltaic device performance. A large focus of this work also investigated the nature of the role of QDs themselves on material quality and device parameters. An in depth study of optical spectroscopy as well as mechanical stress/strain relations was used to more deeply probe the mechanisms causing performance degradation, and ultimately used to mitigate some of these inherent problems.

Paths forward are outlined here for each of the subtopic chapters in this document. The future work can be divided into two categories. First, the QD arrays can be evaluated from a design standpoint. This not to be confused with the topics covered in chapter 4, as that focuses on the optimal growth conditions. The questions to be answered here are:

- What is the highest achievable QD densities and ranges of sizes to maximize absorption?
- Is there a limitation to this density maximum based on limitations of strain balancing?
- Is there a QD size that best fits the needs of the spectral tuning motivation? IBSC motivation?
- Can we improve the control of the QD growth nucleation?

To begin answering these questions, we can make rough calculations, but also implement experimental pathways. For instance it has been shown that QD densities saturate near $1x10^{11}$ cm^{-2} [17]. An experimental thrust may be necessary here to determine if our current growth conditions will allow this density. The second point may be much more difficult to answer. Clearly there is a dependence of strain balancing on QD density (see section 3.3), but does the surface become too dense with islands that the heterogeneous nature of the strain vectors in the material above the QD become too great to mitigate with a two-dimensional layer? A series of samples (p/n junctions) could be grown here with intentionally varying QD densities, their correct strain balancing layers, and TEM and Electron Beam Induced Current (EBIC) measurements could be made to evaluate defect density.

Nucleation site improvement can be investigated by possibly changing the offcut of the substrate which provides a variation in terrace density. Preliminary results have already been investigated elsewhere in our research group [53, 101]. Further investigation may involve the use of surfactants in the growth chamber such as Sb. Although difficult to implement in a manufacturing environment, investigations on nano-patterning would be of good scientific value for QD nucleation enhancement as well. This has been done elsewhere [102, 103].

The dependence of energy levels on the QD size ensures that tweaking the dot size allows for a direct control of the absorption edge. Further evaluation of this effect can be obtained by combining a detailed balance calculation with a realistic confined-state calculation such as k*p method. This could yield an optimal QD size to target. A more atomistic, energy-minimization-based model may prove to be a viable second order

strain balancing calculation for improving the superlattice structure. Other materials should continue to be evaluated for this balancing layer also, such as GaAsP, evaluated here.

From the cell design standpoint, it will be necessary to gain further advantages with these devices with proper cell design and comparisons to equivalent baseline/control cells. Increasing QD densities and improving the control over nucleation sites would also be valuable. Growth conditions in the InAs layers has proven to be a very sensitive variable in the device performance, and chamber conditions need to be critically assessed with respect to the mitigation of large, optically inactive QDs. Unique spectroscopic measurements may also become very valuable for the evaluation of the IBSC including voltage biased and IR-light biased EQE measurements. Maximizing absorption, absorption volume, and carrier extraction while minimizing material defects in the superlattice and emitter will be the most important efforts to keep focus on as the research continues.

Other ideas for the advancement of these devices include answering the following questions:

- How can we increase absorption per QD layer?
- How can we increase QD density?
- How can we continue to increase number of layers without loss in electric field?
- How can we increase extraction efficiency of QD-generated e-h pairs?
- How can we improve uniformity of QDs to minimize FWHM?
- How can we further reduce i-region recombination?

Some of the answers to these questions lie in calculations. Detailed absorption coefficient formulation can be used to optimize absorption by evaluating the variation in QD morphology prior to implementing it on the reactor. For instance, if absorption coefficient increases with a change in diameter or height theoretically, this can then be a hypothesis going into an experiment.

Ultimately, many of these questions must be answered via experimentation. Changes in chamber pressure have shown to improve dot densities and variation of the injector flows inside the reactor has shown the ability to increase spatial uniformity across wafer [104]. Varying the doping levels in the extrinsic regions of the devices may provide enhanced electric field across the junction. In 1993, Paxman performed this experiment with QW solar cells and found that superlattices placed at ¼ and ¾ of the depth of the *i*-region improved dark current densities in the devices [105]. A similar variation of QD array location within the intrinsic region may also be an approach to maximize the existing electric field.

The improvement of extraction efficiency can be looked at using the tradeoff between the benefits of deep QD states (enhanced spectrum absorption) and the drawbacks (higher thermal energy necessary for extraction) can also be evaluated experimentally. Alternatively, limiting the band offset to only the valence band allows the intensely rich states in this band to provide a 'ladder' effect for an enhanced thermal pathway out to the continuum. This would require choosing materials with iso-conduction band properties and may indicate another use of the Sb source mentioned in the previous section. Since the QD layer itself is the most valuable knob to turn in the spectrum enhancing mechanism of this device type, it will be of great value to these cells

to pursue a meticulous study of the QD growth parameters, with this chapter merely scratching the surface.

Secondly, from a general device design standpoint, the device layer structure may show room for improvement. As the number of QD layers increases, the intensity of the electric field provided by the *i*-region begins to diminish. It may be necessary to increase the emitter and base doping such that the electric field is maintained high. A series of varied doping solar cells could be grown to evaluate the significance of this effect. Another important point to begin to evaluate, as it has been lacking in the solar cells grown to date, is to evaluate the effect of pure *i*-region thickness on the device parameters. This could include growing a series of baseline cells at varying thickness and monitor the short-circuit current, and the ideality factors, as these are the most sensitive to this region of the device. Additionally, it would be an effective test to change the intrinsic region in our "standard baseline" to one which reflects an equivalent *i*-region thickness of our QD-embedded samples. This will further remove asymmetry in experimental evaluations.

By the methods and efforts contained herein, absolute solar cell device efficiency was improved by one half of a percent which can be a significant finding in the photovoltaic field. Although much work is left in inclusion of these nanostructures into real, manufactured devices such as state of the art multijunction III-V cells and also for the realization of an operational intermediate band solar cell, the advancements made here provide a step forward in the direction of these goals to reach fruition. Bandgap engineering can be a viable endeavor in the field of photovoltaic devices.

Appendix A: Strain balance development

Included in this appendix is a detailed development of the application of the continuum elasticity theorem to the strain balancing of a superlattice of two layers which alternate between compressive and tensile about a substrate lattice constant.

In a layer with a cubic lattice psuedomorphically strained to a substrate or thick layer, the energy density is a function of the strained layer's stiffness coefficients (C_{ij}) and the directional components of the strain (ε_{ij}):

$$U = \frac{C_{12}}{2}\left(\varepsilon_{xx}^2 + \varepsilon_{yy}^2 + \varepsilon_{zz}^2\right) + C_{12}\left(\varepsilon_{yy}\varepsilon_{zz} + \varepsilon_{zz}\varepsilon_{xx} + \varepsilon_{xx}\varepsilon_{yy}\right) \quad (1)$$

where the strain, is defined as $\varepsilon_{ij} = [(a_0 - a_1)/ a_1]_{ij}$ for a particular direction, x, y and z. Since ε_{xx} and ε_{yy} are equal as they are strained to the material beneath, and ε_{zz} is defined as $\nu\varepsilon_{xx}$, where ν is the ratio of $-2C_{12}/C_{11}$, this can be reduced to:

$$U = \varepsilon^2\left[C_{11} + C_{12} - \frac{2C_{12}^2}{C_{11}}\right] \quad (1)$$

with $\varepsilon = \varepsilon_{xx} = \varepsilon_{yy}$. Then, taking a thickness weighted average of the energy density for a stack of layers, and substituting A for the factor in the brackets above, we obtain:

$$U_{ave} = \frac{A_1\varepsilon_1^2 t_1 + A_2\varepsilon_2^2 t_2}{t_1 + t_2} \quad (1)$$

This equation can be minimized by taking dU/de and setting equal to zero. Using the definition of ε_{ij}, this minimization of energy density results in a ratio of thicknesses of alternating lattice constants about a_0:

$$t_2 \Big/ t_1 = \frac{A_1 a_1 a_2^2 - A_1 a_2^2 a_0}{A_2 a_1^2 a_0 - A_2 a_2 a_1^2} \quad (1)$$

Assuming t_1 = strained layer (in this case InAs) and t_2 = balancing layer, in this case GaP. It is then the calculation of t_2 that is used for the weighted method described in section 3.2.

Appendix B: Glossary of Abbreviations

Included in this appendix is a listing of common abbreviations used in this thesis.

AFM – Atomic Force Microscopy. Feature height and surface roughness characterization technique which makes use of a highly sensitive cantilever/stylus mechanism. Used in this work for QD diameter, height and distribution density evaluation.

AM*x* – Air Mass number (*x*) used to describe a particular solar spectrum. AM0 is used for solar spectrum used in space, and AM1.5 is used for terrestrial spectra. The air mass number is the daily average of the secant of the angle the sun makes with the horizon. The average is taken using a time weighted average of this value throughout the day.

BSF – Back Surface Field, Layer typically included beneath base layer of a solar cell with slightly higher doping

CET – Continuum Elasticity Theory/Theorem utilized in [68] for the minimization of stress in a superlattice. Called Zero Stress Method (ZSM) in [64].

EL – Electroluminescence. A spectroscopic measurement in which photons emitted from a semiconductor are detected and plotted versus wavelength or energy. It is a very sensitive measurement used to determine energy levels of radiative recombination events and can provide information about radiative lifetime. It is performed by forward biasing a metal-contacted p/n junction and detection is performed using emission from the surface of the material.

EQE – External Quantum Efficiency. This is a measurement of the efficiency of conversion of photons to electron-hole pairs as a function of wavelength. It is a very useful measurement for solar cells as it can indicate performance of the device as a function of doping region.

HRXRD – High Resolution X-Ray Diffraction. This is form of x-ray diffraction in which very small slits are used to guide x-rays into low defect density materials such as single crystal semiconductors. This is a highly sensitive measurement and tool that can be used to extract mechanical and material parameters such as lattice constant, in- and out-of-plane strain, superlattice periodicity, interface quality and alloy composition.

ML – Monolayer. This refers to a material-dependent unit of thickness equal to half of the material's lattice constant.

MOCVD – Metalorganic Chemical Vapor Deposition (also called OMVPE).

QD – Quantum Dot. Typically defined as a three dimensionally confined, zero-dimensional structure with dimensions on the order of or below the Bohr Radius of a material, whose properties are governed by quantum mechanics.

QW – Quantum Well. Defined as a one dimensionally confined, two dimensional material (or layer) with dimensions on the order of or below the Bohr Radius of a material, whose properties are governed by quantum mechanics.

PL – Photoluminescence. Similar to electroluminescence, this is a spectroscopic measurement in which photons emitted from a semiconductor are detected and plotted versus wavelength or energy. It is a very sensitive measurement used to determine energy levels of radiative recombination events and can provide information about radiative lifetime. It is performed by probing a test structure or device using a laser at a wavelength whose energy is larger than the detection energy range, and detection is performed using emission from the surface of the material.

WL – Wetting Layer. This layer is an extremely thin (on the order of a ML that forms during QD growth and is left "behind" after QD nucleation is complete.

References

[1] A. Zervos, C. Lins, and J. Muth, "Re-thinking 2050: A 100% Renewable Energy Vision for the European Union," Brussels, Belgium2010.

[2] A. Jager-Waldau, "PV Status Report 2011: Research, Solar Cell Production and Market Implementation of Photovoltaics," Institute for Energy, Renewable Energy Unit, Via Enrico Fermi 2749; TP 450 I - 21027 Ispra (VA), Italia, Luxembourg2011.

[3] G. G. a. W. Doeztel, *Introduction to Microsystems Technology: A Guide for Students*. Chichester, England: J. Wiley & Sons, 2008.

[4] "$1/W Photovoltaic Systems," U. S. D. o. Energy, Ed., ed: Advanced Research Projects Agency - Energy, 2009.

[5] M. W. Wanlass, S. P. Ahrenkiel, R. K. Ahrenkiel, D. S. Albin, J. J. Carapella, A. Duda, J. F. Geisz, S. Kurtz, T. Moriarty, R. J. Wehrer, and B. Wernsman, "Lattice-mismatched approaches for high-performance, III-V photovoltaic energy converters," in *31st Photovoltaic Specialists Conference*, Orlando, FL, 2005, pp. 530-535.

[6] A. J. Nozik, "Spectroscopy and hot electron relaxation dynamics in semiconductor quantum wells and quantum dots," *Annul. Rev. Phys. Chem.,* vol. 52, pp. 193-231, 2001.

[7] R. D. Schaller and V. I. Klimov, "High efficiency carrier multiplication in PbSe nanocrystals: Implications for solar energy conversion," *Phys. Rev. Lett.,* vol. 92, 2004.

[8] R. J. Ellingson, M. C. Beard, J. C. Johnson, P. Yu, O. I. Micic, A. J. Nozik, A. Shabaev, and A. L. Efros, "Highly efficient multiple exciton generation in colloidal PbSe and PbS quantum dots," *Nano Lett.,* vol. 5, pp. 865-871, 2005.

[9] A. J. Nozik, "Exciton multiplication and relaxation dynamics in quantum dots: Applications to ultrahigh-efficiency solar photon conversion," *Inorg. Chem.,* vol. 44, pp. 6893-6899, 2005.

[10] S. M. Hubbard, C. D. Cress, C. G. Bailey, R. P. Raffaelle, S. G. Bailey, and D. M. Wilt, "Effect of strain compensation on quantum dot enhanced GaAs solar cells " *Appl. Phys. Lett.,* vol. 92, 2008.

[11] K. W. J. Barnham, B. Braun, J. Nelson, M. Paxman, C. Button, J. S. Roberts, and C. T. Foxon, "Short-circuit current and energy efficiency enhancement in low-dimensional structure photovoltaic device.," *Appl. Phys. Lett.,* vol. 59, pp. 135-137, 1991.

[12] R. B. Laghumavarapu, M. El-Emawy, N. Nuntawong, A. Moscho, L. F. Lester, and D. L. Huffaker, "Improved device performance of InAs/GaAs quantum dot solar cells with GaP strain compensation layers," *Appl. Phys. Lett.,* vol. 91, 2007.

[13] R. P. Raffaelle, S. Sinharoy, J. D. Andersen, D. M. Wilt, and S. G. Bailey, "Multi-junction solar cell spectral tuning with quantum dots," in *World Conference on Photovoltaic Energy Conversion*, Waikoloa, Hawaii, 2006, pp. 162-166.

[14] P. T. Landsberg and G. Tonge, "Thermodynamic energy conversion efficiencies," *Journal of Applied Physics,* vol. 51, 1980.

[15] W. Shockley and H. J. Queisser, "Detailed balance limit of efficiency of p-n junction solar cells," *J. Appl. Phys.,* vol. 32, pp. 510-519, 1961.

[16] G. L. Araujo and A. Marti, "Absolute limiting efficiencies for photovoltaic energy conversion," *Sol. Ener. Mat. and Sol. Cel.,* vol. 33, 1994.

[17] D. Bimberg, M. Grundmann, and N. N. Ledentsov, *Quantum Dot Heterostructures*. New York: John Wiley & Sons, 1999.

[18] I. N. Stranski and L. Krastinow, in *Proceedings of the Meeting of the Academy of Sciences*, Vienna, Austria, 1937, p. 797.

[19] L. Goldstein, F. Glas, J. Y. Marzin, M. N. Charasse, and G. L. Roux, "Growth by molecular beam epitaxy and characterization of InAs/GaAs strained-layer superlattices," *Appl. Phys. Lett.,* vol. 47, 1985.

[20] N. Kristaeder, N. N. Ledentsov, M. Grundmann, D. Bimberg, V. M. Ustinov, S. S. Ruvinov, M. V. Maximov, P. S. Kop'ev, Z. I. Alferov, U. Richter, P. Werner, U. Gosele, and J. Heidenreich, "Low threshold, large T0 injection laser emission from (InGa)As quantum dots," *Elec. Lett.,* vol. 30, 1994.

[21] R. Mirin, A. Gossard, and J. Bowers, "Room temperature lasing from InGaAs quantum dots," *Elec. Lett.,* vol. 32, 1996.

[22] K. W. Berryman, S. A. Lyon, and M. Segev, "Mid-infrared photoconductivity in InAs quantum dots," *Appl. Phys. Lett.,* vol. 70, 1997.

[23] J. Phillips, K. Kamath, and P. Bhattacharya, "Far-infrared photoconductivity in self organized InAs quantum dots," *Appl. Phys. Lett.,* vol. 72, 1998.

[24] K. W. J. Barnham and G. Duggan, "A new approach to high-efficiency multi-band-gap solar cells," *J. Appl. Phys.,* vol. 67, pp. 3490-3493, 1990.

[25] A. Marti, L. Cuadra, and A. Luque, "Quantum dot intermediate band solar cell," in *28th Photovoltaic Specialists Conference*, Anchorage, AL, 2000.

[26] A. Luque and A. Marti, "Increasing the efficiency of ideal solar cells by photon induced transitions at intermediate levels," *Phys. Rev. Lett.,* vol. 78, pp. 5014-5017, 1997.

[27] A. G. Norman, M. C. Hanna, P. Dippo, D. H. Levi, R. C. Reedy, J. S. Ward, and M. M. Al-Jassim, "InGaAs/GaAs QD Superlattices: MOVPE Growth, Structural and Optical Characterization, and Application in Intermediate-Band Solar Cells," in *31st Photovoltaic Specialists Conference*, Lake Buena Vista, FL, 2005.

[28] S. Chakrabarti, S. Adhikary, N. Halder, Y. Aytac, and A. G. U. Perera, "High-performance, long-wave (~10.2 um) InGaAs/GaAs quantum dot infrared

photodetector with quaternary In0.21Al0.21Ga0.58As capping," *Appl. Phys. Lett.,* vol. 99, 2011.

[29] S. I. Molina, A. M. Beltran, T. Ben, P. L. Galindo, E. Guerrero, A. G. Taboada, J. M. Ripalda, and M. F. Chisholm, "High resolution electron microscopy of GaAs capped GaSb nanostructures," *Appl. Phys. Lett.,* vol. 94, 2009.

[30] Y. V. Terent'ev, O. G. Lyublinskaya, A. A. Toropov, B. Y. Meltser, A. N. Semenov, V. A. Solov'ev, and S. V. Ivanov, "Anomalous spin splitting of electrons in type-II InSb quantum dots in InAs," *Semiconductors,* vol. 43, 2009.

[31] D. Kim, W. Sheng, P. J. Poole, D. Dalacu, J. Lefebvre, J. Lapointe, M. E. Reimer, G. C. Aers, and R. L. Williams, "Tuning the exciton g factor in single InAs/InP quantum dots," *Phys. Rev. B,* vol. 79, 2009.

[32] J. McCaffrey, M. Robertson, P. Poole, Z. Wasilewski, B. Riel, R. WIlliams, and S. Fafard, "Structural Characterization of InAs/GaAs and InAs/InP Quantum Dots by Transmission Electron Microscopy," in *Materials Research Society Symposium*, 2010, pp. J851-J8510.

[33] A. Alemu, J. A. H. Coaquira, and A. Freundlich, "Dependence of device performance on carrier escape sequence in multi-quantum-well *p-i-n* solar cells," *J. Appl. Phys.,* vol. 99, p. 4506, 2006.

[34] J. R. Botha and A. W. R. Leitch, "Temperature dependence of the photoluminescence properties and band gap energy of InxGa1–xAs/GaAs quantum wells," *Journal of Electronic Materials,* vol. 29, 2000.

[35] C. G. Bailey, S. M. Hubbard, D. V. Forbes, R. F. Aguinaldo, C. D. Cress, S. J. Polly, and R. P. Raffaelle, "Effect of barrier thickness on strain balanced InAs/GaAs QD solar cells," in *34th Photovoltaic Specialist Conference*, Philadelphia, PA, 2009.

[36] D. Guimard, R. Morihara, D. Bordel, K. Tanabe, Y. Wakayama, M. Nishioka, and Y. Arakawa, "Fabrication of InAs/GaAs quantum dot solar cells with enhanced

photocurrent and without degradation of open circuit voltage," *Appl. Phys. Lett.,* vol. 96, 2010.

[37] C. G. Bailey, S. J. Polly, J. Okvath, D. V. Forbes, C. D. Cress, S. M. Hubbard, and R. P. Raffaelle, "Temperature dependent photoluminescence spectroscopy of InAs/GaAs solar cells," in *35th Photovoltaic Specialists Conference*, Honolulu, HI, 2010.

[38] C. G. Bailey, D. V. Forbes, R. P. Raffaelle, and S. M. Hubbard, "Near 1V open circuit voltage InAs/GaAs quantum dot solar cells," *Appl. Phys. Lett.,* vol. 98, 2011.

[39] M. Wiemer, V. Sabnis, and H. Yuen, "43.5% efficient lattice matched solar cells," in *High and Low Concentrator Systems for Solar Electric Applications VI*, San Diego, California, USA 2011, p. 810804.

[40] J. Singh, *Physics of semiconductors and their heterostructures*: McGraw-Hill, 1993.

[41] E. F. Schubert, *Light Emitting Diodes*: Cambridge University Press, 2006.

[42] K. W. J. Barnham, I. Ballard, J. Barnes, J. Connolly, P. Griffin, B. Kluftinger, J. Nelson, E. Tsui, and A. Zachariou, "Quantum well solar cells," *Appl. Surf. Sci.,* vol. 113/114, pp. 722-733, 1997.

[43] N. J. Ekins-Daukes, K. W. J. Barnham, J. P. Connolly, J. S. Roberts, J. C. Clark, G. Hill, and M. Mazzer, "Strain-balanced GaAsP/InGaAs quantum well solar cells," *Appl. Phys. Lett.,* vol. 75, pp. 4195-4197, 1999.

[44] A. Luque and A. Marti, "The intermediate band solar cell: Progress towards the realization of an attractive concept," *Advanced Materials,* vol. 22, pp. 160-174, 2010.

[45] A. Luque, P. G. Linares, E. Antolin, E. Canovas, C. D. Farmer, C. R. Stanley, and A. Marti, "Multiple levels in intermediate band solar cells," *Appl. Phys. Lett.,* vol. 96, 2010.

[46] S. M. Sze, *Physics of Semiconductor Devices*. New York: Wiley-Interscience, 1981.

[47] R. Williams, *Modern GaAs processing techniques*. Norwood, MA: Artech House, 1990.

[48] G. B. Stringfellow, *Organometallic vapor-phase epitaxy: theory and practice*: Academic Press, 1989.

[49] S. Adachi, *Properties of Semiconductor Alloys: Group-IV, III-V and II-VI Semiconductors*: Wiley, 2009.

[50] I. N. Stranski and L. Krastinow, in *Proceedings of the Meeting of the Academy of Sciences in Vienna*, 1937, p. 797.

[51] R. V. Kukta and L. B. Freund, "Minimium energy configuration of epitaxial material clusters on a lattice-mismatched substrate," *J. Mech. & Phys. Solids,* vol. 45, 1997.

[52] V. P. Evtikhiev, A. M. Boiko, I. V. Kudryashov, A. K. Kryganovskii, R. A. Suris, A. N. Titkov, and V. E. Tokranov, "Control of density, size and size uniformity of MBE-grown InAs quantum dots by means of substrate misorientation," *Semicon. Sci. and Tech,,* vol. 17, pp. 545-550, 2002.

[53] C. R. Mackos, D. V. Forbes, S. J. Polly, A. Podell, Y. Dai, C. G. Bailey, and S. M. Hubbard, "GaAs Substrate Misorientation and the Effect on InAs Quantum Dot Critical Thickness," in *37th IEEE Photovoltaic Specialists Conference*, Seattle, WA, 2011.

[54] J. Kim, C. Yang, U. Sim, G.-D. Lee, J. Park, Y. Lee, and E. Yoon, "Growth mechanism of highly uniform InAs/GaAs quantum dot with periodic arsine interruption by metalorganic chemical vapor deposition," *J. Appl. Phys.,* vol. 110, 2011.

[55] M. Yang, S. J. Xu, and J. Wang, "Influence of capping layer and atomic interdiffusion on the strain distribution in single and double self-assembled InAs/GaAs quantum dots," *Appl. Phys. Lett.,* vol. 92, p. 3112, 2008.

[56] J. Nelson, *The physics of solar cells*. London: Imperial College Press, 2003.

[57] B. S. Passmore, J.Wu, E. A. D. Jr., O. Manasreh, P. M. Lytvyn, V. P. Kunets, and G. J. Salamo, "Multi-color photoresponse based on interband and intersubband transitions in InAs and InGaAs quantum dot photodetectors," in *Fall meeting of the Materials Research Society*, Boston, MA, 2008.

[58] S. Tsao, H. Lim, H. Seo, W. Zhang, and M. Razeghi, "InP-based quantum dot infrared photodetectors with high quantum efficiency and high-temperature imaging," *IEEE Sensors Journal,* vol. 8, pp. 936-941, 2008.

[59] J. W. Matthews and A. E. Blakeslee, "Defects in epitaxial multilayers," *J. Crystal Growth,* vol. 27, pp. 118-125, 1974.

[60] P. S. Zory, Ed., *Quantum Well Lasers*. San Diego: Academic Press, 1993, p.^pp. Pages.

[61] F. Liu, S. E. Davenport, H. M. Evans, and M. G. Lagally, "Self-Organization of 3D coherent island size and shape in multilayer heteroepitaxial films," *Phys. Rev. Lett.,* vol. 82, 1999.

[62] H. Hamada, R. Hiroyama, S. Honda, M. Shono, K. Yodoshi, and T. Yamaguchi, "AlGaInP strained multiple-quantum-well visible laser diodes (λL⩽630 nm band) with a multiquantum barrier grown on misoriented substrates," *Journ. of Quan. Elec.,* vol. 29, 1993.

[63] L. Diehl, S. Mentese, H. Sigg, E. MÜller, D. GrÜtzmacher, U. Gennser, I. Sagnes, T. Fromherz, J. Stangl, T. Rochl, G. Bauer, Y. Campidelli, O. Kermarrec, D. Bensahel, and J. Faist, "Strain Compensated Si/Sige Quantum Cascade Emitters Grown On Sige Pseudosubstrates," *Chemistry and Materials Science,* vol. 93, pp. 325-330, 2003.

[64] N. J. Ekins-Daukes, "Strain-balanced criteria for multiple quantum well structures and its signiture in X-ray rocking curves," *Crystal Growth & Design,* vol. 2, pp. 287-292, 2002.

[65] V. Popescu, G. Bester, M. C. Hanna, A. G. Norman, and A. Zunger, "Theoretical and experimental examination of the intermediate-band concept for strain-balanced (In,Ga)As/Ga(As,P) quantum dot solar cells," *Phys. Rev. B,* vol. 78, p. 5321, 2008.

[66] C. G. Bailey, S. M. Hubbard, D. V. Forbes, and R. P. Raffaelle, "Evaluation of strain balancing layer thickness for InAs/GaAs quantum dot arrays using high resolution x-ray diffraction and photoluminescence," *Appl. Phys. Lett.,* vol. 95, p. 3110, 2009.

[67] Y. Okada, R. Oshima, and A. Takata, "Characteristics of InAs/GaNAs strain-compensated quantum dot solar cell," *J. Appl. Phys.,* vol. 106, 2009.

[68] V. Popescu, G. Bester, M. C. Hanna, A. G. Norman, and A. Zunger, "Theoretical and experimental examination of the intermediate-band concept for strain-balanced (In,Ga)As/Ga(As,P) quantum dot solar cells," *Phys. Rev. B,* vol. 78, 2008.

[69] J. Nelson, *The physics of solar cells*. London: Imperial College Press, 2003.

[70] S. Tomic, A. G. Sunderland, and I. J. Bush, "Parallel multi-band k·p code for electronic structure of zinc blend semiconductor quantum dots," *J. of Mat.Chem.,* 2006.

[71] S. Kret, P. Ruterana, A. Rosenauer, and D. Gerthsen, "Extracting Quantitative Information from High Resolution Electron Microscopy," *Physica Status Solidi B,* vol. 227, 2001.

[72] S. M. Hubbard, D. Wilt, S. Bailey, D. Byrnes, and R. Raffaelle, "OMVPE grown InAs quantum dots for application in nanostructured photovoltaics," in *World Conference on Photovoltaic Energy Conversion*, Waikoloa, HI 2006, pp. 118-121.

[73] G. S. Solomon, J. A. Trezza, and J. S. Harris, "Effects of monolayer coverage, flux ratio, and growth rate on the island density of InAs islands on GaAs," *Appl. Phys. Lett.,* vol. 66, 1995.

[74] F. Heinrichsdorff, A. Krost, M. Grundmann, D. Bimberg, F. Bertram, J. Christen, A. Kosogov, and P. Werner, "Self organization phenomena of InGaAs/GaAs quantum dots grown by metalorganic chemical vapour deposition," *Journal of Crystal Growth,* vol. 170, 1997.

[75] T. S. Yeoh, C. P. Liu, R. B. Swint, A. E. Huber, S. D. Roh, C. Y. Woo, K. E. Lee, and J. J. Coleman, "Epitaxy of InAs quantum dots on self-organized two-dimensional InAs

islands by atmospheric pressure metalorganic chemical vapor deposition," *Appl. Phys. Lett.,* vol. 79, 2001.

[76] P. Frigeri, L. Nasi, M. Prezioso, L. Seravalli, G. Trevisi, E. Gombia, R. Mosca, F. Germini, C. Bocchi, and S. Franchi, "Effects of the quantum dot ripening in high-coverage InAs/GaAs nanostructures," *J. Appl. Phys.,* vol. 102, 2007.

[77] S. M. Hubbard, C. G. Bailey, S. J. Polly, C. D. Cress, J. D. Andersen, D. V. Forbes, and R. P. Raffaelle, "Nanostructured photovoltaics for space power," *J. Nano. Photon.,* vol. 3, 2009.

[78] S. M. Hubbard, C. Plourde, Z. Bittner, C. G. Bailey, M. Harris, T. Bald, M. Bennett, D. V. Forbes, and R. P. Raffaelle, "InAs quantum dot enhancement of GaAs solar cells," in *Photovoltaic Specialists Conference*, Honolulu, HI, 2010, pp. 001217-001222.

[79] R. P. Raffaelle, C. G. Bailey, S. M. Hubbard, S. J. Polly, and D. V. Forbes, "Quantum Dot Spectral Tuning of Multijunction III-V Solar Cells " in *Fall Meeting of the MRS*, Boston, MA, 2008.

[80] S. M. Hubbard, C. G. Bailey, R. Aguinaldo, S. J. Polly, D. V. Forbes, and R. P. Raffaelle, "Characterization of quantum dot enhanced solar cells for concentrator photovoltaics," in *34th Photovoltaic Specialists Conference*, Philadelphia, PA, 2009.

[81] D. Scheiman, B. L. Sater, D. Chubb, and P. Jenkins, "Measurement and Characterization of Concentrator Solar Cells," in *3rd World Conference on Photovoltaic Energy Conversion*, Osaka, Japan, 2003, pp. 885-888.

[82] S. J. Polly, M. L. Harris, Z. Bittner, C. R. Plourde, C. G. Bailey, D. V. Forbes, and S. M. Hubbard, "Effect of cell size on GaAs concentrators with InAs quantum dots," in *35th Photovoltaic Specialists Conference*, Honolulu, HI, 2010, pp. 2057-2061.

[83] J. Barnes, E. Tsui, and K. Barnham, "Steady state photocurrent and photoluminescence from single quantum wells as a function of temperature and bias," *J. Appl. Phys.,* vol. 81, 1997.

[84] G. Rowland, T. Hosea, S. Malik, D. Childs, and R. Murray, "A photomodulated reflectance study of InAs/GaAs self-assembled quantum dots," *Appl. Phys. Lett.,* vol. 73, 1998.

[85] Y. T. Dai, J. C. Fan, Y. F. Chen, R. M. Lin, S. C. Lee, and H. H. Lin, "Temperature dependence of photoluminescence spectra in InAs/GaAs quantum dot superlattices with large thicknesses," *J. Appl. Phys.,* vol. 82, pp. 4489-4492, 1997.

[86] L. Kong, Z. C. Feng, Z. Wu, and W. Lu, "Temperature depedent and time-resolved photoluminescence stuides of InAs self-assembled quantum dots with InGaAs strain reducing layer structure," *Journal of Applied Physics,* vol. 106, 2009.

[87] O. Kojima, H. Nakatani, T. Kita, O. Wada, and K. Akahane, "Temperature dependence of photoluminescence characteristics of excitons in stacked quantum dots and quantum dot chains," *J. Appl. Phys.,* vol. 107, 2010.

[88] C. Sasaki, H. Naito, M. Iwata, H. Kudo, Y. Yamada, T. Taguchi, T. Jyouichi, H. Okagawa, K. Tadatomo, and H. Tanaka, "Temperature dependence of Stokes shift in InxGa1-xN epitaxial layers," *J. Appl. Phys.,* vol. 93, 2003.

[89] D. Hang, M. Chou, M. Hsieh, and M. Heuken, "Temperature dependence of the Stokes shift in tensile InGaN/GaN MQWs with advanced buffer layers," *Journal of Korean Physical Society,* vol. 53, pp. 1584-1588, 2008.

[90] I. Vainshtein, A. Zatsepin, and V. Kortov, "Applicability of the empirical Varshni relation for the temperature dependence of the width of the band gap," *Phys. Sol. State,* vol. 41, pp. 905-908, 1999.

[91] A. Alemu, L. Bhusal, and A. Freundlich, "Improved performance due to fast electronic escape in MQW p-i-n solar cells," in *31st Photovoltaic Specialists Conference*, Lake Beuna Vista, FL, 2005.

[92] J. S. Hwang, M. F. Chen, K. I. Lin, C. N. Tsai, W. C. Hwang, W. Y. Chou, H. H. Lin, and M. C. Chen, "Study of Self-Organized InAs/GaAs Quantum Dots by Photoluminescence and Photoreflectance," *Jpn. J. Appl. Phys. ,* vol. 42, 2003.

[93] S. Martini, A. A. Quivy, A. Tabata, and J. R. Leite, "Influence of the temperature and excitation power on the optical properties of InGaAs/GaAs quantum wells grown on vicinal GaAs(001) surfaces," *J. Appl. Phys.,* vol. 90, 2001.

[94] J. Gardner, E. Albers, C. G. Bailey, S. M. Hubbard, and R. P. Raffaelle, "Advanced techniques for the characterization of quantum dot enhanced solar cells," in *Photovoltaic Specialists Conference*, Philadelphia, PA, 2009.

[95] R. F. Aguinaldo, "Modeling solutions and simulations for advanced III-V photovoltaics based on nanostructures," M.S. Thesis, , Rochester Institute of Technology, Rochester, NY, 2008.

[96] J. G. J. Adams, J. S. Roberts, G. Hill, N. J. Ekins-Daukes, and K. W. J. Barnham, in *34th Photovoltaic Specialists Conference*, Philadelphia, PA, 2009.

[97] N. N. Ledentsov, V. A. Shchukin, M. Grundmann, N. Kirstaedter, J. Boehrer, O. Schmidt, D. Bimberg, V. M. Ustinov, A. Y. Egorov, A. E. Zhukov, P. S. Kop'ev, S. V. Zaitsev, N. Y. Gordeev, Z. I. Alferov, A. I. Borovkov, A. O. Kosogov, S. S. Ruvimov, P. Werner, U. Goesele, and J. Heydenreich, "Direct formation of vertically coupled quantum dots in Stranski-Krastinow growth," *Phys. Rev. B,* vol. 54, pp. 8743-8750, 1996.

[98] S. Tomic, T. S. Jones, and N. M. Harrison, "Absorption characteristics of a quantum dot array induced intermediate band: Implications for solar cell design," *Appl. Phys. Lett.,* vol. 93, 2008.

[99] D. R. Hang, M. M. C. Chou, M. H. Hsieh, and M. Heuken, "Temperature dependence of the Stokes shift in tensile InGaN/GaN MQWs with advanced buffer layers," *Journal of the Korean Physical Society,* vol. 53, pp. 1584-1588, 2008.

[100] C. Sasaki, H. Naito, M. Iwata, H. Kudo, Y. Yamada, T. Taguchi, T. Jyouichi, H. Okagawa, K. Tadatomo, and H. Tanaka, "Temperature dependence of Stokes shift in $In_xGa_{1-x}N$ epitaxial layers," *J. Appl. Phys.,* vol. 93, pp. 1642-1646, 2003.

[101] D. V. Forbes, C. G. Bailey, S. J. Polly, C. R. Plourde, S. M. Hubbard, and R. P. Raffaelle, "Substrate Orientation Effects on QD-Strain Compensated GaAs Solar Cells," in *IEEE Photovoltaic Specialists Conference*, Honolulu, HI, 2010.

[102] J. Kim, M. Kawabe, and N. Koguchi, "Ordering of high-quality InAs quantum dots on defect-free nanoholes," *Appl. Phys. Lett.,* vol. 88, 2006.

[103] J. Martın-Sanchez, Y. Gonzalez, L. Gonzalez, M. Tello, R. Garcıa, D. Granados, J. M. Garcıa, and F. Briones, "Ordered InAs quantumdots on pre-patterned GaAs (001) by local oxidation nanolithography," *Journal of Crystal Growth,* vol. 284, 2005.